Measurement of the Hadronic Photon Structure Function F_2^γ at LEP2

Russell John Taylor

Department of Physics and Astronomy
University College London

Submitted for the degree of
Doctor of Philosophy
May 2002

Abstract

The hadronic structure function of the photon $F_2^\gamma(x, Q^2)$ is measured as a function of Bjorken x and of the photon virtuality Q^2 using deep-inelastic scattering data taken by the OPAL detector at LEP at e^+e^- centre-of-mass energies from 183 to 209 GeV. Previous OPAL measurements of the x dependence of F_2^γ are extended to an average Q^2 of $\langle Q^2 \rangle = 780$ GeV^2 using data in the kinematic range $0.15 < x < 0.98$. This represents the highest $\langle Q^2 \rangle$ measurement of F_2^γ made to date. The Q^2 evolution of F_2^γ is studied for $12.1 < \langle Q^2 \rangle < 780$ GeV^2 using three ranges of x. As predicted by QCD, the data show positive scaling violations in F_2^γ with $F_2^\gamma(Q^2)/\alpha = (0.08 \pm 0.02\,^{+0.05}_{-0.03}) + (0.13 \pm 0.01\,^{+0.01}_{-0.01}) \ln Q^2$, where Q^2 is in GeV^2, for the central x region 0.10–0.60.

Acknowledgements

Thanks are due to many people who have contributed in some way - large or small, direct or indirect - towards this thesis reaching its denouement.

The members of the OPAL Collaboration, past and present, are gratefully acknowledged for building and running an efficient experiment, and in particular the Two-Photon group and the editorial board for the paper for their role in refining the analysis. Those deserving of particular mention for their major roles in the analysis include Richard Nisius, Thorsten Wengler and all the F_2^γ students who went before me and unwittingly laid the groundwork for this thesis. At UCL, Jon Butterworth provided a lot of advice, especially during the first year of my PhD. Above all, many thanks are due to my supervisor, David Miller, for all his help and guidance throughout this work.

For financial support I am indebted to the Particle Physics and Astronomy Research Council; and at UCL to the Department of Physics and Astronomy, the HEP group and the Graduate School; and also to the Elizabeth Spreadbury Fund.

Outside of the realms of physics research, many people helped while away the few spare hours and days. This includes numerous fellow OPAL and Brit students, and I would just like to single out Steve Dallison for faithful drinking companionship - and apologise for the fact the I always flagged too soon! Among the 'non-physicists', I would like to make special mention of all my friends at EBCG, who will make leaving Geneva so difficult. Thankfully, I am taking one of them with me - and even better she is now my wife - so the biggest thanks of all go to Angie for being my best friend and so much more besides.

Finally, I would like to thank my parents, Andy and Brenda, and my sister and brother, Nicole and Stuart, for being a wonderful family through the years. Stu, we miss you more than words can express.

Russell Taylor
May 2002

Contents

List of Figures

List of Tables

Chapter 1

Introduction

The photon is unique in that it can act both as a fundamental particle - the gauge boson of QED - or as an extended object with structure. In the former, its more familiar, guise it is the mediator of the electromagnetic force between charged objects and can be regarded as a structureless object. QED is an abelian gauge theory, so it is not possible for two photons to directly interact with one another.

However, within QED the Heisenberg uncertainty principle allows that a photon can fluctuate into a charged fermion anti-fermion pair, with the restriction that $\Delta E \Delta t < 1$ (where $c = \hbar = 1$). Thus an interaction between two photons is possible because, for example, one photon can interact with one of the fermions into which the other photon has fluctuated. It is in this manner that the photon exhibits structure, which can be either leptonic or hadronic in nature. If the photon has fluctuated into a lepton pair then the process can be accurately calculated in QED. In the case of quarks the situation is more complicated, and the hadronic structure of the photon can be regarded as the sum of two parts - one where the splitting into quarks is with sufficient transverse momentum such that the entire process is calculable in perturbative QCD, and the other when the photon fluctuates into a hadronic

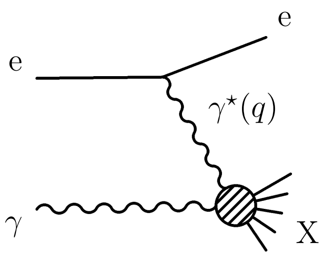

Figure 1.1: Deep inelastic electron-photon scattering.

state with the appropriate quantum numbers. This second, soft part means that the photon can also ‘contain’ gluons. The two aspects are often referred to as the point-like and hadron-like components.

Much of the information on the hadronic structure of the photon has been obtained from measurements at e^+e^- colliders, in interactions involving the photon ‘clouds’ that surround the beam electrons. Of particular importance have been measurements of deep-inelastic electron-photon[1] scattering, Figure 1.1, in which the structure of a nearly-real photon, γ, is probed by a highly virtual one, $\gamma^\star$ of virtuality q^2, producing a hadronic final state, X. In this context, structure functions of the photon can be defined in analogy with those of the proton, although the point-like component leads to important differences in the behaviour of photon structure functions.

Measurements of the hadronic photon structure function F_2^γ, such as that described in this thesis, use the fact that the differential cross-section of the process $e\gamma \rightarrow eX$ as a function of Q^2 and Bjorken x is proportional to $F_2^\gamma(x, Q^2)$. Here $Q^2 = -q^2$, and x can be thought of as the fraction of the photon's momentum carried by the struck quark. Because the photon couples to electric charge, F_2^γ is in leading order proportional to the quark content of the photon.

Experimentally, F_2^γ is measured using *single-tagged* events. Q^2 is determined from the energy and polar angle of the deeply-inelastically scattered (tagged)

[1]For conciseness positrons are also referred to as electrons.

electron, which is generally well measured by the electromagnetic calorimetry of the detector. The electron which emits the quasi-real photon is scattered at a very low angle and escapes unobserved down, or close to, the beam pipe. As a consequence, the energy of the target particle is not known - in contrast to electron-proton DIS - and so x has to be determined by measuring the invariant mass of the hadronic final state. Because the eγ centre-of-mass system does not coincide with the laboratory frame, the hadrons tend to be boosted in the forward direction and thus poorly contained in the detector. For this reason a central component in measurements of F_2^γ is the use of an unfolding procedure to relate the visible x distribution to the underlying true distribution. As a result, the accuracy of photon structure function measurements does not approach those of the proton.

The measurement of the photon structure function now has a history going back some 20 years, when the first results were obtained with the PETRA collider at DESY. Since then measurements have been carried out with PEP at SLAC, TRISTAN at KEK and, most recently, LEP at CERN. A summary of the world data on F_2^γ is shown in Figure 1.2, which is an updated version of a figure taken from a recent comprehensive review [1]. The published measurements [2–18] range in Q^2 from 0.24–390 GeV^2, and down to $\sim 10^{-3}$ in x. Several preliminary results from LEP experiments [19–21] are also shown, including one from this analysis [21].

This thesis describes measurements of F_2^γ made using data recorded by the OPAL detector in the years 1997–2000 at e$^+$e$^-$ centre-of-mass energies of 183–209 GeV. It includes a high-Q^2 measurement of F_2^γ as a function of x (at an average Q^2, $\langle Q^2\rangle$, of 780 GeV^2) and also the most precise OPAL measurement yet of the evolution of F_2^γ with Q^2.

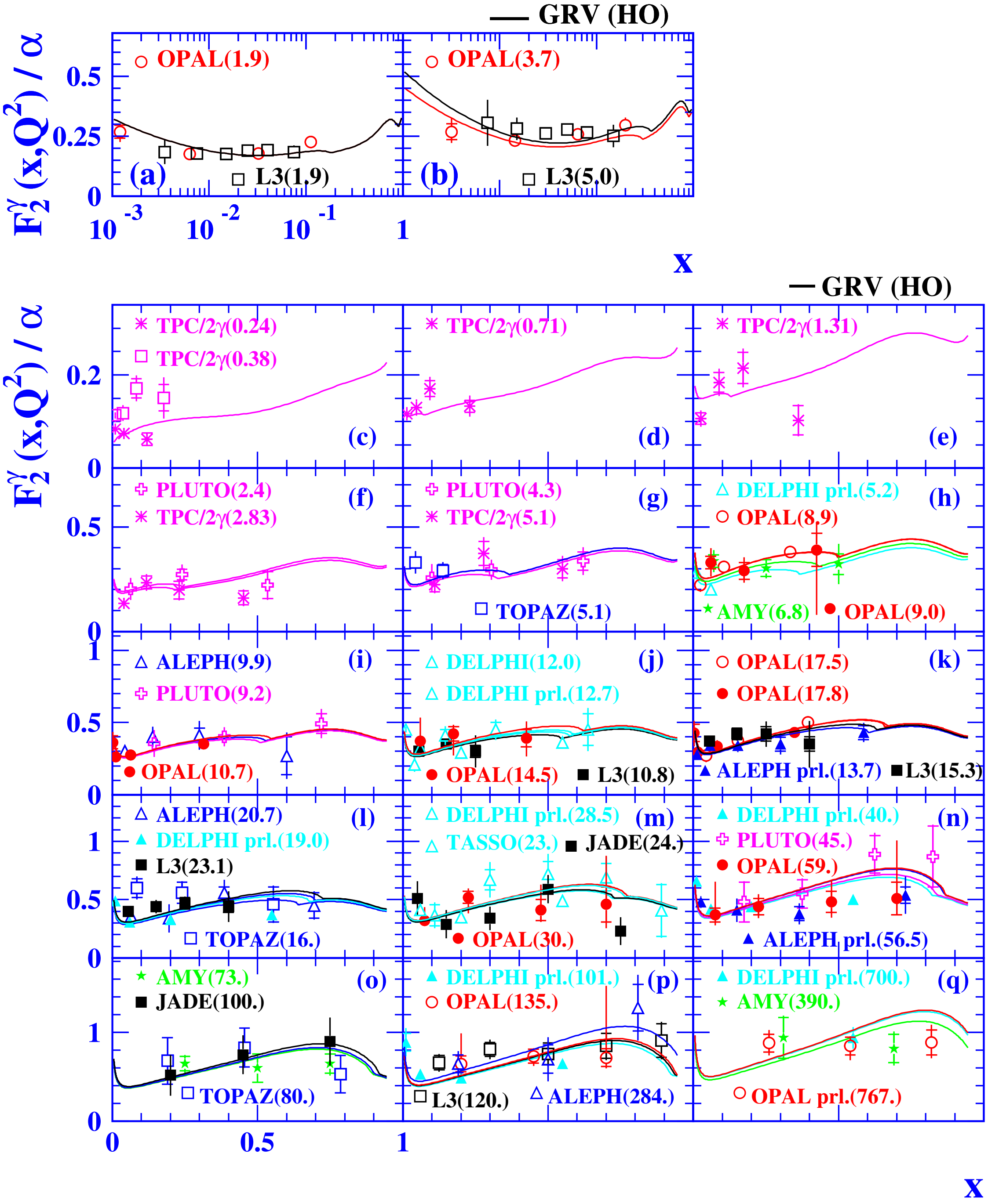

Figure 1.2: The world data on the hadronic photon structure function F_2^γ [1].

Chapter 2

Theory of Photon Structure

2.1 The Cross-Section for Photon-Photon Scattering

The multiperipheral diagram for the interaction of two photons of arbitrary virtuality at an e^+e^- collider is shown in Figure 2.1. The labels in brackets denote the four-vectors of the participants. The incoming electrons, of energy E_b, both radiate photons and are scattered at an angle $\theta_{1,2}$. The photons interact to produce a final state X, which in this thesis will always be regarded as hadronic, but could equally well be a lepton pair. (The leptonic structure of the photon has been measured by several experiments [14,22-26] and found to agree well with QED predictions.)

The radiated photons can have either transverse (T) or longitudinal (L) polarisation, and so the total differential cross-section for the multiperipheral process can be written in terms of four cross-sections corresponding to the possible combinations (σ_{TT}, σ_{TL}, σ_{LT} and σ_{LL}) and two interference terms

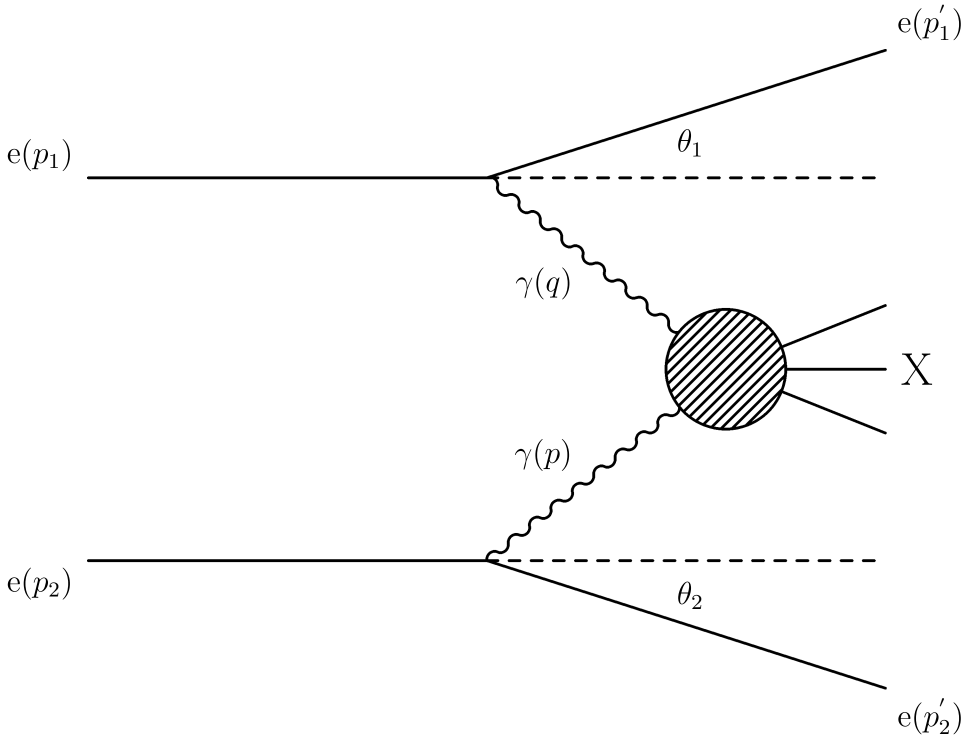

Figure 2.1: The multiperipheral diagram for the interaction of two photons at an e^+e^- collider.

($\tau_{\rm TT}$ and $\tau_{\rm TL}$). The cross-section for unpolarised beams is then [27]:

$$\begin{aligned} \mathrm{d}^6\sigma_{\mathrm{e^+e^-\to e^+e^-X}} = {} & \frac{\mathrm{d}^3\mathbf{p}'_1}{E'_1}\frac{\mathrm{d}^3\mathbf{p}'_2}{E'_2}\frac{\alpha^2}{16\pi^4 Q^2P^2}\left(\frac{(q\cdot p)^2-Q^2P^2}{(p_1\cdot p_2)^2-m_{\rm e}^4}\right)^{1/2} \\ & (4\rho_1^{++}\rho_2^{++}\sigma_{\rm TT}+2|\rho_1^{+-}\rho_2^{+-}|\tau_{\rm TT}\cos 2\bar{\phi}+2\rho_1^{++}\rho_2^{00}\sigma_{\rm TL} \\ & +2\rho_1^{00}\rho_2^{++}\sigma_{\rm LT}+2\rho_1^{00}\rho_2^{00}\sigma_{\rm LL}-8|\rho_1^{+0}\rho_2^{+0}|\tau_{\rm TL}\cos\bar{\phi})\,, \end{aligned} \tag{2.1}$$

where $\mathbf{p}'_{1,2}$ are the momentum vectors of the scattered electrons and $E'_{1,2}$ their energies, $P^2 = -p^2$ and $\bar{\phi}$ is the angle between the scattering planes of the two electrons in the photon-photon centre-of-mass frame. The coefficients $\rho_{1,2}^{ab}$, where $a, b = +, -, 0$ are the photon helicities, are elements of the photon density matrix and depend only on the kinematic variables and on $m_{\rm e}$. They are given in full in, for example, Equation 5.13 of reference [27].

This thesis is concerned with the case where one of the photons is quasi-real and the other is highly virtual ($\gamma^\star\gamma$ events). In this situation the expression for the cross-section simplifies considerably, since a real photon can have only transverse polarisation. The terms σ_{TL}, σ_{LL} and τ_{TL} vanish as $P^2 \to 0$. The term proportional to τ_{TT} also vanishes because for $P^2 = 0$ the angle $\bar{\phi}$ is undefined. Thus Equation 2.1 reduces to

$$\mathrm{d}^6\sigma = \frac{\mathrm{d}^3\mathbf{p}_1'}{E_1'}\frac{\mathrm{d}^3\mathbf{p}_2'}{E_2'}\frac{\alpha^2}{16\pi^4 Q^2 P^2}\left(\frac{(q\cdot p)^2 - Q^2P^2}{(p_1\cdot p_2)^2 - m_\mathrm{e}^4}\right)^{1/2} 4\rho_1^{++}\rho_2^{++}\left(\sigma_\mathrm{TT} + \frac{\rho_1^{00}}{2\rho_1^{++}}\sigma_\mathrm{LT}\right). \quad (2.2)$$

Only the terms σ_{TT} and σ_{LT} remain, corresponding to the probing of a transverse target photon by, respectively, a transverse or longitudinal virtual photon.

2.2 The Equivalent Photon Approximation

It is usual to factorise the cross-section of Equation 2.2 into two terms: an expression for the flux of incoming, transversely polarised, quasi-real target photons, and a term describing the reaction $\mathrm{e}\gamma \to \mathrm{eX}$. This can be written as

$$\mathrm{d}^3\sigma_{\mathrm{e^+e^-\to e^+e^-X}} = \left(\int \Gamma_{\gamma/e}(z, P^2)\,\mathrm{d}P^2\right)\cdot\frac{\mathrm{d}^2\sigma_{\mathrm{e}\gamma\to\mathrm{eX}}}{\mathrm{d}x\mathrm{d}Q^2}, \quad (2.3)$$

which is derived from Equation 2.2 in Reference [1]. The integral term is the Weizsäcker-Williams [28] formula for the flux of real photons. The flux factor

$$\Gamma_{\gamma/e} = \frac{\alpha}{2\pi}\left(\frac{1+(1-z)^2}{zP^2} - \frac{2m_e^2 z}{P^4}\right) \quad (2.4)$$

is the equivalent photon approximation (EPA) [29], which gives the spectrum of photons of energy zE_b at a finite (but small) virtuality P^2. The integration runs from the minimum possible P^2, which is given by four-vector conservation [30], to the maximum, which is determined by the experimental acceptance, leading to

$$\int \Gamma_{\gamma/e}\, \mathrm{d}P^2 = \frac{\alpha}{2\pi}\left[\frac{1+(1-z)^2}{z}\ln\frac{P^2_{max}}{P^2_{min}} - 2m_e^2 z\left(\frac{1}{P^2_{min}} - \frac{1}{P^2_{max}}\right)\right]. \quad (2.5)$$

2.3 Photon Structure Functions

It is normal to describe the cross-section for $\mathrm{e}\gamma \to \mathrm{eX}$ (the second term in Equation 2.3) in terms of structure functions of the real photon. It is useful, therefore, to define the usual DIS invariant variables which, neglecting the electron mass, are:

$$Q^2 = -q^2 = 2\,E_\mathrm{b}\,E_\mathrm{tag}\,(1-\cos\theta_\mathrm{tag})\,, \quad (2.6)$$

$$x = \frac{Q^2}{2\,q\cdot p} = \frac{Q^2}{Q^2+W^2+P^2}\,, \quad (2.7)$$

$$y = \frac{q\cdot p}{p_1\cdot p} = 1 - \frac{E_\mathrm{tag}}{E_\mathrm{b}}\cos^2\frac{\theta_\mathrm{tag}}{2}\,, \quad (2.8)$$

where the experimentally measurable variables E_tag and θ_tag are the energy and polar angle respectively of the tagged electron, and W is the invariant mass of the hadronic final state, X. In the DIS limit $Q^2 \gg P^2 \approx 0$, and so P^2 is neglected in the calculation of x from Equation 2.7.

The transverse and longitudinal structure functions of the photon are defined, in the limit $P^2 = 0$, as [31]:

$$F_\mathrm{T}^\gamma = \frac{Q^2}{8\pi^2\alpha x}\,\sigma_\mathrm{TT} \quad (2.9)$$

$$F_\mathrm{L}^\gamma = \frac{Q^2}{4\pi^2\alpha}\,\sigma_\mathrm{LT}\,. \quad (2.10)$$

Through use of the above and the relation

$$F_2^\gamma = 2xF_\mathrm{T}^\gamma + F_\mathrm{L}^\gamma\,, \quad (2.11)$$

the second term of Equation 2.3 can be written as

$$\frac{\mathrm{d}^2\sigma_{\mathrm{e}\gamma\to\mathrm{eX}}}{\mathrm{d}x\mathrm{d}Q^2} = \frac{2\pi\alpha^2}{x\,Q^4}\left[\left(1+(1-y)^2\right)F_2^\gamma(x,Q^2) - y^2F_\mathrm{L}^\gamma(x,Q^2)\right]\,. \quad (2.12)$$

The experimental requirement of a high tag energy means that only low values of y are studied, rendering negligible the term proportional to F_{L}^{γ}. Thus the structure function F_2^{γ} can be related through a simple proportionality factor to the differential cross-section for $e\gamma$ scattering.

2.4 Theoretical Predictions for F_2^{γ}

The hadronic structure of the photon can be viewed, in analogy to the proton, in terms of a sum of distributions of partons in the photon. In this view, and in leading order,

$$F_2^{\gamma}(x, Q^2) = x \sum_{i=1}^{n_f} e_i^2 \left[q_i^{\gamma}(x, Q^2) + \bar{q}_i^{\gamma}(x, Q^2) \right] , \tag{2.13}$$

where q_i^{γ} is the parton distribution function parameterising the probability of finding a quark, of flavour i and charge e_i, within the photon at a given (x,Q^2).

As mentioned in the introduction, F_2^{γ} can be regarded as the sum of two parts - the point-like and the hadron-like components. The point-like part is most important at higher x and Q^2, and is most simply approximated by the quark-parton model, whilst the description of the hadron-like part, which dominates at low x and Q^2, is usually based on a vector meson dominance ansatz. These models are described in the two sections which follow.

2.4.1 Quark Parton Model

The first calculations of the photon structure function were based on the quark-parton model (QPM), in which the quarks are treated as free particles and gluons are neglected. This, of course, is nothing but QED modified to take account of the quark charges and include a colour factor. The calculation

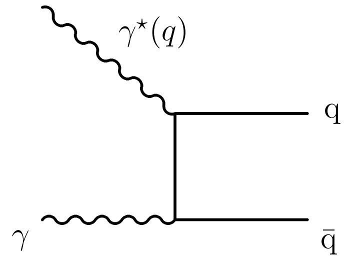

Figure 2.2: The box diagram for the process $\gamma^\star\gamma \to \mathrm{q\overline{q}}$.

of F_2^γ is based on the box diagram for the process $\gamma^\star\gamma \to \mathrm{q\overline{q}}$ shown in Figure 2.2 which, for the real photon, leads to [32]

$$F^\gamma_{2,\mathrm{QPM}} = \frac{3\,\alpha}{\pi} \sum_{i=1}^{n_f} e_i^4\, x \left[\left(x^2 + (1-x)^2 \right) \ln \left(\frac{Q^2(1-x)}{m_i^2\, x} \right) + 8x(1-x) - 1 \right] , \tag{2.14}$$

where the sum runs over all active flavours ($4m_i^2 < W^2$, where m_i is the quark mass).

The QPM is shown as a function of x in Figure 2.3 for the lowest and highest values of $\langle Q^2 \rangle$ in this analysis. It is calculated for four active flavours with masses of 0.325 GeV for light quarks and 1.5 GeV for charm quarks. The step in the curve for $Q^2 = 12.1$ GeV is due to the charm threshold. Charm quark pairs can only be created at values of x to the left of the threshold, as shown by Equation 2.7, which also indicates that the threshold moves to higher x with increasing Q^2 - hence the fact that it is not visible in the curve for $Q^2 = 780$ GeV. The QPM is only a model for the point-like component of F_2^γ, which is expected to dominate in the high-Q^2 measurement presented in this thesis. Thus the QPM should be a reasonable approximation in this region. However, we know that even here it is by no means a complete model because of the coupling of quarks to gluons, and also because the quark masses used are really only appropriate at low scales.

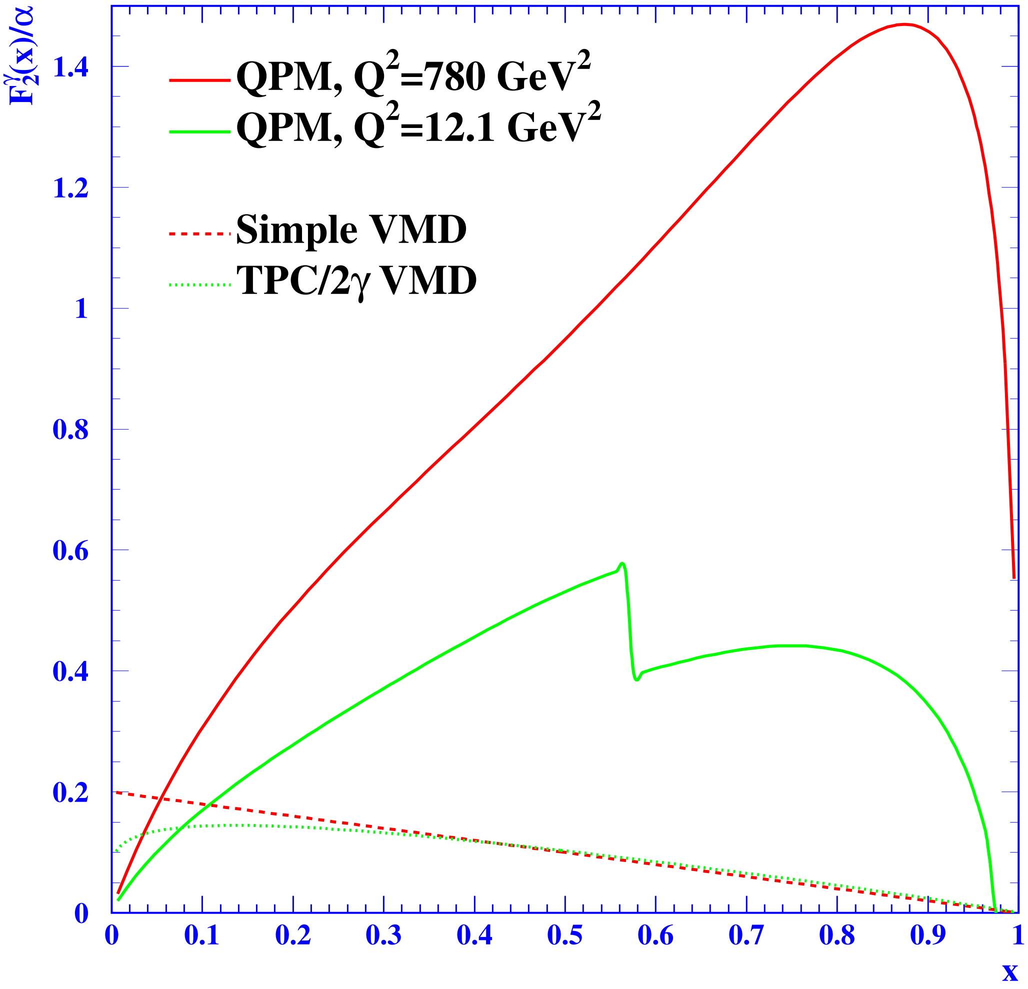

Figure 2.3: Components of F_2^γ according to the QPM and VMD models. The QPM (Equation 2.14) is shown as a function of x for four flavours with quark masses of 325 MeV for u, d, s and 1.5 GeV for charm. It is plotted at the lowest and highest values of $\langle Q^2 \rangle$ in this analysis. The VMD parameterisations of Equations 2.15 and 2.16 are also shown.

2.4.2 Vector Meson Dominance

The hadron-like part of the photon cannot be calculated by current theoretical techniques, since the problem is non-perturbative in nature. Because the photon couples to the $J^{PC} = 1^{--}$ vector meson states (e.g. ρ, ω, ϕ), the usual way of estimating the hadron-like part is to use a vector meson dominance (VMD) model. The parton distributions of the vector mesons have not been measured, but the structure function of the ρ can be approximated by that of the pion, which is known experimentally [33]. Using this basis, estimates for the VMD component can be arrived at via various assumptions. As an example, the simplest VMD estimate is obtained by taking contributions of ρ and ω, leading to [31, 34]

$$F^{\gamma}_{2,\mathrm{VMD}} = 0.2\,\alpha\,(1-x)\,, \tag{2.15}$$

which applies to $Q^2 \sim 10\ \mathrm{GeV}^2$.

An alternative approach is to parameterise a VMD component by fitting to measurements of the pion structure function, F_2^{π}, or to low-Q^2 F_2^{γ} data. The latter has been done by the TPC/2γ Collaboration [6], and their fit, which was to data at $\langle Q^2 \rangle = 0.7\ \mathrm{GeV}^2$, gives

$$F^{\gamma}_{2,\mathrm{VMD}} = \alpha\left(0.22\,x^{0.31}(1-x)^{0.95} + 0.06\,(1-x)^{2.5}\right). \tag{2.16}$$

Caution should be accorded to this fit, though, since the highest x point used corresponds to very low W - deep into the poorly understood region of resonance production.

The two parameterisations given above are shown in Figure 2.3, but note that the two curves were obtained for different values of Q^2, and no Q^2 dependence is included. The importance of the VMD component is expected to decrease with increasing x and Q^2 - both absolutely and as a proportion of the full F_2^{γ} - but it can be seen that its contribution is significant at the lowest values of Q^2 considered in this thesis, particularly at low x.

2.4.3 QCD and the Evolution of F_2^γ with Q^2

Although the size and shape of F_2^γ at a given, finite Q^2 cannot be calculated because of the hadron-like part, the evolution of F_2^γ with Q^2 can be determined within the framework of perturbative QCD. It should first be noted, however, that even the naive parton model predicts a logarithmic increase of F_2^γ with Q^2 (Equation 2.14) - unlike F_2^{p} which exhibits Bjorken scaling in this model, which is only broken once QCD corrections are taken into account. This feature of F_2^γ arises because of the point-like part of the photon, which leads to positive scaling violations at all values of x (Figure 2.4). Contrast this with the case of the proton (Figure 2.5), where gluon radiation leads to negative scaling violations at large x and pair production of quarks from gluons results in positive scaling violations at small x.

The original QCD evaluation of F_2^γ was undertaken by Witten using the technique of operator product expansion [35]. He found that both the shape and normalisation of F_2^γ are calculable at asymptotically large Q^2, and that the evolution of F_2^γ is similar to the QPM case:

$$F_2^\gamma \propto \ln \frac{Q^2}{\Lambda^2}\,, \tag{2.17}$$

at leading logarithmic order. The asymptotic solution has been re-derived using Feynman diagrams [36, 37], evolution equations [38] and in NLO [39]. In addition, parameterisations based on this method have been presented [40–42].

Unfortunately, we are not able to reach the asymptotic region, and so a different approach has to be taken. Although it is not possible to calculate the shape or normalisation of F_2^γ at finite Q^2, its evolution with Q^2 can be determined through use of the QCD evolution equations. These equations express the fact that as the resolution (i.e. Q^2) is increased more of the partons which share the photon's momentum can be 'seen'. The probability of finding a quark at small x increases and that of finding one at high x decreases, because high-momentum quarks lose momentum by radiating gluons. The

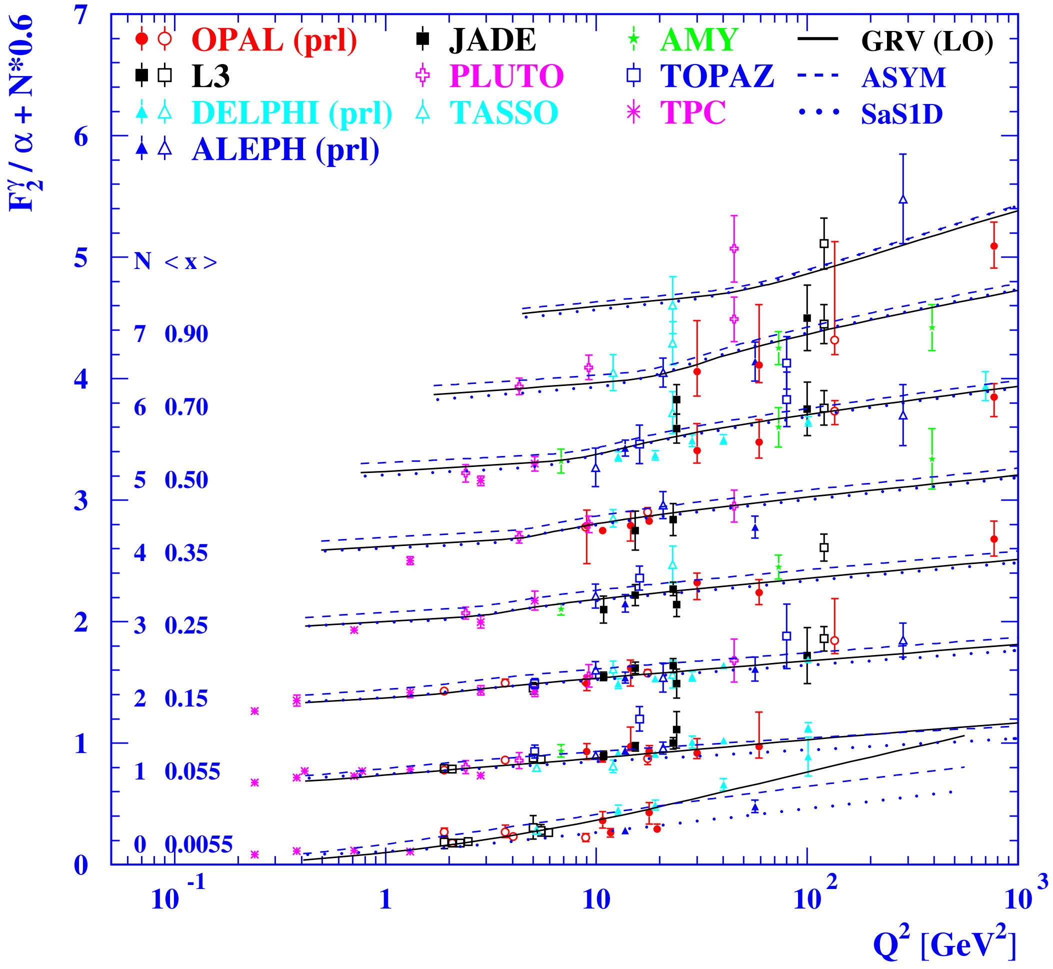

Figure 2.4: Summary of the measurements of the Q^2 evolution of F_2^γ. Taken from Reference [1].

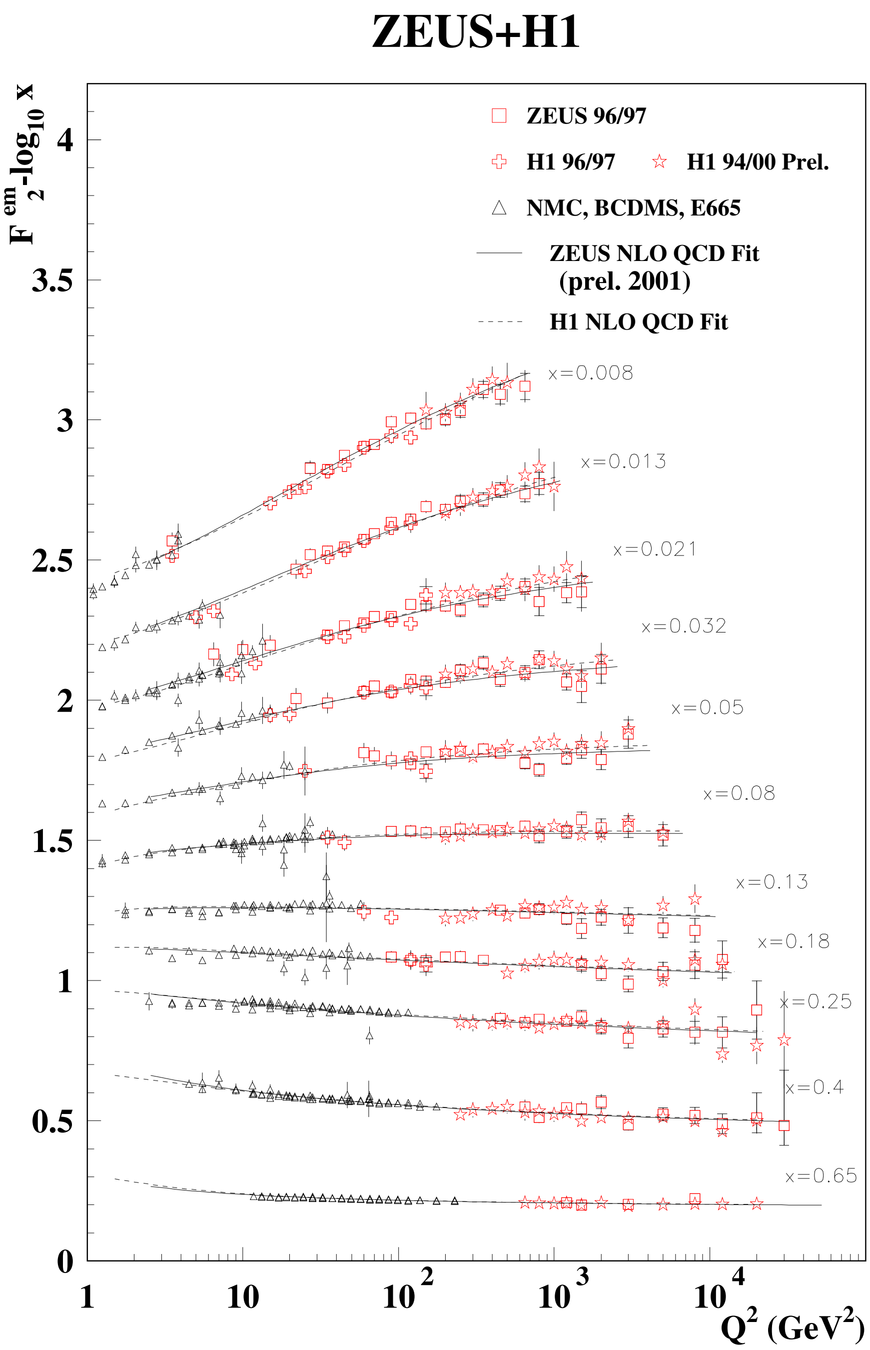

Figure 2.5: Summary of the measurements of the Q^2 evolution of F_2^{p}. Taken from Reference [43].

radiated gluons can in turn produce sea quarks with even lower momentum. Thus, for the hadron-like part of the photon, a shift from high to low x is expected with increasing Q^2. In addition, the point-like part increases with Q^2 for all x.

In order to calculate F_2^γ at a given scale, one needs to first fix the input x distribution at some low scale, based either on theoretical considerations or a fit to F_2^γ data. Then the evolution of the quark and gluon distributions is given by the DGLAP [44] equations, which to leading order are:

$$\frac{\mathrm{d}q_i(x,Q^2)}{\mathrm{d}\log Q^2} = \frac{\alpha}{2\pi}P_{\gamma q}(x) + \frac{\alpha_s}{2\pi}\int_x^1 \frac{\mathrm{d}x'}{x'}\left(q_i(x',Q^2)P_{qq}(\frac{x}{x'}) + g_i(x',Q^2)P_{qg}(\frac{x}{x'})\right) \tag{2.18}$$

$$\frac{\mathrm{d}g_i(x,Q^2)}{\mathrm{d}\log Q^2} = \frac{\alpha_s}{2\pi}\int_x^1 \frac{\mathrm{d}x'}{x'}\left(\sum_i q_i(x',Q^2)P_{gq}(\frac{x}{x'}) + g_i(x',Q^2)P_{gg}(\frac{x}{x'})\right). \tag{2.19}$$

These equations apply to massless quarks. The $P_{ij}(z)$ are splitting functions which express the probability of finding a parton of type i within a parton of type j with momentum fraction z. For a good discussion of the evolution equations as applied to the photon see Reference [45], which also covers the extension to NLO.

The Q^2 evolution of F_2^γ remains logarithmic, the running of α_s balancing the effects of gluon emission. If α_s were fixed, F_2^γ would bend with Q^2 to become asymptotically scale-invariant at large Q^2 [34]. A measurement of the evolution, using as long as possible a lever arm in Q^2, is therefore a good test of perturbative QCD predictions. It also holds out the possibility of obtaining a competitive measurement of α_s [46].

2.5 Heavy Quarks

The contribution of charm to F_2^γ needs to be dealt with differently since the above evolution equations apply only to massless quarks, and charm can only be regarded as massless at high scales and large invariant masses. Massive quark DGLAP equations have been derived [47], but the treatment can be simplified by the hard scale resulting from the mass. This means that the zeroth-order QCD calculation (i.e. QPM, but not neglecting the mass terms), known as the Bethe-Heitler formula, is a good approximation and in particular deals with the threshold ($W = 2m_c$) behaviour correctly [48]. This is in contrast to the QPM (see Figure 2.3); in reality the cut-off should not be sharp because the phase space for charm production is limited near the threshold.

The charm contribution is expected to be almost entirely point-like in the x region considered in this thesis, but at low x a LO resolved contribution does come from photon-gluon fusion. The charm structure function $F_{2,c}^{\gamma}$ has been calculated to NLO [49], and has recently been measured by OPAL [50]. The production of b quarks is suppressed by the larger mass and small charge, and is negligible at LEP2 energies.

2.6 The P^2 Dependence of F_2^{γ}

In the discussion above the target photon has been assumed to be real, i.e. $P^2 = 0$. In fact, because of the incomplete experimental acceptance in the very forward direction, P^2 is only restricted to be less than a fixed maximum. The effect of this is twofold; first, the flux of target photons is affected, and second, the structure function $F_2^{\gamma}(x, Q^2, P^2 \neq 0)$ is in general not expected to be equal to $F_2^{\gamma}(x, Q^2, P^2 = 0)$.

The flux of target photons can be calculated with sufficient accuracy using the EPA (Equation 2.4). It is strongly peaked at the minimum P^2, with a median of around 10^{-4} GeV^2. The impact on the structure function, however, is not as clear-cut. The virtual photon is expected to exhibit a more point-like behaviour than the real photon. The point-like component has been

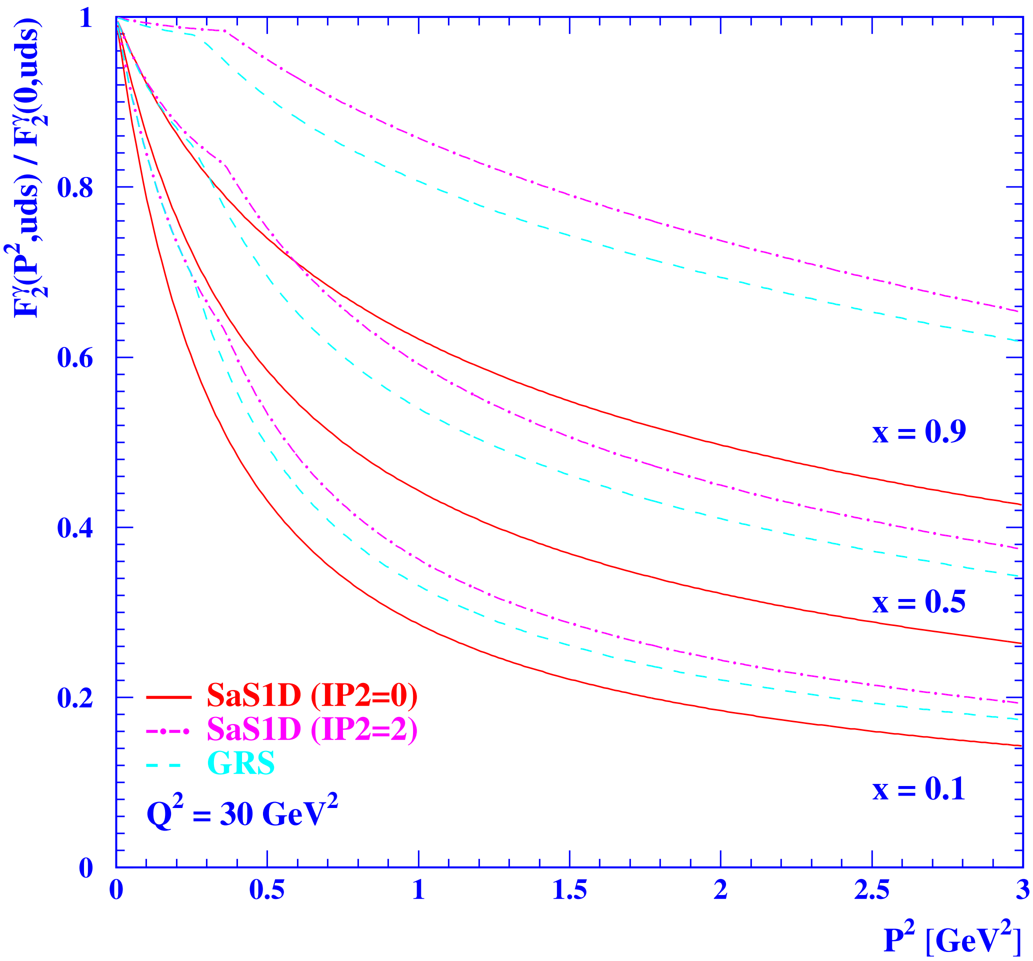

Figure 2.6: The predicted P^2 suppression of F_2^γ according to different models. Shown are the SaS1D [54] and GRS [55] parameterisations for virtual photons. Note that the SaS set acknowledges the theoretical uncertainty by providing more than one model (they in fact give six in total). Figure taken from Reference [1].

calculated at LO and NLO [51] in the limit $Q^2 \gg P^2 \gg \Lambda^2$. The hadron-like part is expected to be suppressed as P^2 increases, but the rate of the fall-off is theoretically uncertain and the experimental knowledge is very poor. PLUTO [52] and L3 [17] have measured the virtual photon structure function F^{γ}_{eff} ($\equiv F_2^{\gamma} + 3F_{\mathrm{L}}^{\gamma}/2$), but with severely limited statistics, and data have also been presented by the HERA experiments [53]. Data do not exist on the structure functions of virtual mesons, making the choice of a suitable VMD input to the parameterisations a difficult one. The outcome of all this is that the different parameterisations of the P^2 dependence of F_2^{γ} show large discrepancies, as demonstrated in Figure 2.6, although the qualitative behaviour is the same.

2.7 Parameterisations of F_2^{γ}

A number of parameterisations of the real photon structure function F_2^{γ} have been presented, in both leading and next-to-leading order, based on the DGLAP evolution equations. The various sets differ in the chosen starting scale for the evolution, in the input distributions assumed at that scale and in the amount of data used to determine any free parameters. There are also choices to be made with respect to the value of the QCD scale Λ, the treatment of charm and, for the NLO sets, the factorisation scheme.

The choice of the input quark and gluon distributions can be based either on theoretical prejudice (usually some VMD-based argument), on a phenomenological fit to the data, or on a combination of the two. The quark distribution is by now reasonably well constrained by the data, at least in the central x region, but it should be borne in mind that most of the sets described here are fairly old and therefore based on a relatively small fraction of the current full data. The constraint at high x is poor because of the need to restrict invariant masses to be above the resonance region. The gluon distribution is not well constrained by measurements of F_2^{γ}, since it is only important at low x - a region where measurements have only recently become available - and even there only indirectly. Data exist which are directly sensitive to the gluon distribution of the photon, such as jet production data from LEP and HERA, but no significant effort has yet been made to incorporate these results into any parameterisation.

2.7.1 Glück, Reya and Vogt (GRV)

The GRV parameterisation [56] is available in LO and NLO, and was motivated by the successful description of the proton and pion structure functions by the same authors. The evolution is started from a very low scale (0.25 GeV^2 for LO and 0.3 GeV^2 for NLO) and the input distribution is a purely hadron-like one based on VMD arguments. The point-like part is generated dynamically with the evolution equations. The VMD input is the same for both the quark and gluon distributions and takes the form $xf_\pi \sim x^a(1-x)^b$, where a and b are obtained from measurements of the pion structure function. The only free parameter is the normalisation of the VMD input, corresponding to the uncertainty in the inclusion of the ω and ϕ mesons. It is determined by fitting to data in the region $0.71 < Q^2 < 100$ GeV^2, and $W > 2$ GeV to avoid the resonance region. Charm and bottom quarks are included via the Bethe-Heitler formula, with $m_c = 1.5$ GeV and $m_b = 4.5$ GeV, and are treated as massless in the evolution at high values of W. These parameterisations are by now somewhat elderly, yet in general they still do a good job of describing all the current F_2^γ data.

2.7.2 Glück, Reya and Schienbein (GRSc)

These LO and NLO parton distribution functions [57] are basically an update of the GRV parameterisation. The major change is in the determination of the input distribution, where a coherent sum of vector mesons is used instead of the incoherent sum of the GRV parameterisation. This eliminates the only free parameter and means that no fit to data was required. The charm contribution was added using the Bethe-Heitler formula, but the charm mass used was reduced to 1.4 GeV. The GRSc LO parameterisation is compared to the LO and NLO GRV curves, at three values of Q^2, in Figure 2.7. Note that, particularly at low Q^2, the differences between the GRV LO and NLO parameterisations are greater than those between the two LO sets.

2.7.3 Hagiwara *et al.* (WHIT)

The WHIT LO parameterisations [48] start their evolution at a relatively high starting scale of 4 GeV^2. This means that the input distributions need to include some point-like contribution, and the input valence quark distribution is parameterised by $xq(x)/\alpha = Ax^B(1-x)^C$, with the coefficients obtained from fits to data in the range $4 < Q^2 < 100$ GeV^2. The sea quark distribution is approximated by the Bethe-Heitler formula using $m_q = 0.5$ GeV. Charm is included via Bethe-Heitler for $Q^2 < 100$ GeV^2 and through the use of the massive evolution equations for higher values of Q^2. The charm mass is taken to be 1.5 GeV. The gluon input distributions take the same functional form as the valence quark input, but the coefficients are systematically varied within the limits allowed to still be consistent with the data. This results in six different sets of parton distribution functions. However, because the gluon distribution only has a strong effect at low x, the differences between the sets are small for the values of x ($x > 0.1$) considered in this thesis.

2.7.4 Schuler and Sjöstrand (SaS)

Schuler and Sjöstrand have produced [54] two sets, SaS1 with a starting scale of 0.36 GeV^2, and SaS2 which starts at 4 GeV^2. Although these are LO sets, a higher order term is included by hand, in both the $\overline{\mathrm{MS}}$ and DIS$_\gamma$

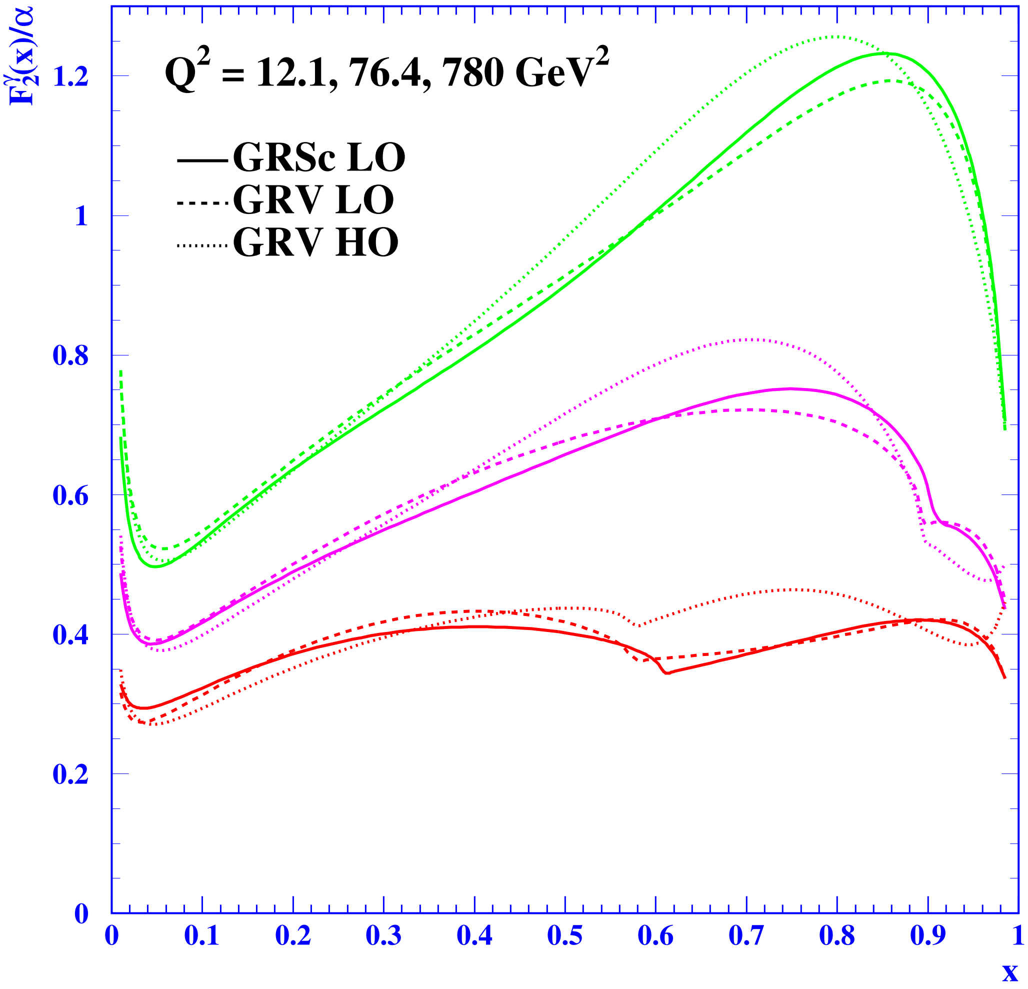

Figure 2.7: The GRV LO and HO and GRSc LO parameterisations of F_2^γ, shown at three values of Q^2 for which results are obtained in this thesis. The kink in the curves at the two lower values of Q^2 are due to the charm threshold, which sits at an x value determined by the charm mass used and Q^2. These parameterisations use massive charm quarks, hence the threshold behaviour is different to the sharp cut-off seen for the QPM (Figure 2.3).

factorisation schemes, leading to four sets in all. For the SaS2 sets the shape and normalisation of the hadron-like input distribution is determined by fitting to F_2^γ data. For the SaS1 sets only the shape is obtained from a fit to F_2^γ data, whilst the normalisation is taken from an analysis of γp data. Bethe-Heitler contributions of charm and bottom are included, with $m_c = 1.3$ GeV and $m_b = 4.6$ GeV.

Two of the SaS sets, 1D and 2M, are compared to the WHIT1 and GRSc LO parameterisations in Figure 2.8. It can be seen that the GRSc LO and SaS1D curves are very close to one another, particularly at high Q^2. The SaS sets are quite different from one another, especially at low Q^2. The WHIT1 curves show their strongest difference to the others at high x and Q^2.

2.7.5 Other Parameterisations

Various other parton distribution functions of the real photon have been produced. The sets from Drees and Grassie [58] and those of Abramowicz, Charchula and Levy [59] are both very old and have by now been ruled out by the data. There also exist both LO and NLO sets from Gordon and Storrow [42, 60] and a NLO set from Aurenche, Guillet and Fontannaz [61].

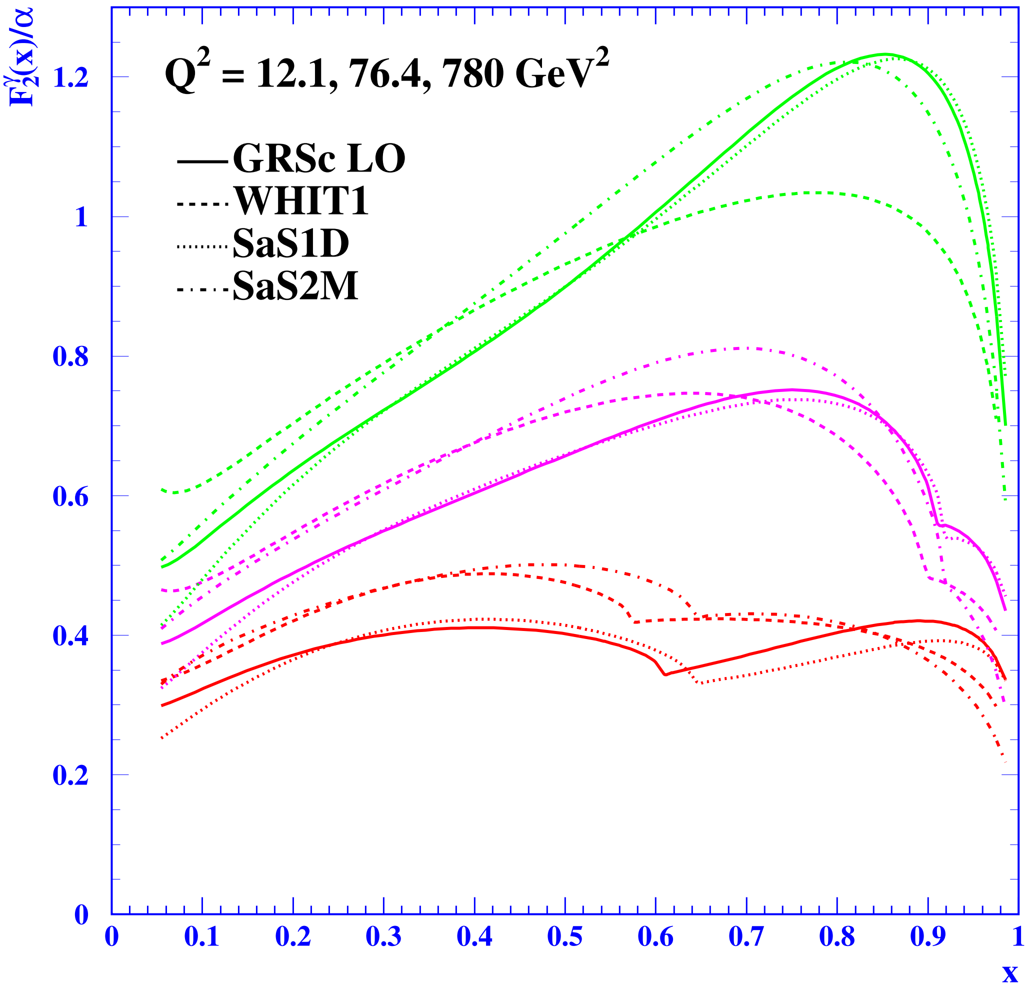

Figure 2.8: The GRSc LO, WHIT1, SaS1D and SaS2M and parameterisations of F_2^γ, shown at three values of Q^2 for which results are obtained in this thesis.

Chapter 3

LEP and the OPAL Detector

3.1 LEP

The LEP collider at CERN, an e^+e^- collider of 27 km circumference, operated between the years 1989 and 2000. During the first phase (LEP1, 1989-1995) the beams were accelerated using room temperature copper cavities and collided at centre-of-mass energies, $\sqrt{s}$, close to the mass of the Z^0. For the second phase of LEP's life (LEP2, 1995-2000) superconducting rf accelerating cavities were added, bringing $\sqrt{s}$ past the threshold for the production of W^+W^- pairs and ultimately up to $\sim$209 GeV in the pursuit of new physics.

The beams, made up of bunches of electrons or positrons, were steered around the curved sections of LEP by a combination of dipole, quadrupole and sextupole magnets, and horizontal and vertical dipole correctors. In between were long straight sections which contained the accelerating cavities and the experimental collision points. At each intersection point the beams were tightly focussed using superconducting quadrupoles to give good luminosity.

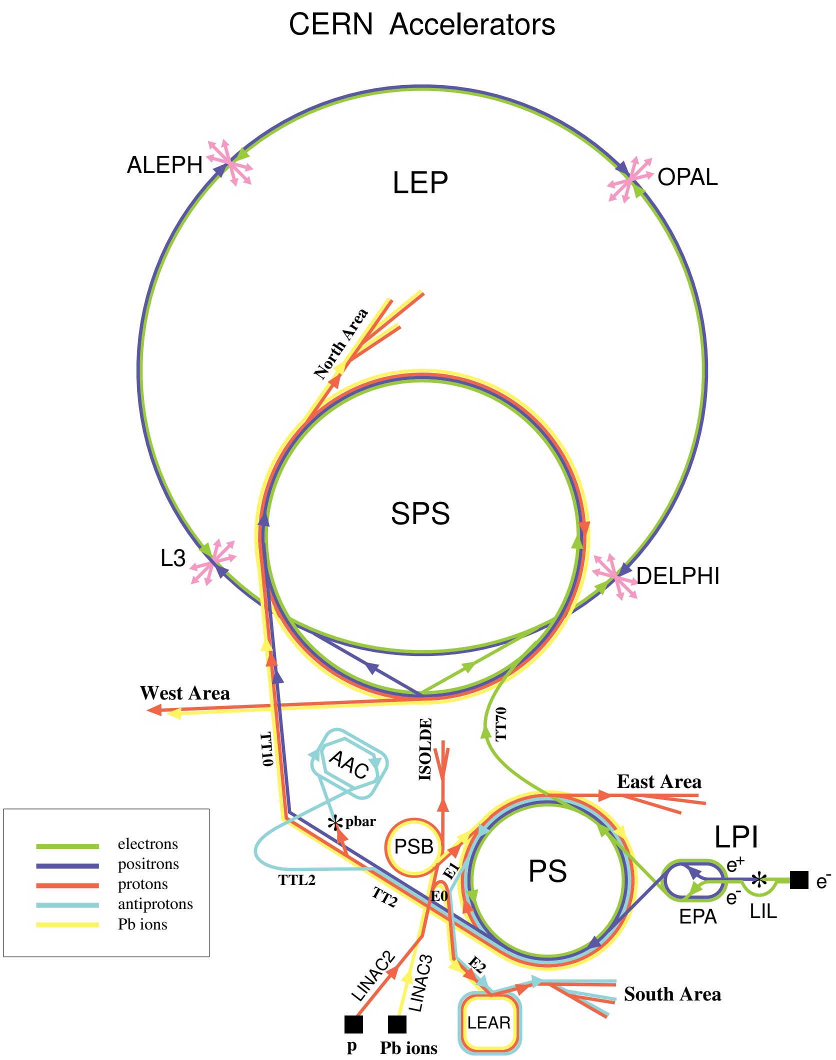

LEP: Large Electron Positron collider
SPS: Super Proton Synchrotron
AAC: Antiproton Accumulator Complex
ISOLDE: Isotope Separator OnLine DEvice
PSB: Proton Synchrotron Booster
PS: Proton Synchrotron
LPI: Lep Pre-Injector
EPA: Electron Positron Accumulator
LIL: Lep Injector Linac
LINAC: LINear ACcelerator
LEAR: Low Energy Antiproton Ring

Rudolf LEY, PS Division, CERN, 02.09.96

Figure 3.1: The CERN accelerator complex during the LEP era.

LEP was the last accelerator in a chain of five, which are illustrated in Figure 3.1. The injectors consisted of two linacs of 200 and 600 MeV, fed by an electron gun and a positron converter, followed by the 600 MeV Electron-Positron Accumulator, which injected into the CERN PS operating as a 3.5 GeV e^+e^- sychrotron. The electron and positron bunches would then pass from the PS into the SPS, which accelerated them to 22 GeV prior to their injection into LEP.

3.2 The OPAL Detector

OPAL [62] was one of the four large detectors situated around LEP. It was a multipurpose apparatus designed to efficiently detect all types of interactions occurring in e^+e^- collisions, with nearly full solid angle acceptance. The detector was made up of a number of subdetector systems, the information from which was combined to reconstruct the events.

The general layout is shown in Figures 3.2 and 3.3, indicating the location and relative size of the various subdetectors. Charged particles were detected by a silicon microvertex detector, a drift chamber vertex detector, and a large volume jet chamber. This central tracking system was contained inside a solenoid which provided a uniform magnetic field of 0.435 T along the beam direction. Outside the jet chamber, but still in the magnetic field, lay a layer of drift chambers which were used to improve the track reconstruction in the z-coordinate. The solenoidal coil was surrounded in both the barrel and end-cap regions by a counter array with good time resolution, an electromagnetic calorimeter with a presampler, the flux return yoke, instrumented to serve as a hadronic calorimeter, and outer layers of muon chambers. A set of small calorimeters placed directly around the beam pipe in the very forward direction was used to measure luminosity. The detector elements are described in more detail below.

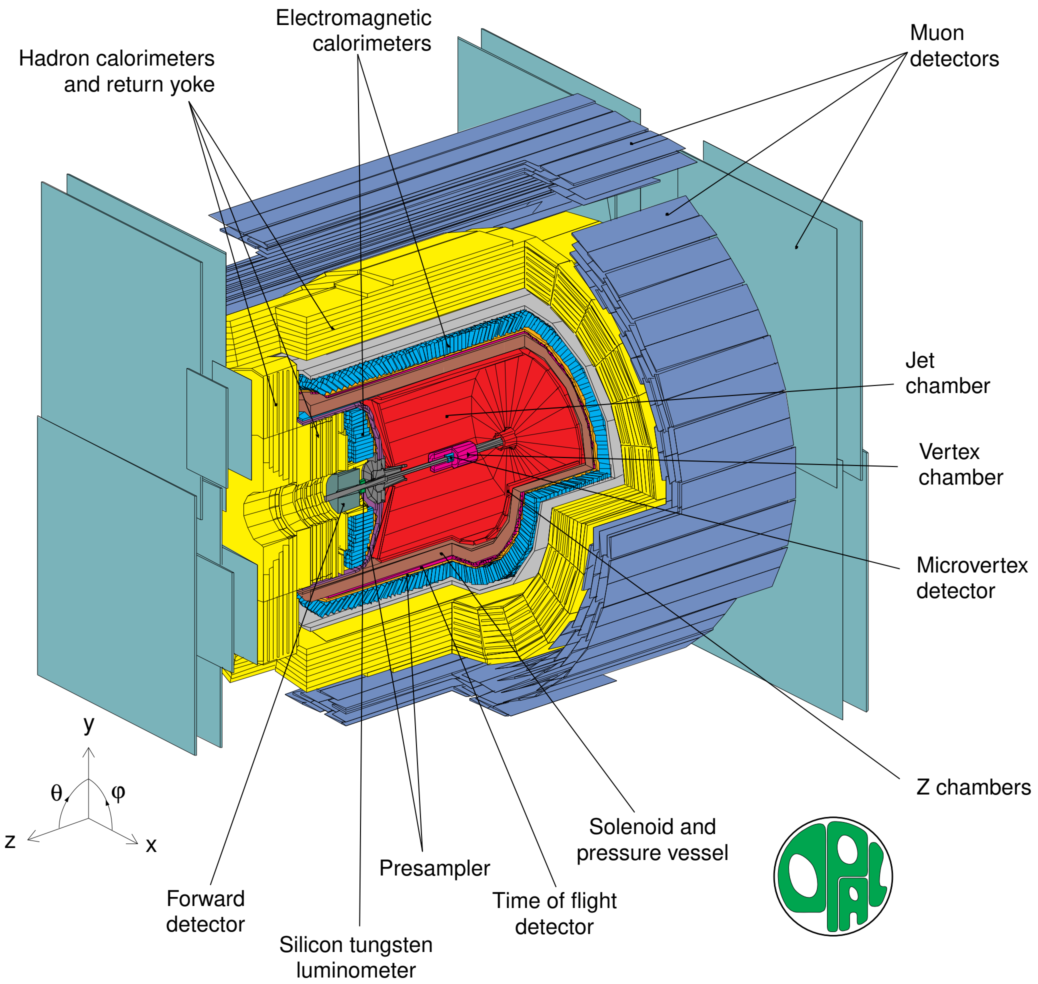

Figure 3.2: A cut-away view of the OPAL detector.

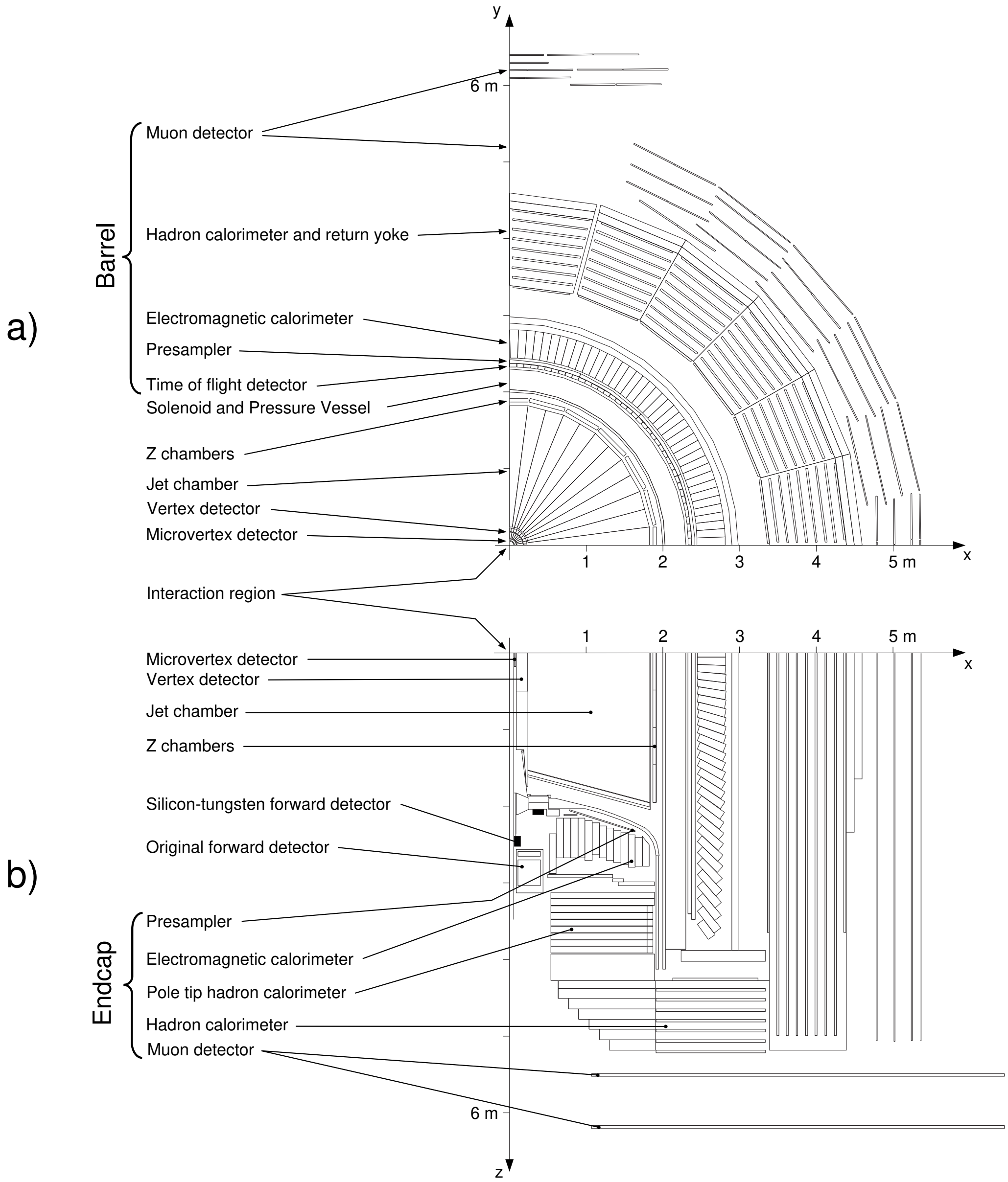

Figure 3.3: A cross-section view of the OPAL detector.

The critical subdetectors to the present analysis are, firstly, those used to tag the scattered electrons from two-photon collisions and, secondly, those important to a good reconstruction of the invariant mass of the hadronic final state. In this analysis, electrons are tagged in the endcap electromagnetic calorimeters and the forward detectors. A good understanding of the response of these detectors to high energy electrons is vital, and significant work has been invested to achieve this (see in particular Appendix A). For reconstructing the hadronic part of the event (which is mostly low energy) we rely most heavily on the jet chamber and the electromagnetic calorimetry.

In the OPAL coordinate system the z-direction points in the direction of the electron beam (which was anti-clockwise when viewing LEP from above). The x-axis is horizontal and points towards the centre of LEP. The z-axis is inclined at an angle of 13.9 mrad with respect to the horizontal plane; thus the y-axis is inclined by the same amount with respect to the vertical. The polar angle, θ, is measured from the z-axis, and the azimuthal angle, ϕ, from the x-axis about the z-axis.

3.2.1 Central Tracking System (CT)

Silicon Microvertex Detector (SI)

The silicon microvertex detector [63] was added to OPAL during the 1991/92 shutdown, in between the original beam pipe and a new beryllium beam pipe which had a radius of 5.35 cm. It was designed to measure and identify particles with small decay lengths (≤ 1 cm) such as heavy hadrons and the τ-lepton. The subdetector was made up of two layers of semiconducting silicon wafers which were divided into strips. Each layer had two back-to-back single sided detectors, one giving coordinates in the $r - \phi$ plane and the other the z coordinate. The inner and outer layers were at a radius of approximately 6.1 and 7.5 cm respectively. This subdetector is not used in this analysis.

Vertex Detector (CV)

The vertex detector was a 1 m long, 470 mm diameter, cylindrical drift chamber that was located between the outer (original) beam pipe and the jet chamber. It operated within the common 4 bar central tracking system pressure vessel and contained a mixture of argon, methane and isobutane. An original component of OPAL, it was used to determine the positions of decay vertices of short lived particles and to improve the overall momentum resolution of the central tracking system. It was segmented radially, and had an inner layer of 36 cells with axial wires and an outer layer of 36 stereo cells with wires strung at an angle of 4°. The axial cells provided a measurement of points in the $r - \phi$ plane with a resolution of 50 μm. The combination of the stereo and axial cell information allowed a resolution of 700 μm on the z-coordinate of charged particles close to the interaction region.

Jet Chamber (CJ)

The central jet chamber was a large volume gaseous detector. It recorded the tracks of charged particles and determined their momenta by measuring their curvature in the magnetic field. Particle species identification was provided by measuring the rate of energy deposition, $\mathrm{d}E/\mathrm{d}x$, of particles traversing the chamber. The sensitive volume of the jet chamber was a cylinder of length approximately 4 m, surrounding the beam pipe and vertex detector. The inner diameter was 0.5 m, the outer 3.7 m. The chamber was divided in ϕ into 24 identical sectors, each of which contained a plane of 159 sense wires. All wires were parallel to the beam direction and the wire planes were radial. Cathode wire planes formed the boundaries between adjacent sectors. In the range $43^\circ < \theta < 137^\circ$ 159 points were measured along each track, and at least 8 points on a track were obtained over a solid angle of 98% of 4π. The resolution on the transverse momentum was $\sigma_{p_\mathrm{t}}/p_\mathrm{t} = \sqrt{0.02^2 + (0.0015\, p_\mathrm{t})^2}$ for $|\cos\theta\,| < 0.7$, where p_t is in GeV. The resolution became much worse for larger values of $|\cos\theta\,|$, which includes the region where some of the scattered electrons were measured in this analysis.

Z Chambers (CZ)

The Z chambers were arranged to form a barrel layer around CJ, covering the polar angle range $44° < \theta < 136°$. They improved the polar angle resolution, and hence the invariant mass determination, by making a precise measurement of the z coordinate of charged particles exiting CJ. CZ was made up of 24 chambers, each 4 m long, 50 cm wide and 59 mm thick. The chambers were divided into eight cells in z. Each cell was 50 cm long with six readout wires strung along the ϕ direction. The resolution in z was 100–350 μm.

3.2.2 Timing Counters

The time of flight barrel system (TB) generated trigger signals and allowed charged particle identification in the range 0.6–2.5 GeV by measuring the transit time from the interaction point. It also aided in the rejection of cosmic rays. It consisted of 160 scintillation counters and covered the region $|\cos\theta| < 0.82$, forming a barrel of mean radius 2.36 m outside the solenoid. In addition to this barrel section, a scintillating tile system [64] was installed in the endcap region in 1996. Called the Tile Endcap (TE) system, it provided timing information - allowing the identification of which bunch of a train an event belonged to - and the ability to detect minimum ionising particles.

3.2.3 Electromagnetic Calorimeter

The electromagnetic calorimeter (ECAL) system measured the energies and positions of electrons, positrons and photons ranging from tens of MeV up to beam energy. It was a total absorption calorimeter consisting of three large arrays of lead glass blocks, covering 98% of the solid angle. Since there was about 2 X_0 of material in front of the lead glass, mostly due to the coil and pressure vessel, most electromagnetic showers were initiated before the lead glass itself. Presampling devices were installed in both the barrel and endcap regions, to measure the position and sample the energy of these showers, thereby improving the electromagnetic energy resolution.

Endcap Lead-Glass Calorimeter (EE)

The endcap electromagnetic calorimeters [65], one of which is pictured in Figure 3.4, were used to tag the electron in two-photon collisions in this analysis. Each endcap was composed of 1,132 lead glass blocks assembled in a dome-shaped array and located between the pressure bell of the central tracking system and the pole tip hadron calorimeter. The detector covered the full azimuthal angle and $0.81 < |\cos\theta| < 0.98$ (200–630 mrad). Because of space constraints, the lead glass blocks were mounted coaxially with the beam line.

The 9.2×9.2 cm^2 blocks were manufactured in three lengths (38, 42 and 52 cm) and arranged, following the contours of the pressure bell, so that they presented a total depth of at least 20.5 radiation lengths, and more typically 22 X_0, to all particles coming from the interaction region. The blocks were instrumented with single stage multipliers known as vacuum photo triodes (VPT's), which were developed to be able to operate in the full magnetic field.

The performance of the calorimeter was extensively studied, prior to installation, in π^- and e^- beams. The energy response was found to be linear in the range 3–50 GeV and the energy resolution was $\sigma_E/E \sim 5\%/\sqrt{E}$ (where E is in GeV) at low energies. The spatial resolution was found to be 8–14 mm for a 6 GeV e^- beam incident at 15° to the longitudinal block axes. Two

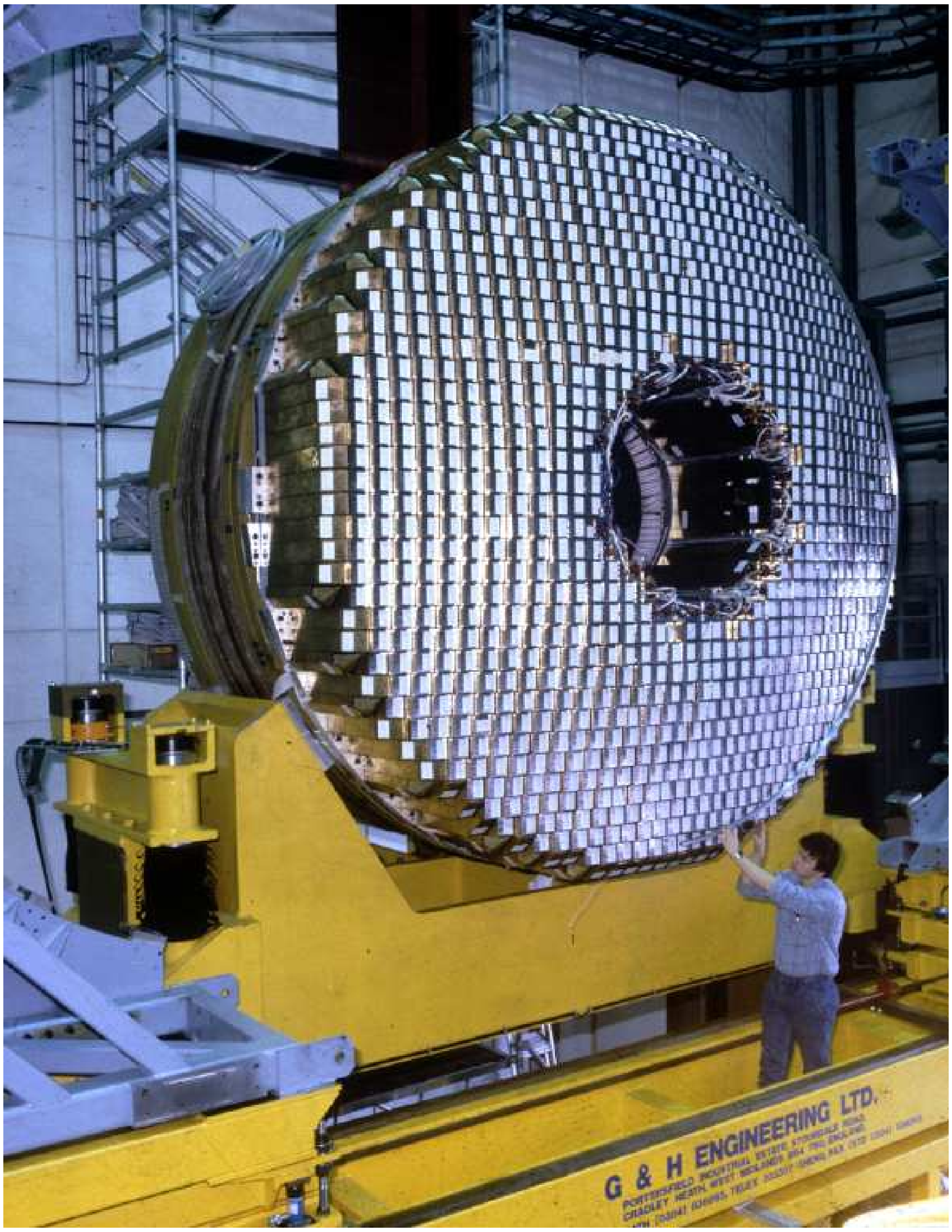

Figure 3.4: One of the endcap electromagnetic calorimeters prior to installation.

separate reference light sources were incorporated into the assemblies. These corresponded to $\sim$10 and $\sim$20 GeV electron equivalents, and were used to monitor the performance of the detector throughout its lifetime.

It is important to note that the resolutions quoted above correspond to the intrinsic resolution of the calorimeter, and not the resolution actually observed once the detector was in situ. This was degraded due to a combination of the material in front of the calorimeter and the severe space constraints in the endcap region, which in some areas led to reduced active material being presented to particles coming from the interaction point. Figure 3.5 shows the number of radiation lengths of material in front of and inside the entire electromagnetic calorimeter. The right hand part of the figure pertains to the EE.

Barrel Lead-Glass Calorimeter (EB)

The barrel calorimeter consisted of a cylindrical array of 9,440 lead-glass blocks of 24.6 X_0, located at a radius of 2.455 m, covering the full azimuthal angle and $|\cos\theta| < 0.98$. In contrast to the endcaps, the blocks were arranged so that they pointed close to the nominal interaction point (but not exactly at it, in order to prevent the escape of neutral particles through the gaps between blocks). Each block was $\sim 10 \times \sim 10$ cm^2 in cross-section and 37 cm in depth. The blocks were instrumented with magnetic field tolerant phototubes. The energy resolution of a prototype barrel section was measured, in a testbeam, to be $\sigma_E/E = 0.2\% + 6.3\%/\sqrt{E}$ (E in GeV) with no material in front of the calorimeter.

Presampler

Behind the TB/TE system and in front of the lead glass calorimeter were the electromagnetic presampler systems. In the barrel, this system was a cylinder

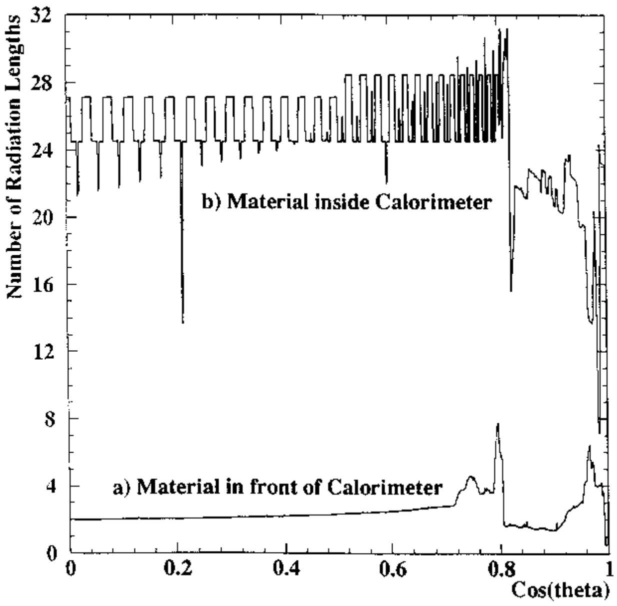

Figure 3.5: "Radiation lengths (a) in front of and (b) inside the active material of the electromagnetic calorimeter as a function of $|\cos\theta|$ at an arbitrary angle in ϕ. The peaks in the material in front of the calorimeter at $|\cos\theta| \sim 0.8$ and ~ 0.96 arise from the structure of the pressure bell of the central tracking system. The structure in the active material of the calorimeter arises, for $|\cos\theta| < 0.8$ from the quasi-pointing block geometry, at $|\cos\theta| = 0.8$ from the barrel/endcap overlap and transition, and at $|\cos\theta| \sim 0.975$ from the endcap/gamma-catcher/forward calorimeter overlap and transition." (from [62])

of gaseous wire chambers working in limited streamer mode. In the endcap region the presampler was an umbrella shaped arrangement of thin gaseous multiwire chambers which were operated in a high gain mode. Combining the information from the presampler with that from the calorimeter provides an improved energy resolution on a shower by shower basis, because the number of charged particles passing through the presampler is approximately proportional to the energy deposited in the material traversed before the presampler. However, because of reliability issues, the presamplers were not used in this analysis.

3.2.4 Hadronic Calorimeter

The hadron calorimeter (HCAL) measured the energy of hadrons that penetrated the electromagnetic calorimeter. The iron of the return yoke was segmented into layers, with planes of wire chambers between each layer, and formed a cylidrical sampling calorimeter about 1 m thick. To achieve good coverage in solid angle, the detector was constructed in three parts - the barrel, the endcaps and the pole tips - presenting at least 4 interaction lengths of absorber over 97% of 4π. Most hadronic showers were initiated in the 2.2 interaction lengths of material in front of the hadronic calorimeter, so the overall hadronic energy was determined by combining information from both the electromagnetic and hadron calorimeters.

3.2.5 Muon Chambers

The outermost layer of the OPAL detector was the muon detector, which consisted of a system of large-area gaseous chambers constructed as a barrel and two endcaps. It covered the iron yoke almost completely. The amount of material that a particle had to traverse before reaching the muon chambers exceeded the equivalent of 1.4 m of iron (over 7 X_0 for pions). While muons penetrated to the muon detector and left a single clean track, the probability of a pion not interacting, thus faking a muon, was less than 0.001. The muon chambers are not used in this analysis.

3.2.6 Forward Region

Detectors in the forward region extended the electromagnetic calorimetric coverage of OPAL to low angles with respect to the beam line. They are used in this analysis to tag scattered electrons from two-photon collisions, but their main purpose was to provide precision measurements of the luminosity delivered to OPAL by counting small-angle Bhabha scattering events. Of relevance to this analysis is the fact that hadronic showers were not well contained by these electromagnetic calorimeters, resulting in poor hadronic energy measurement in the forward region. A diagram of the layout of the forward region is shown in Figure 3.6.

Forward Detector (FD)

The FD consisted of four separate parts: the main calorimeter, the tube chambers, the gamma catcher and the far forward monitor. Two further original components, the drift chambers and the fine luminosity monitor, were removed to make room for the silicon tungsten calorimeter (see below) and will not be discussed further. The two FD assemblies, one situated at each end of the OPAL detector, were symmetric about the interaction point.

The forward calorimeter consisted of 35 layers of lead-scintillator sandwich, presenting a total of 24 X_0 to electrons coming from the interaction point. The first 4 X_0, the presampler, was read out with wavelength shifter on the outside only, but the rest of the calorimeter was read out on both the inner and outer edges. The calorimeter was divided into 16 azimuthal segments and the azimuthal resolution, from the ratio of signals in adjacent segments,

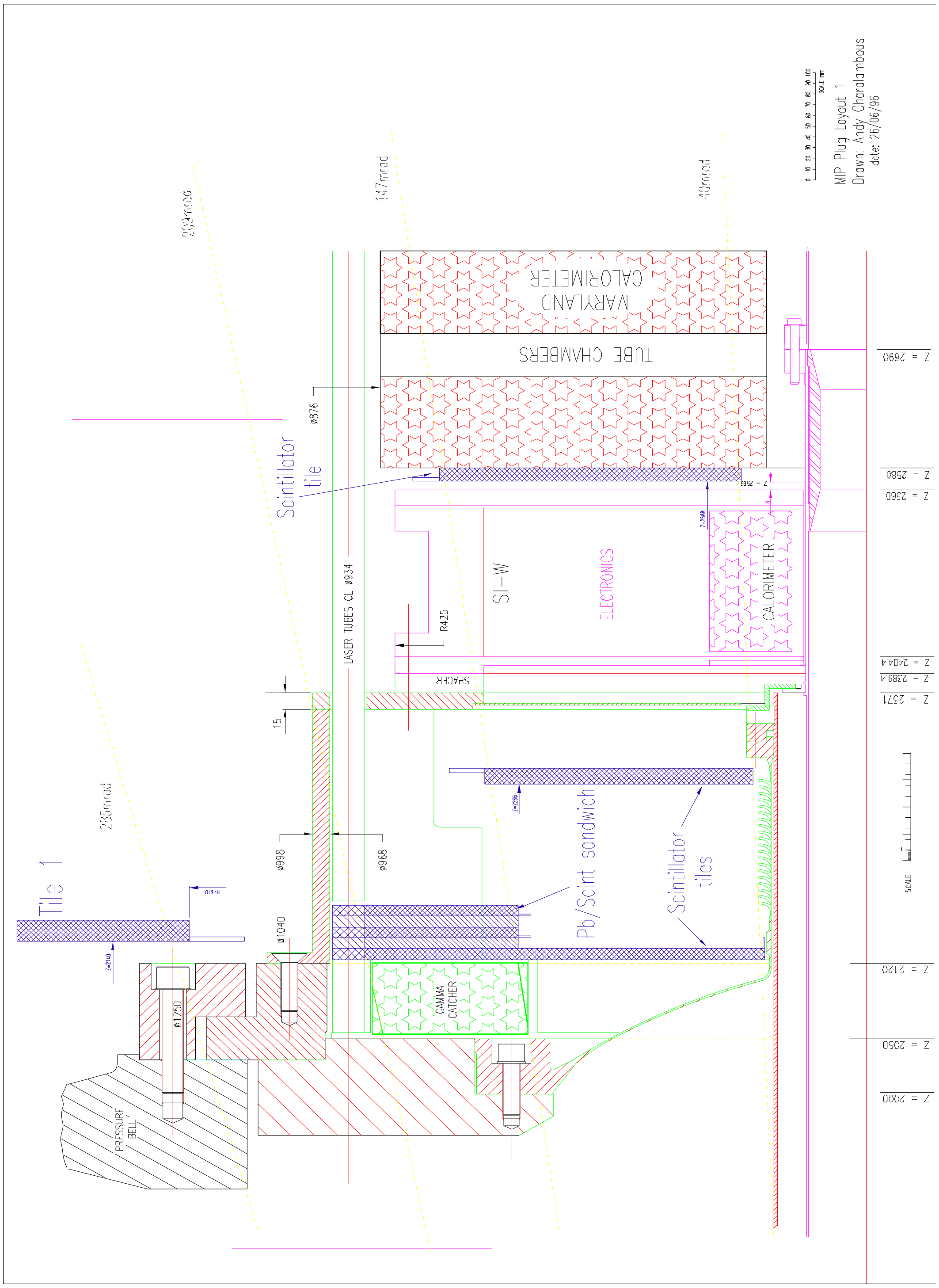

Figure 3.6: A cross-section view of the forward region in OPAL.

was $\pm 1.5°$. The energy resolution was measured to be $\sigma_E/E \sim 17\%/\sqrt{E}$ (E in GeV) and the radial position resolution on electron showers, using the ratio of the inner to outer signals, was ± 2 mm. There was clean acceptance for particles from the interaction region for $60 < \theta < 120$ mrad. The tube chambers, located between the presampler and the rest of the main calorimeter, consisted of three planes of proportional tubes, with two layers aligned at right angles and the third at $45°$ to the other two. They improved the position resolution to about 2 mrad in both θ and ϕ.

The gamma catcher, a non-containing lead-scintillator ring of 7 X_0, filled the gap between the EE and the main FD calorimeter. The far forward monitors were two small lead-scintillator calorimeters mounted on either side of the beam pipe at ± 7.85 m from the interaction point. They were used to provide a high statistics online luminosity measurement, and also to tag very low-angle ($5 < \theta < 10$ mrad) electrons. Neither of these last two components were used in this analysis.

Silicon Tungsten Calorimeter (SW)

In order to provide a higher statistics luminosity measurement, the FD was supplemented from 1993 by the silicon tungsten luminometers [66]. The SW consisted of two cylindrical small angle calorimeters encircling the beam pipe at ± 2.39 m in z from the interaction point and had an angular acceptance of $33 < \theta < 59$ mrad. They were sampling calorimeters presenting 22 radiation lengths, consisting of 18 passive layers of tungsten and 19 active layers of silicon. Each layer consisted of 16 wedges which were segmented into pads that were read out individually. The radial position resolution on electron showers was typically 0.06 mrad and the energy resolution approximately 6% at LEP2.

3.2.7 The Trigger

The OPAL trigger system [67] was designed to reduce the 45 kHz LEP bunch crossing frequency to a manageable rate of $\sim$10 Hz, by making a rapid decision on whether a bunch crossing might contain an interesting physics event. It was also used to reject backgrounds arising from cosmic rays, beam-gas interactions and subdetector electronics noise. Most physics events would be triggered by a number of independent conditions imposed on the subdetector signals. Such redundancy leads to a high trigger efficiency and is greatly beneficial to the estimation of this efficiency.

The various trigger signals were combined in a flexible manner in the central trigger logic. The 4π solid angle of the detector was divided into 144 overlapping bins, 6 in θ and 24 in ϕ. Events were triggered by certain programmable coincidences in the same θ–ϕ bin. In addition, the subdetectors delivered stand-alone signals, based on total energy or track multiplicity sums, which could also trigger the readout of the detector. The trigger signals important to this analysis are listed in Table 3.1. A trigger decision would be reached approximately 15 μs after the bunch crossing, and it took about 4.5 μs to reset the subdetectors, if appropriate.

3.2.8 Data Acquisition

When a positive trigger decision was made, data from all the individual subdetectors would be read out, combined and then passed to the filter. The filter was able, by partially reconstructing events, to make a more sophisticated decision than the trigger on whether an event should be kept. Events not rejected by the filter would then be passed to the ROPE (Reconstruction of OPal Events) farm of HP workstations, which reconstructed individual events and archived them for offline analysis.

Trigger name	Subdetector	Description
SWHIOR	SW	Total energy at either end $\geq$ 34 GeV
FDHIOR*	FD	Total energy at either end $\geq$ 35 GeV
EEL(R)HI*	EE	EM energy in left (right) endcap $\geq$ 2.4 GeV
EEL(R)LO	EE	EM energy in left (right) endcap $\geq$ 1.6 GeV
TPEML(R)	EE	Energy in 1 ϕ bin $\geq$ 0.75 GeV
EBTOTLO	EB	Total EM energy in barrel $\geq$ 1.8 GeV
EBWEDGE	EB	Energy in 'wedge' $\geq$ 2 GeV
EB1	EB	≥ 1 ϕ bin
TBM1(2,3*)	CT	≥ 1 (2,3) barrel tracks
TPTTR(L)	CT	≥ 1 ϕ bin in θ_1 (θ_6)
TPTT1	CT	≥ 1 θ–ϕ bin
TPTTTOB	CT/TB	≥ 1 θ–ϕ coincidence in barrel
TPTTEM*	CT/ECAL	≥ 1 θ–ϕ coincidence
TPTOB	TB	≥ 1 ϕ bin
TPTOEMB	TB/EB	≥ 1 θ–ϕ coincidence
TBEBS	TB/EB	Same ϕ sectors hit

Table 3.1: Description of selected OPAL trigger signals. The exact values of the energy thresholds varied slightly from year to year - those given here are for 1998. Triggers marked with an asterisk were stand-alone, while the others required coincidences with other triggers.

Chapter 4

Monte Carlo Simulation

Monte Carlo programs are a crucial part of the analysis presented here. Not only are they used to refine the event selection, to determine the selection efficiency for signal events and to estimate physics backgrounds, but they are also required as an input to the unfolding procedure, to determine the correlation between the measured and true x distributions (see Section 7.1). It is therefore important to have Monte Carlo models which give a good description of $\gamma^{\star}\gamma$ events, and in particular of the angular distribution of hadrons in the final state. This is not a trivial ambition, since we are dealing with non-perturbative QCD and multi-particle final states, meaning that any model has to use a series of approximations and assumptions.

The main signal Monte Carlo generator used in this analysis is HERWIG 5.9+k_{t}(dyn) [68]. It is common to use a second Monte Carlo model to estimate the systematic uncertainty introduced to the unfolding because of different assumptions about the modelling of the hard scattering and the hadronisation process. For this purpose, either the PHOJET 1.05 [69] generator or the Vermaseren [70] program is used, depending on the Q^2 region being studied. These programs are described in more detail in the following.

4.1 HERWIG

HERWIG is a general purpose QCD Monte Carlo generator which includes electron-photon DIS. Its general philosophy is to provide the most complete treatment possible of perturbative QCD, combined with a simple model for soft interactions. It does this uniformly for any combination of lepton, hadron or photon scattering, allowing the free parameters to be tuned to one reaction, for example e^+e^- annihilation or pp scattering, and then applied to other reactions. This is a strong advantage, which lends confidence to the description of the underlying physics, since in a dedicated two-photon generator (as used in all measurements of F_2^γ until relatively recently) one can only tune the parameters to the very thing one is trying to measure, possibly biasing the measurement. HERWIG bases the event generation on the fact that an event can be factorised into several separate stages. These are:

- the production of a quasi-real photon from one of the beam electrons,
- the elementary hard sub-process,
- initial and final state QCD radiation (parton showers),
- the hadronisation process.

The target photon is generated according to the EPA (Equation 2.4), producing the correct P^2 dependence, although the second term (of order m_e^2/P^4) is neglected. The event is then described as deep inelastic scattering $e\gamma \rightarrow eX$ including the full electron kinematics. The hard process is simulated as $eq \rightarrow eq$ scattering, with the momentum fraction of the incoming quark generated according to a given set of parton distribution functions of the real ($P^2 = 0$) photon. The scattering is calculated using the LO matrix element. HERWIG does include a simple model to generate soft interactions between the photon remnant and its nearest neighbour - known as the 'soft underlying event' - but this option is not recommended for DIS events and was not used in the samples generated for this analysis.

The participant quark in the hard scattering may emit QCD radiation before or after the scatter, with the probabilities of such emissions governed by the DGLAP splitting functions. The accurate treatment of the perturbative phase of these parton showers is one of the main emphases of HERWIG. For both the initial and final state parton showers (ISPS and FSPS), the evolution is calculated downwards in scale, away from the hard scatter, using the transverse momentum as the evolution parameter and obeying angular ordering. This means that the ISPS uses a 'backward evolution' algorithm, back towards the incoming photon. The ISPS is analogous to the case of ep DIS - using NLO matrix elements for the processes $q \to qg$ and $g \to q\bar{q}$ - with the addition of the $\gamma \to q\bar{q}$ vertex. The evolution continues by the emission of partons at successively lower angles, either until the quark is evolved back to the incoming photon, or until the cut-off scale is reached. In the former case the event is classified as point-like, otherwise it is hadron-like (note that this separation is different to the choice made in the parton distribution functions). The photon remnant will have a larger transverse momentum for point-like events, as given by perturbative QCD; for hadron-like events the remnant is given a transverse momentum k_t with respect to the direction of the incoming photon. The backward evolution algorithm ensures that, at each branching, the parton distributions agree with the input parton distribution functions. All partons produced in the ISPS undergo further showering just like any other outgoing parton.

The FSPS is identical to the case of e^+e^- annihilation, and continues until the infrared cut-off is reached. At this point non-perturbative confinement effects are considered to take over and the program switches to the hadronisation phase. HERWIG uses the cluster fragmentation model [71], Figure 4.1(a), to perform the conversion of all of the partons produced in the initial and final state showers, plus the photon remnant, into hadrons. In this model any gluons remaining from the parton shower are split non-perturbatively into quark-antiquark pairs. Colour singlet clusters are then formed from neighbouring quarks and antiquarks (not coming from the same gluon), carrying the combined flavour and four-momentum of the pair. In the simplest case these clusters then decay isotropically in their rest frame into pairs of hadrons, with branching ratios determined by density of states. If a cluster is too light to decay into two hadrons, it is converted to the lightest single hadron of its flavour, with the extra four-momentum donated to a neighbouring cluster. A small fraction of clusters may be too heavy for two-body decay to be a reasonable ansatz; these are fragmented collinearly into two lighter clusters.

4.1.1 The k_{t}(dyn) modification

The default version of HERWIG 5.9 was found [72] to exhibit a less point-like behaviour than the data in certain variables relating to the hadronic final state. In a first attempt to improve the description of the data, the distribution of transverse momenta, k_t, of the photon remnant in hadron-like events was altered from the program default. The default Gaussian behaviour was replaced by a function of the form $\mathrm{d}k_t^2/(k_t^2 + k_0^2)$, with $k_0 = 0.66$ GeV, motivated by the observation that such a form improves the description of the data in photoproduction studies at HERA [73]. Originally, the upper limit on k_t was fixed at 5 GeV, but this was found to introduce too much transverse momentum for low Q^2 events. An improved description of the data was achieved [74] by dynamically (dyn) adjusting the upper limit of k_t according to the hardest scale in the event, which is of order Q^2. This leads to the version known as HERWIG 5.9+k_{t}(dyn), which is used throughout this analysis.

4.2 PHOJET

The general purpose Monte Carlo program PHOJET 1.05 is designed to model hadronic pp, γp and $\gamma\gamma$ interactions, based on the Dual Parton Model [75]. It was originally designed for real photon collisions, but can be applied to eγ

DIS by extrapolating the $\gamma\gamma$ cross-section in Q^2 on the basis of the Generalised Vector Dominance model [76]. The basic stages in the event generation are similar to those in HERWIG, with the key differences detailed below.

In PHOJET, both the target and probe photons are generated through the use of the full EPA (Equation 2.4). The hard interaction is simulated not as DIS, but as a combination of direct ($\gamma\gamma \rightarrow q\bar{q}$) and resolved ($\gamma g \rightarrow q\bar{q}$ and $\gamma q \rightarrow gq$) processes. The LO matrix elements for real photons are used to calculate these contributions. The detailed treatment of diffractive and soft processes is a main focus of PHOJET. Soft interactions are modelled through Regge phenomenology, including reggeon and pomeron exchanges, with photon-hadron duality assumed and the cross-sections tuned to pp and γp data. The soft and hard regions are separated by a p_{t} cut of 2.5 GeV, with the model constructed to give a smooth transition between the two. Note that the cut-off means that for $W < 5$ GeV only soft processes are generated.

The sum of the processes is matched to the input parton distribution function, but because the program is not based on the DIS cross-section formula the output distribution is not that which one would expect given the input structure function. This means that in order to use the program as input to an unfolding, the events need to be reweighted to match a known distribution. In this analysis we choose to reweight to the HERWIG x distribution. What this means in the end is that only the transformation matrix relating the measured x to the true value is determined from PHOJET, and the efficiency correction is always based on HERWIG.

All hard photon interactions are combined with leading-log parton showers. PHOJET models initial state parton showers in a manner similar to HERWIG, using a backward evolution algorithm with transverse momentum as the evolution parameter and obeying angular ordering. The final state parton shower and hadronisation is implemented by the widely-used JETSET program [77]. JETSET uses the string fragmentation model [78], Figure 4.1(b),

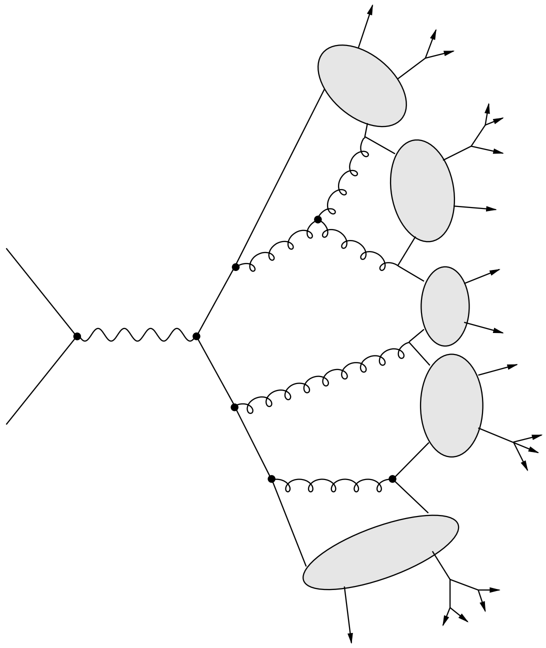

(a)

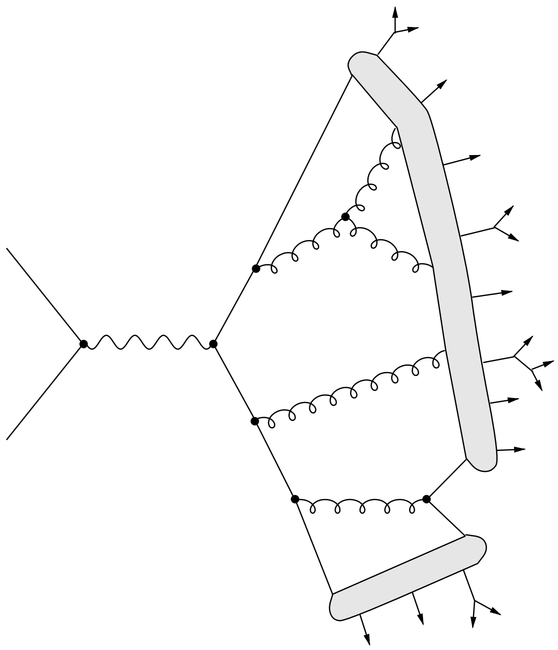

(b)

Figure 4.1: Schematic diagrams of a final state parton shower with (a) cluster and (b) string hadronisation in e^+e^- annihilation. Taken from Reference [79]

in which pairs of quarks in the final state are connected by colour strings. Final state gluons appear as kinks in the string. The photon remnant is treated as any other parton. The string has a uniform energy per unit length, which is consistent with hadron spectroscopy data. As quarks move apart, they give energy to the string (or colour field), which eventually breaks up into hadron-sized pieces through $q\bar{q}$ pair creation in the intense colour field.

4.3 Vermaseren

The author of PHOJET recommends that it be used only for Q^2 values lower than about 50 GeV^2. In this analysis it is used up to 150 GeV^2, but an alternative generator is needed for higher values. The choices are severely limited, but the situation is improved by the fact that the point-like part of F_2^γ is expected to dominate at high Q^2. Thus a generator based only on the point-like part can be expected to give an adequate description of the data, given the proviso that it will only be used to estimate the systematic uncertainty on a measurement that will be dominated by the statistical error.

The Vermaseren program is a QED generator, which is regarded as the standard Monte Carlo for lepton pair production in two-photon collisions. It uses the exact $2 \rightarrow 4$ matrix element to calculate the multiperipheral diagram (i.e. the EPA is not required, and the complete dependence of the cross-section on the photon helicity is modelled). When given quark masses, charges and colour factors it can be run as a QPM generator. The outgoing quark pair is passed to JETSET which initiates the final state parton shower and string hadronisation. There is no initial state shower.

4.4 Detector Simulation

In order to compare events generated by Monte Carlo programs with real data events, it is necessary to have some way of knowing what the Monte Carlo events would look like had they been 'seen' by the OPAL detector. The standard tool used to achieve this is the GEANT (Generation of Events ANd Tracks) package [80]. This program provides a framework for the definition of the detector geometry, and controls the tracking of particles through this geometry using well-tested routines to simulate interactions with the matter of the detector. The GEANT-based program which implements the simulation of the OPAL detector is called GOPAL [81].

The GOPAL simulation of the detector response to Monte Carlo events involves several steps. First there is an initialisation stage, in which the geometrical form of the detector is specified in the form required by GEANT. This involves the description of the detector in terms of the juxtaposition of geometrical volumes. A medium-number is assigned to each volume, with each medium characterised by a set of parameters describing its interactions with traversing particles. The description of the original OPAL detector required the definition of 49 media and 68 413 volumes, which covered the different subdetectors as well as passive elements such as the beam pipe, magnet coil and support structures.

The program then loops over the generated events in three stages. First the kinematics of the particles forming the event are obtained, usually from the output of a separate generator. Then each of the particles is tracked through the detector in steps, taking into account geometrical volume boundaries and physical effects depending upon the nature of the particles themselves, their interactions with matter and with the magnetic field. When a particle traverses a sensitive region of the detector suitable information (known as *hits*) - e.g. position, energy loss - is stored. At the end of tracking this information is processed for each subdetector in turn and folded with models which sample the response of the detector. Thus the final output is simulated raw data which is stored in the same format as if it had emerged from the OPAL detector itself, with some additional information such as the initial kinematics of the generated event and 'cheat information' (the true association between particles and hits).

4.5 Samples Generated

Details of the $\gamma^{\star}\gamma$ signal Monte Carlo samples used for this analysis are given in Table 4.1. These samples were all passed through the full GOPAL simulation. The HERWIG 5.9+k_{t}(dyn) and PHOJET 1.05 samples were generated with the restrictions that Q^2 be greater than, and P^2 less than, 4.5 GeV^2. W was required to be greater than 1.73 GeV and the GRV LO parameterisation, taken from the PDFLIB library [82], was used as the input structure function. The numbers given for the cross-sections and integrated luminosities correspond to the phase space defined by these cuts. Details of the PHOJET samples are not given in the table because the version used does not give a useful cross-section in its output. This is not a problem because the PHOJET x distribution is reweighted to match that of HERWIG, so the cross-section is not needed for the unfolding. The number of generated events at each energy is the same as the corresponding HERWIG sample.

The Vermaseren signal samples were generated separately for light and for charm quarks. The u quark samples were generated with Q^2 greater than 150 GeV^2, P^2 less than Q^2 (events with P^2 larger than 4.5 GeV were removed from the signal sample at a later stage of the analysis), and W greater than 1.73 GeV. The quark mass used was 0.325 GeV and the cross-section for three light quarks was obtained simply by multiplying the output cross-section by 9/8 (see Equation 2.14). For these samples, the quoted cross-sections in Table 4.1 are just for u quarks, whereas the integrated luminosities correspond to $u + d + s$ quarks. The cuts specified for the charm quark samples were: $Q^2 > 4.5$ GeV^2, $P^2 < 4.5$ GeV^2 and $W > 2\,m_{\mathrm{c}}$, where $m_{\mathrm{c}} = 1.5$ GeV.

$\sqrt{s}$	HERWIG 5.9+k_t(dyn)			Vermaseren $u\bar{u}$			Vermaseren $c\bar{c}$		
[GeV]	Events	σ [pb]	$\int \mathcal{L}$ [pb^{-1}]	Events	σ [pb]	$\int \mathcal{L}$ [pb^{-1}] (u, d, s)	Events	σ [pb]	$\int \mathcal{L}$ [pb^{-1}]
183	150k	296.0	503	10k	2.46	3613	50k	36.3	1377
189	520k	305.8	1701	28k	2.55	9760	50k	37.0	1351
192	80k	310.4	258	3k	2.60	1026	50k	36.8	1359
196	310k	310.0	1000	10k	2.65	3354	50k	38.6	1295
200	314k	314.0	1000	6k	2.66	2005	50k	38.5	1299
202	100k	322.2	310	5k	2.67	1665	50k	38.3	1306
205	330k	324.6	1017	-	-	-	-	-	-
206	-	-	-	30k	2.76	9662	50k	38.4	1302
207	450k	326.8	1377	-	-	-	-	-	-
Totals	2254k	-	7166	92k	-	31 085	350k	-	9289

Table 4.1: Details of the signal Monte Carlo samples generated: the numbers of events generated, the cross-sections given by the generators and the corresponding integrated luminosities. See the text for details of the phase spaces to which these numbers correspond. The number of PHOJET events generated at each energy is the same as for the corresponding HERWIG sample.

Chapter 5

Event Selection

5.1 Data Samples

This analysis uses data taken by the OPAL detector during the final four years of LEP data-taking, when the accelerator was operating at its highest energies and luminosities. Three samples of events are studied, classified according to the subdetector in which the scattered electron is observed. Electrons are tagged in the SW, FD and EE detectors. Because the $\gamma^{\star}\gamma$ cross-section varies only logarithmically with $\sqrt{s_{ee}}$, the data from different years is combined in order to make full use of the available statistics.

5.2 Event Reconstruction and '$\gamma\gamma$ ntuples'

The 'offline ROPE' software package [83] is used to analyse raw OPAL data, both real and simulated. The OPAL gamma-gamma analysis group [84] has used this framework to produce a set of common ntuples that can in principle be used for any type of two-photon analysis. Data ntuples contain all events that have been flagged by ROPE as possible two-photon events (whether containing tagged electrons or not), using extremely loose criteria. Monte Carlo ntuples contain simulated events. For each event the ntuples contain, among other things, lists of tagged electron candidates, tracks and unassociated clusters, particle identification information and, for Monte Carlo, the generated four-vectors (i.e. before simulation). Only tracks and clusters satisfying certain quality criteria end up in the final list, and the requirements are detailed in the following three sections.

5.2.1 Track quality requirements

Quality criteria are applied to tracks in order to ensure that their momentum is reliably measured, and to reject tracks that do not arise from e^+e^- interactions (e.g. cosmic rays, beam-gas interactions). The requirements used in the $\gamma\gamma$ ntuples are:

- a transverse momentum of at least 120 MeV;
- a polar angle satisfying $|\cos\theta| < 0.9622$;
- at least 20 hits in CJ;
- a number of hits in CJ of at least half that expected for a track at the same polar angle;
- a point of closest approach to the origin of less than 25 cm in the z direction and less than 2 cm in the r–ϕ plane;
- a first measured point in CJ at a radius of less than 75 cm.

5.2.2 Cluster quality requirements

There are also quality requirements for clusters, to ensure that they are not due to noisy electronics. All clusters are compared to a list of known noisy ('hot') clusters, and the cluster is rejected if its energy is close to that expected from the noise. Electromagnetic clusters have to exceed energy thresholds of 100 MeV in the EE, 250 MeV in EB, 1 GeV in FD and 2 GeV in the SW detector. Clusters in the hadronic calorimeters must have an energy of at least 600 MeV (2 GeV in the pole tips).

5.2.3 Track-cluster matching

Charged particles can, of course, give rise to both tracks and calorimeter clusters. If this is the case, to use both would be double-counting, so matching of tracks and clusters must be performed. Within OPAL this is done using the MT package [85], which matches tracks and clusters in the same θ–ϕ region. It loops over the tracks and disregards matching clusters whose energy is less than that expected for the track (plus a certain tolerance). If a match is found, but the cluster has too large an energy to be accounted for by the track alone, then the energy expected from the track is subtracted from the cluster. The remaining energy is assumed to be due to a neutral particle. In the matching process tracks are assigned the pion mass and unassociated clusters are assumed to be photons (i.e. massless).

5.3 Subdetector Status

For every data event, each subdetector is given a code to indicate its status. The meanings of these status codes are given in Table 5.1. Different analyses make use of different parts of the detector, so no requirements are placed on these codes in the $\gamma\gamma$ ntuples. However, in this analysis a status code of 3 is required for a number of vital subdetectors. These are the tagging detectors (SW, FD and EE), the barrel electromagnetic calorimeter EB, and the tracking detectors CV and CJ.

Status code	Meaning
0	dead or off
1	unreliable
2	minor problems
3	fully functional

Table 5.1: Descriptions of the subdetector status codes.

5.4 Calculation of W_{vis}

An important quantity in this analysis is the invariant mass of the hadronic final state, W_{vis}, which is used both in the event selection and to calculate x from Equation 2.7. W_{vis} is given by

$$W_{\text{vis}} = \sqrt{(\sum_i E_i)^2 - (\sum_i p_{i,x})^2 - (\sum_i p_{i,y})^2 - (\sum_i p_{i,z})^2}\,, \tag{5.1}$$

where i runs over all tracks and unassociated clusters (except that which produced the tagged electron), including those in the FD and in the side of SW opposite to that in which the scattered electron is observed. A correction algorithm [86], obtained from Monte Carlo studies of the detector response to hadrons, is applied to clusters in FD to correct for losses in the measurement of the hadronic energy in this electromagnetic calorimeter.

For the EE sample, because of the high probability that the scattered electron will shower in the dead material in front of the EE calorimeter (see Figure 3.5), energy deposits close to the electron are likely to belong to the electron. Even though they are generally low energy, they can strongly distort the measured W_{vis} because of the large angle with respect to the rest of the hadronic final state. Therefore, for this sample, all tracks and clusters within a cone of 200 mrad half-angle about the direction of the electron candidate are excluded from the calculation of W_{vis}. This automatically excludes any track left by the tagged electron, which should be present for clusters with polar angle greater than about 275 mrad, as well as any leakage of the electron's energy into the HCAL. The size of the exclusion cone was chosen after a study of Bhabha events - see Appendix A for details. Study of HERWIG signal events indicates that only 0.2% of events have anything from the hadronic final state within 200 mrad of the tag.

5.5 Final Selection

The final samples of events are selected by applying cuts on the scattered electrons and on the hadronic final state. The cuts are chosen in order to obtain as pure a sample of signal $\gamma^{\star}\gamma$ events as possible while minimising the inevitable loss of efficiency. Cuts are applied on the following variables:

- the energy of the tagged electron cluster, E_{tag}, normalised to the beam energy, E_{b};
- the polar angle of the tagged electron with respect to the closest beam axis, θ_{tag};
- the energy of the most energetic electromagnetic cluster in the hemisphere of the detector opposite the tag, E_{a}, normalised to E_{b};
- the track multiplicity, N_{trk}, excluding (for the EE sample) any track belonging to the tagged electron;
- the number of tracks identified as electrons from their $\mathrm{d}E/\mathrm{d}x$ weight;
- the invariant mass of the hadronic final state, W_{vis}.

For the EE sample only, an additional cut is applied on the energy deposited in a cone of 500 mrad half angle about the tag cluster (called the 'electron isolation' cut). The cuts applied to each of the data samples are listed in Table 5.2.

The polar angle cuts ensure that the tag is detected within the clear acceptance of the tagging calorimeter. In the case of the EE, the inner edge of the detector is not used because its resolution is very poor, and badly modelled in the detector simulation, and the upper θ_{tag} cut is determined by the point at which the signal becomes less important than background. The cut on the track multiplicity is designed to ensure that the event is hadronic. The stronger cut on the EE sample reflects the fact that a larger proportion of the final state particles are likely to be detected, and a genuine hadronic $\gamma^{\star}\gamma$ event is unlikely to have only 3 charged particles in the hadronic final state - whereas Bhabha scattering frequently gives signal-like events with 3 charged particles. The lower cut on W_{vis} removes the region of resonance production in two-photon collisions, which is very difficult to model properly in the Monte Carlo. The remaining cuts are specifically to remove background and are discussed in the following section. Details of the final samples are given in Table 5.3, and the highest Q^2 event is shown in Figure 5.1.

Cut	SW	FD	EE
$E_{\rm tag}/E_{\rm b}$ min	0.75		0.70
$\theta_{\rm tag}$ min [mrad]	33.25	60	230
$\theta_{\rm tag}$ max [mrad]	55	120	500
$E_{\rm a}/E_{\rm b}$ max	0.25		
$N_{\rm trk}$ min	3		4
	(2 non-electron tracks)		
$W_{\rm vis}$ min [GeV]	2.5		
$W_{\rm vis}$ max [GeV]	60		50
Electron isolation [GeV]	-		≤ 3.0

Table 5.2: The selection cuts applied to each data sample.

Year	$\sqrt{s}$ [GeV]	Integrated Luminosity [pb^{-1}]	Selected events SW	FD	EE
1997	183	40.6	1927	825	26
1998	189	168.6	7671	3375	118
1999	192–202	206.6	9078	3829	132
2000	200–209	215.8	9143	3845	138
Totals		631.6	27819	11874	414

Table 5.3: The e^+e^- centre-of-mass energy, integrated luminosity and number of selected events in each data sample, separately for each year's data taking and in total.

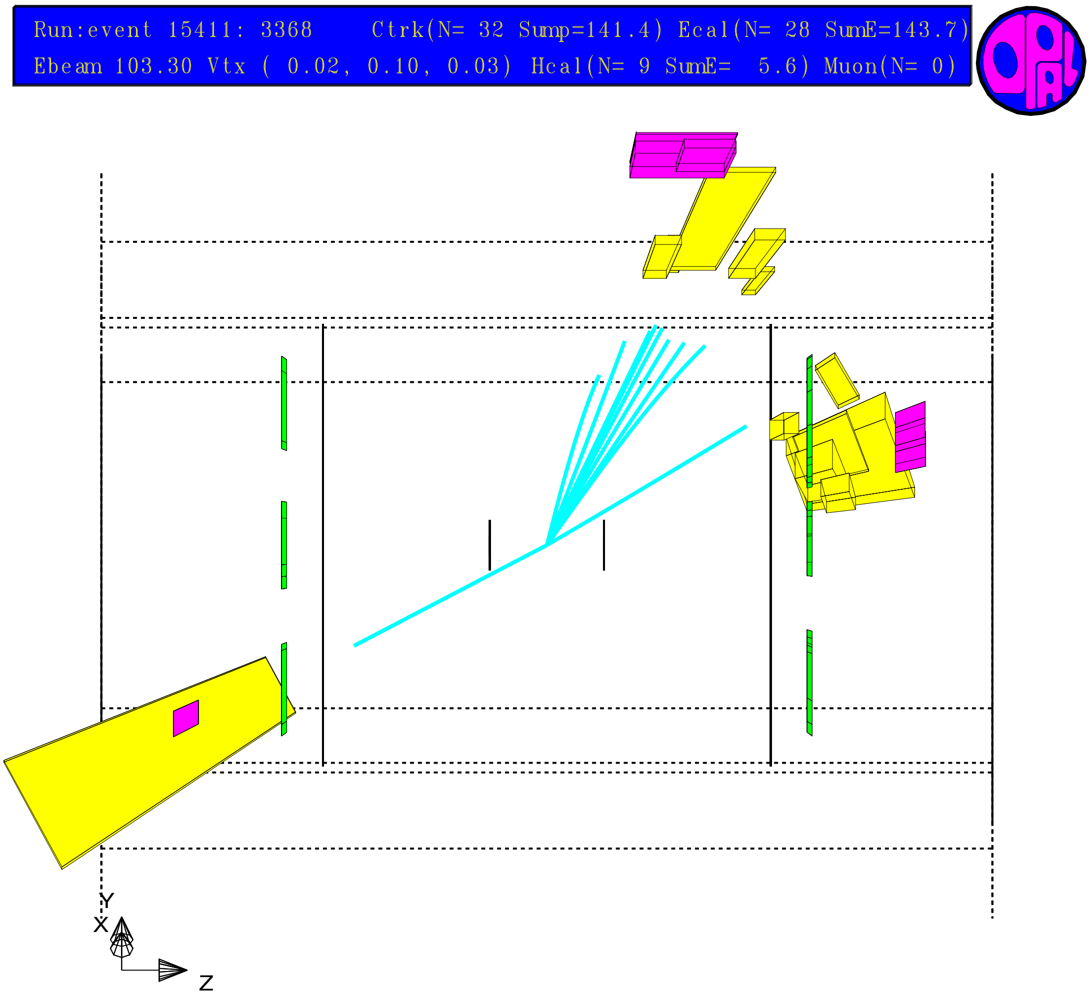

Figure 5.1: OPAL event display picture of the selected event with the highest measured Q^2 (2323 GeV^2). The large electromagnetic cluster on the left, along with its associated track, has been left by the scattered electron. The small pink block indicates that some of the electron's energy has leaked into the HCAL. The two jets of particles on the right compose the hadronic final state. All but one of the particles in one of the jets has a polar angle below the region of good tracking.

5.6 Backgrounds

Even with optimised cuts, it is impossible to completely eliminate all sources of background. The contribution to the background from all standard model processes was checked using standard OPAL Monte Carlo samples. The details of these samples are given in Table 5.4, along with the estimated number of events remaining in each data sample after all cuts. The major sources are subtracted from the data when measuring F_2^γ and are discussed further in the following.

5.6.1 Leptonic final states in two-photon collisions

These events are very similar to signal $\gamma^\star\gamma$ events, except that a pair of leptons are produced in the two-photon collisions instead of two quarks. With the presence of a tagged electron, these events need to be rejected by some requirement on the 'hadronic' final state. The electron and muon-pair events have only two particles in this final state, so in the vast majority of cases fail the multiplicity cut. However, extra tracks are possible from, for example, converted bremsstrahlung photons or bad reconstruction of a track. This is much more likely for electrons, and so the additional cut on the number of identified electrons further reduces this background. The tau-pair events that survive the multiplicity cut constitute a virtually irreducible background, but being purely QED in nature they are reliably modelled in the Monte Carlo. This is the dominant background in the SW and FD samples.

Background	SW	FD	EE	Generator	Simulated Integrated Luminosity [pb^{-1}]
$\gamma^{\star}\gamma \rightarrow \tau^{+}\tau^{-}$	1309.3±14.1	845.5±11.3	31.8±2.2	Vermaseren	5957
$\gamma^{\star}\gamma \rightarrow \mu^{+}\mu^{-}$	16.6±2.2	8.6±1.6	0	BDK [87]	2208
$\gamma^{\star}\gamma \rightarrow \mathrm{e}^{+}\mathrm{e}^{-}$	87.9±5.3	51.2±4.1	0.3±0.3	Vermaseren	1962
$\gamma^{\star}\gamma^{\star} \rightarrow$ hadrons	321.3±4.7	193.4±3.7	5.0±0.3	PHOJET 1.10/Vermaseren	9055/31085
$\gamma\gamma \rightarrow$ hadrons	0	3.5±3.5	0	PHOJET 1.10	178.8
$\mathrm{Z}^{0}/\gamma^{\star} \rightarrow$ hadrons	82.8±2.4	124.6±3.1	76.2±2.4	PYTHIA [88]	10360
$\mathrm{Z}^{0}/\gamma^{\star} \rightarrow \tau^{+}\tau^{-}$	7.9±0.3	10.5±0.4	10.6±0.4	KK2f [89]	60519
4f $\mathrm{e}^{+}\mathrm{e}^{-}\mathrm{q}\overline{\mathrm{q}}$	27.0±0.9	48.2±1.1	16.6±0.7	GRC4f [90]	34962
radiative Bhabha	11.9±2.3	13.3±2.5	0.9±0.6	TEEGG [91]	1380

Table 5.4: The estimated number of background events in each data sample with details of the Monte Carlo samples used in the estimation.

5.6.2 Hadron production from e^+e^- annihilation

A hadronic annihilation event (Figure 5.2) can pass the cuts if there is a high energy particle which can fake the tag. This can either be provided by the ISR photon in radiative return events or, more usually, by a highly energetic particle within one of the hadronic jets, for example a meson which decays to photons. Unlike $\gamma^\star\gamma$ events they are produced isotropically, so the importance of this background is determined by the solid angle within which the tag is detected and the magnitude of the $\gamma^\star\gamma$ cross-section for a given sample. For both these reasons, this background is far more important in the EE sample than in either of the other two samples, and constitutes the dominant background in this sample. This background is largely reduced by the upper W_{vis} cut, because these events have a much larger invariant mass than $\gamma^\star\gamma$ events - if most of the final state is seen in the detector. For the EE sample, the E_{tag} cut is also important for reducing this background. In a $\gamma^\star\gamma$ event the tag is isolated from the rest of the event. This is not the case if there is a fake tag within a hadronic jet, and this is the reason for the electron isolation cut on the EE sample. In the region where tracking is available ($> \sim$275 mrad), one could potentially remove events where a photon fakes a tagged electron by requiring that there is a track pointing to the tag. However, when this possibility was investigated it was found that the tracking was neither sufficiently reliable, nor modelled well enough in the detector simulation.

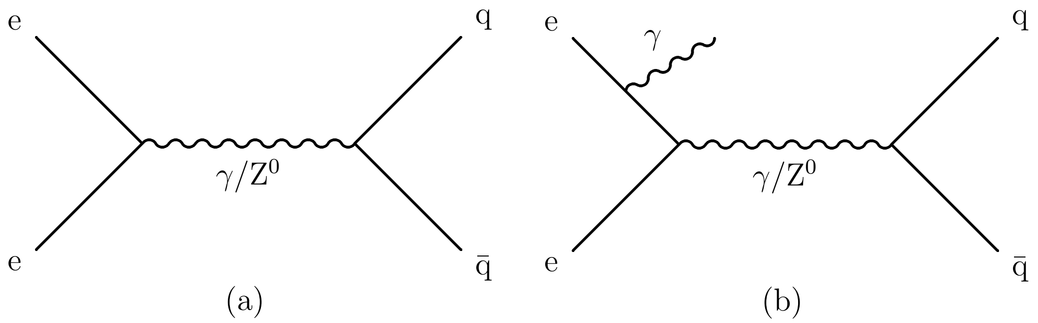

Figure 5.2: Diagrams for hadron production in e^+e^- annihilation: (a) non-radiative, (b) radiative return.

5.6.3 Tau pair production from e^+e^- annihilation

Annihilation events producing tau pairs have similar characteristics to the hadronic case discussed above, and can sometimes pass the multiplicity cut. However, the cross-section is much lower and their contribution is only significant in the EE sample.

5.6.4 Non-multiperipheral four-fermion events

There are processes besides the multiperipheral diagram of Figure 2.1 which give rise an $e^+e^-q\overline{q}$ final state. At LEP2, W^+W^- and Z^0 pairs can be produced, but the cross-sections are small so this background is negligible. Of more importance are the diagrams illustrated in Figure 5.3 - particularly the bremsstrahlung diagram, which has a non-negligible contribution at high Q^2, predominantly at low invariant masses of the photon-photon system.

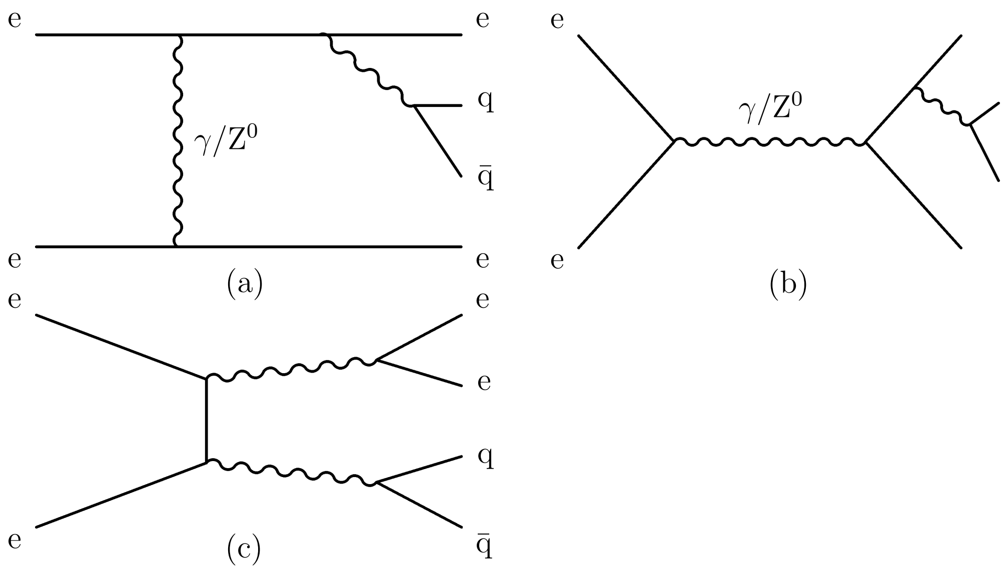

Figure 5.3: Non-multiperipheral four-fermion diagrams giving $e^+e^-q\overline{q}$ final states: (a) bremsstrahlung, (b) annihilation, (c) conversion. Unlabelled boson lines represent photons only; unlabelled fermion lines can be either electrons or quarks.

5.6.5 $\gamma^\star\gamma^\star$ interactions

Because the aim of this analysis is to measure the structure function of the quasi-real photon, hadronic events stemming from the interaction of two virtual photons ($\gamma^\star\gamma^\star$ events) are also treated as background. The cross-section falls off strongly with P^2, but cannot be neglected. If P^2 is sufficiently large ($> \sim 7$ GeV^2), then both of the scattered electrons can be seen in the detector. The anti-tag cut removes the majority of these events, but a low energy tail can remain. In addition, in the signal Monte Carlo P^2 is limited to be below 4.5 GeV^2. Thus it is necessary to subtract the events in the data in which the untagged electron, although not being seen in the detector, does not conform to this signal definition. The PHOJET generator was used to estimate this background for the SW and FD samples but, because PHOJET is not valid at high Q^2, the Vermaseren program was used instead for the EE sample.

5.6.6 Beam-gas events

Interactions between the beam electrons and residual gas molecules in the beam pipe can lead to the electron being deflected into the tagging detector. If this overlaps with, for example, an untagged two-photon event this can fake a signal event. Off-momentum electrons, as they are sometimes known, are concentrated at low polar angles and at energies well below the beam energy. They are not distributed symmetrically in ϕ - tending to occur predominantly in the plane of the accelerator. For some unknown reason this was always a more severe effect at OPAL than at the other three LEP experiments. Their effect can be seen at low values of E_{tag} in the E_{tag} versus ϕ_{tag} plot shown in Figure 5.4. This is the main consideration which determines how low the E_{tag} cut can go for the SW sample. This can be seen both from Figure 5.4 and the E_{tag} distribution shown later (Figure 6.1(a)), where there is a strong rise in the data distribution towards low tag energies, below the cut. For the

FD and EE samples, there is no evidence of off-momentum electrons in the E_{tag} distributions (Figures 6.4(a) and 6.7(a)).

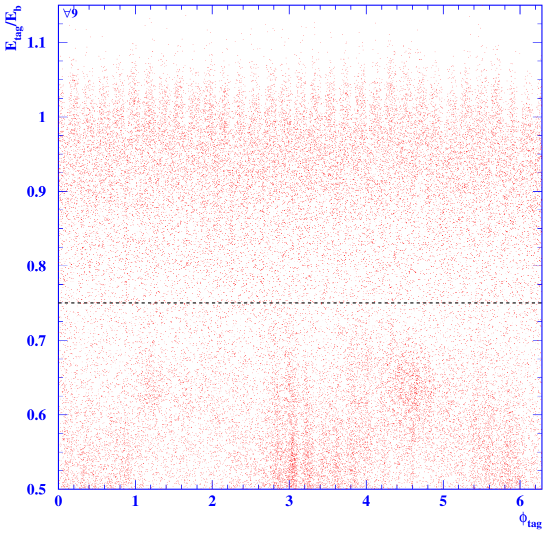

Figure 5.4: Energy versus azimuthal angle of the tagged electrons in the SW sample. The dashed line represents the cut on the tag energy.

5.7 Trigger Efficiency

Before comparing the data events with Monte Carlo or using them to extract cross-sections (i.e. measure F_2^γ), it is important to know whether signal events were efficiently triggered or whether a significant fraction went unrecorded by the OPAL detector. The trigger efficiency is estimated from the data by examining two statistically independent triggers (denoted A and B). For each event in the final samples there are three possibilities: both triggers A and B fire, only A fires or only B fires (assuming events in which neither trigger fires go unrecorded). The number of events in each of these classes can be denoted by N_{AB}, N_A and N_B respectively. The efficiency, ϵ_A, of trigger A is given by

$$\epsilon_A = \frac{N_{AB}}{N_{AB} + N_B}, \tag{5.2}$$

and similarly for ϵ_B. The total trigger efficiency is then estimated to be

$$\epsilon_{TOT} = \epsilon_A + \epsilon_B - \epsilon_A \epsilon_B. \tag{5.3}$$

The two-photon events studied in this analysis can potentially be triggered by both the tagged electron and by the hadronic final state. In general, one looks for separate, independent triggers relating to these two aspects of the events in order to calculate the efficiency as described above. The estimation of the efficiency for each of the data samples is detailed in the following. The trigger signals relevant to this analysis were given in Table 3.1.

5.7.1 Trigger efficiency for the EE sample

The stand-alone EE triggers EELHI and EERHI have a very low threshold (2.4 GeV) relative to the minimum possible tag energy of 64.05 GeV. It is therefore unsurprising that one of these triggers fires for every event in the EE sample. This means that any estimation of the trigger efficiency, using these triggers, via the method described above will result in a value of 100%. This value can be regarded as reliable, so long as there is sufficient coverage of independent triggers, so some checks of the coverage have been made. Independent triggers are provided by the CT, EB and TB triggers. The triggers TPTTTOB.TBEBS and TBM1.EB1 give high efficiencies of 93.8% and 93.0% respectively, lending confidence to the assumption of 100% trigger efficiency for this sample.

5.7.2 Trigger efficiency for the FD sample

For the FD sample, the FDHIOR trigger provides an independent trigger for the tagged electron and is used as trigger A in Equations 5.2 and 5.3. Trigger B is made up of the logical OR of the following triggers:

TPTTEM
TBM3
TPTTTOB.TBEBS
TPTOEMB.EBWEDGE
EBTOTLO.(EELLO+EERLO)

The trigger efficiency for the events in the FD sample is calculated, using Equation 5.3, to be 99.999%.

5.7.3 Trigger efficiency for the SW sample

The calculation of the trigger efficiency for the SW sample is complicated by the fact that there was no independent trigger for the tagged electron - a coincidence being required with the CT or ECAL triggers. In this case, it is necessary to employ a modified version of the above method. A third trigger, C, is used to define a subset of N_C events within the total sample. Within this subset the classes of events for triggers A and B are as before, with an additional class for the case where neither fires. This subset is used to check the correlation of triggers A and B, which, if small, permits the use of Equation 5.3 to give a lower estimate for the total trigger efficiency. It is a lower estimate because it does not include the effect of trigger C on the total efficiency.

The correlation of triggers A and B for the subset N_C events is

$$\mathrm{Corr}_{AB} = \frac{\epsilon_{AB} - \epsilon_A \epsilon_B}{\sigma_A \sigma_B} \tag{5.4}$$

where the efficiencies are now given by

$$\epsilon_A = \frac{N_{AB} + N_A}{N_C}, \qquad \epsilon_B = \frac{N_{AB} + N_B}{N_C}, \qquad \epsilon_{AB} = \frac{N_{AB}}{N_C}, \tag{5.5}$$

and the standard deviations are

$$\sigma_A = \epsilon_A(1 - \epsilon_A), \qquad \sigma_B = \epsilon_B(1 - \epsilon_B). \tag{5.6}$$

The triggers used to estimate the efficiency for the SW sample are:

- **Trigger A**, logical OR of:
  SWHIOR.(TPEML+TPEMR)
  SWHIOR.TBM1
  TPTTTOB.TBEBS
  (TPEML.TPTTR)+(TPEMR.TPTTL)
- **Trigger B**, logical OR of:
  (TPTOB+TPTT1).(EELLO+EELLR+EBTOTLO)
  TPTOEMB.EBWEDGE
- **Trigger C:**
  TPTTEM

This method yields a lower limit on the trigger efficiency for the SW sample of 99.9%, with the correlation between triggers A and B being -10.1.

Chapter 6

Comparison of Data with Monte Carlo

The importance of a good description of the data by the Monte Carlo simulations was emphasised in Chapter 4. In this chapter, plots comparing the selected data with the predictions of the signal and background Monte Carlo programs are presented and discussed. The Monte Carlo samples are normalised to the integrated luminosity of the data, and samples generated at different centre-of-mass energies are mixed in the same proportions as the data. The exception is the PHOJET 1.05 signal samples, which are normalised such that the predicted number of events at each $\sqrt{s}$ for the SW sample is the same as that of HERWIG. Thus the PHOJET distributions only allow for a shape comparison. The SW samples were chosen for the normalisation because they cover the Q^2 region for which PHOJET is supposed to be valid. In fact, if the FD samples had been used instead the difference would have been minimal. The PHOJET distributions are shown without the reweighting referred to in Section 4.2.

The numbers of signal events (selected events minus background) in the data are given in Table 6.1 for the three samples. Also given are the numbers

	SW	FD	EE
Data signal	26071 ± 167	10652 ± 110	274 ± 21
HERWIG signal	26560 ± 49	9989 ± 30	296 ± 5
Vermaseren signal	-	-	251 ± 4

Table 6.1: The numbers of signal events (selected events corrected for background) in the data compared to the signal predictions from the HERWIG and Vermaseren programs. The errors given are statistical only.

predicted by HERWIG and, for the EE sample, the Vermaseren program. It can be seen that HERWIG predicts slightly more events than are seen in the data for the SW sample and slightly fewer for the FD sample, whilst the numbers for the EE sample agree within statistics. The Vermaseren number for the EE sample is, in contrast with HERWIG, lower than the data, but, again, given the statistics the difference is not significant. The detailed comparison of each sample with the Monte Carlo prediction is discussed in the following three sections.

6.1 SW Sample

The analysis of the SW sample up to this point is very similar to that performed for the most recent previous OPAL analysis of F_2^γ [13, 92], but includes three times the data integrated luminosity. The quality of the description of the data by the Monte Carlo is similar to that presented there.

Figure 6.1 shows variables relating to the tagged electron for the SW sample. The data are compared to the sum of the major background sources and the signal Monte Carlo - either HERWIG or PHOJET. The major backgrounds are also shown separately at the bottom of the plots, although in this case the tau pair background dominates and is the only one visible. It can be seen that, in general, the data are well described by the Monte Carlo models within the selection cuts (which are shown as dashed lines). There is not much to choose between the two models, although HERWIG clearly follows the shape of the data better in the θ_{tag} distribution (b). This plot shows that the cuts on the polar angle are set to include the maximum possible range, since beyond them the data and Monte Carlos are strongly discrepant. This is particularly the case at low polar angles, and here the difference is because of the radiation shielding introduced before the LEP2 programme began, to shield the detector from synchrotron radiation.

The presence of off-momentum electrons is clear at low tag energies, below the cut, in the $E_{\mathrm{tag}}/E_{\mathrm{b}}$ plot (a), with the strong rise of the data above the sum of signal and background Monte Carlos. The ϕ_{tag} distribution (c) is consistent with the expected flat distribution, although the scatter in the data is a perhaps a little large. The fourth variable shown is Q^2 (d) - important because it is used to determine x (Equation 2.7).

Variables related to the hadronic final state are shown in Figure 6.2. For these distributions there are significant differences between HERWIG and PHOJET, with HERWIG generally doing the better job. The strongest differences are seen in the $E_{\mathrm{T,out}}$ distribution (d). $E_{\mathrm{T,out}}$ is the transverse hadronic energy out of the plane containing the beam line and the tagged electron:

$$E_{\mathrm{T,out}} = \sum_i E_{i,\mathrm{t}} |\sin\phi_i| \tag{6.1}$$

where i runs over all particles in the hadronic final state, with transverse energy $E_{i,\mathrm{t}}$. The azimuthal angle ϕ_i is measured from the tagged electron. This variable has been found [92] to be particularly sensitive to the angular distribution of hadrons in the final state. The shape is described better by HERWIG, but it still falls short at high values of $E_{\mathrm{T,out}}$.

HERWIG is also closer to the data in the N_{trk} (a) and W_{vis} (c) distributions, although it does lie above the data at middling values of W_{vis}. Although it is partly disguised by the logarithmic scale, PHOJET produces far too few events at low W_{vis}, where it only generates soft events.

The effectiveness of the cut on $N_{\mathrm{trk}} - N_{\mathrm{e}}$ (the number of tracks **not** identified as electrons) is demonstrated in (b), with a large excess of the data over the simulations below the cut. This excess is most likely due to unshown background $\gamma^\star\gamma \rightarrow \mathrm{e^+e^-}$ or Bhabha events with extra tracks due to, for example, photon conversions.

The measured x distribution, x_{vis}, calculated from Q^2 and W_{vis}, is shown in Figure 6.3. At values of x_{vis} greater than 0.1, which is the region considered in this thesis, the HERWIG model using the GRV parameterisation of F_2^γ qualitatively follows the data, which means that the F_2^γ found from the data should be similar to the expectation from GRV. Because of the shortcoming of the PHOJET model already discussed, the description of the x_{vis} distribution is unsatisfactory when using the PHOJET model without reweighting of the x distribution.

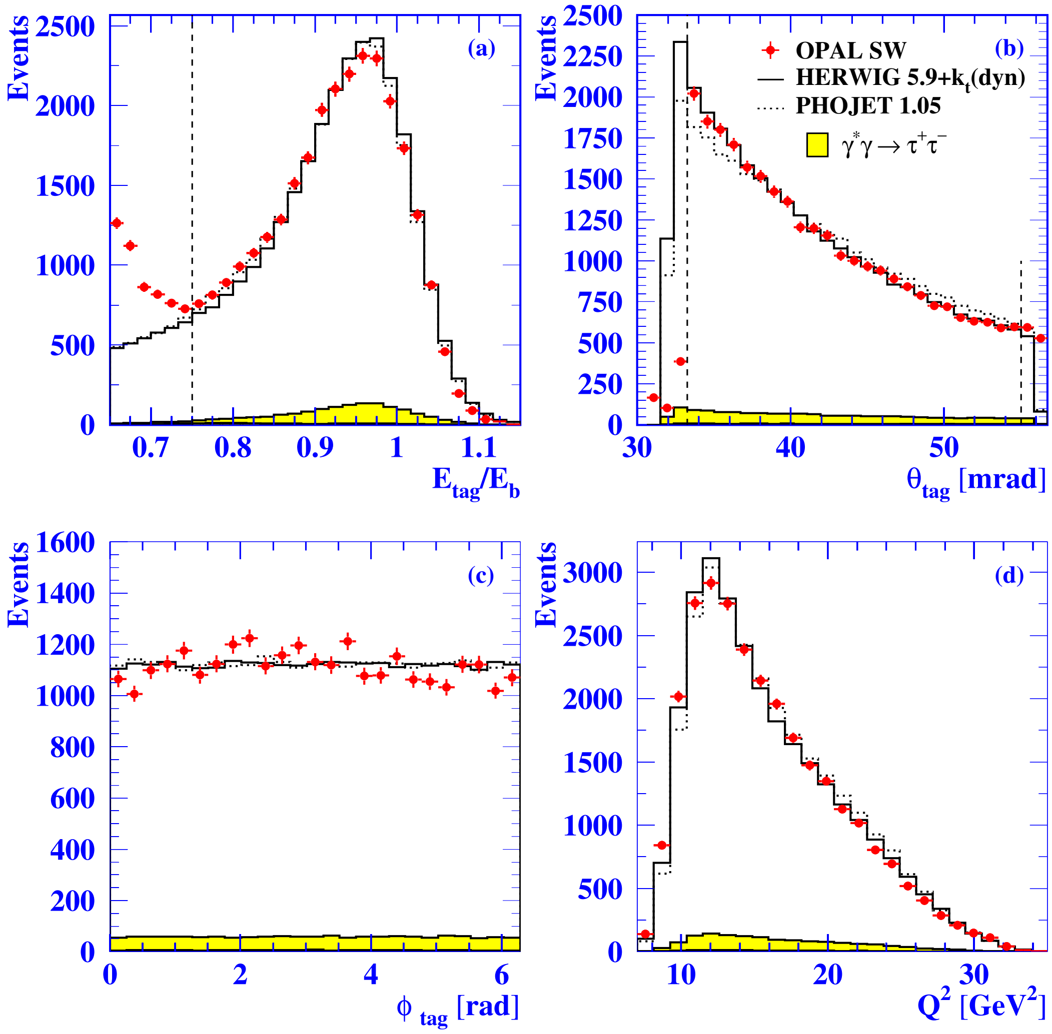

Figure 6.1: Data and Monte Carlo distributions of variables related to the tagged election for the SW sample. The open histograms are the sum of the signal prediction and the contributions of the major background sources (shaded histograms), shown both for the HERWIG and PHOJET models. The Monte Carlo predictions are normalised to the data luminosity, except for PHOJET where the sample has been normalised such that the predicted number of events for the SW sample is the same as that of HERWIG. All selection cuts have been applied, except for any cut on the variable in the plot (indicated as dashed lines if within the region shown). The distributions shown are: (a) $E_{\rm tag}/E_{\rm b}$, the energy of the tagged electron as a fraction of the beam energy; (b) $\theta_{\rm tag}$, the polar angle of the tagged electron; (c) $\phi_{\rm tag}$, the azimuthal angle of the tagged electron; (d) the measured Q^2. The errors are statistical only.

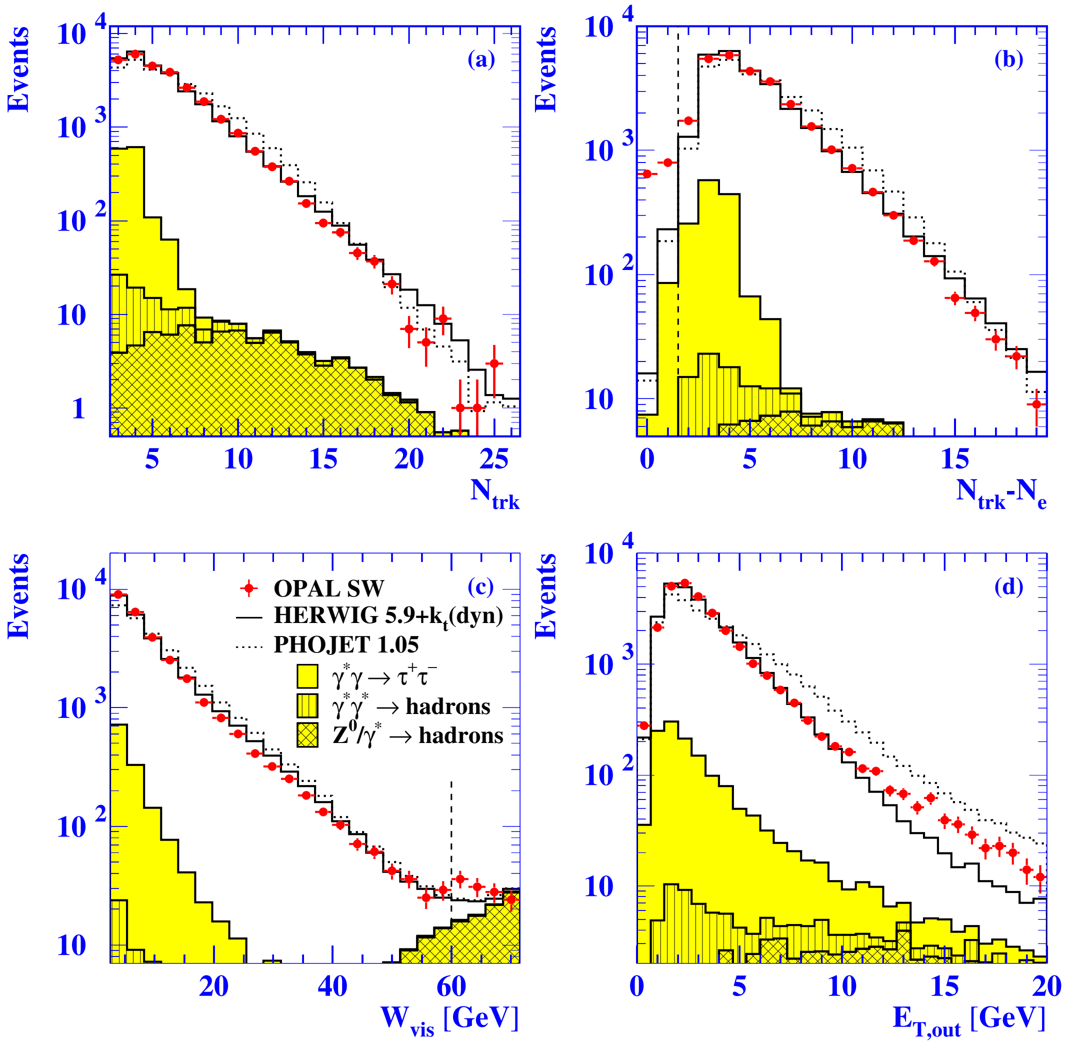

Figure 6.2: Data and Monte Carlo distributions of variables related to the hadronic final state for the SW sample. The distributions shown are: (a) N_{trk}, the track multiplicity; (b) $N_{\mathrm{trk}} - N_{\mathrm{e}}$, the number of tracks not identified as electrons; (c) W_{vis}, the measured invariant mass of the hadronic final state; (d) $E_{\mathrm{T,out}}$, the transverse component of energy out of the tag plane. See Figure 6.1 caption for further details.

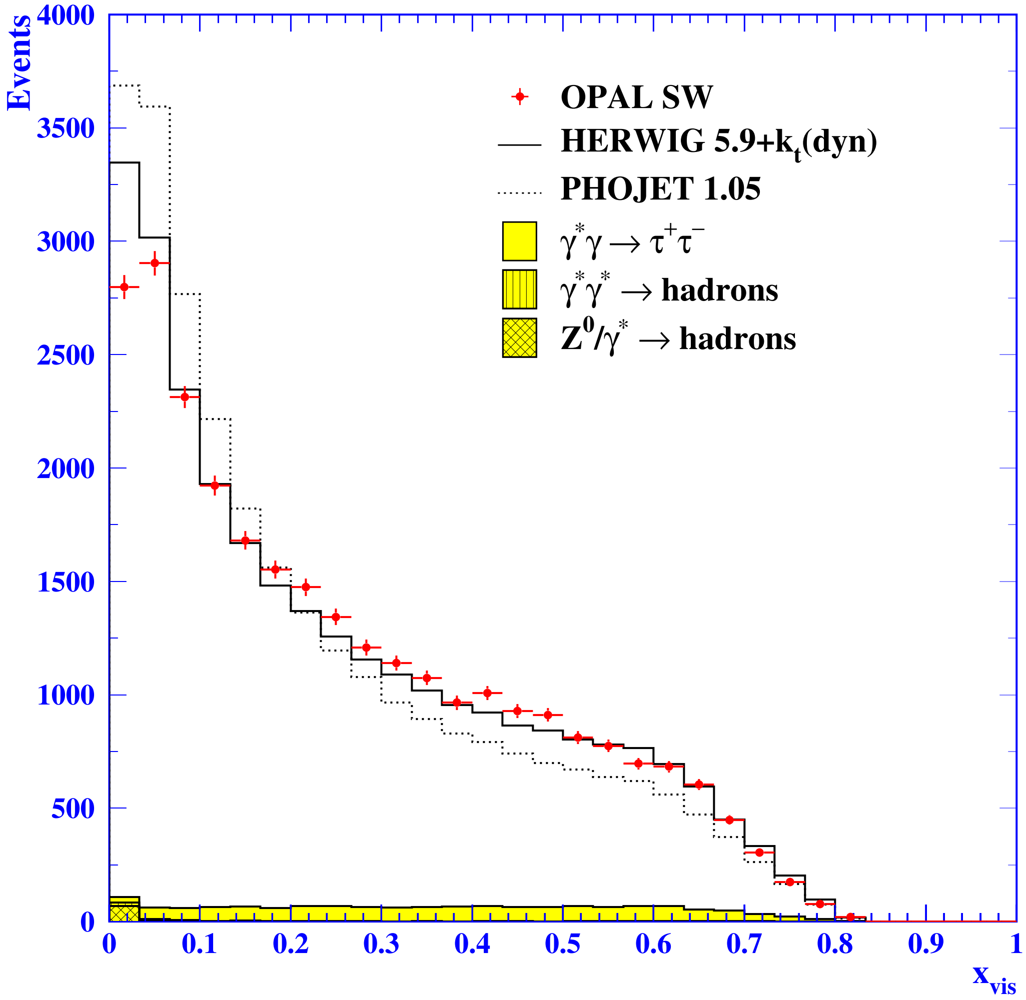

Figure 6.3: The measured $x_{\rm vis}$ distribution for the SW sample. See Figure 6.1 caption for further details.

6.2 FD Sample

The same distributions as were presented for the SW sample are shown in Figures 6.4, 6.5 and 6.6. Broadly speaking, the distributions have the same general form as those for the SW sample, but with lower statistics. The background from $\gamma^{\star}\gamma \to \tau^{+}\tau^{-}$ still dominates, but now other backgrounds make a larger relative contribution.

For the variables relating to the tag, Figure 6.4, it can be seen that the description of the data by both Monte Carlos is generally good. In this case, PHOJET follow the shape of the data better, certainly for the $\theta_{\rm tag}$ (b) and Q^2 (d) distributions, and also at low tag energies in (a). The energy of the tag cluster in the Monte Carlo has been corrected following a study of Bhabha scattering events where the electrons were detected in the FD; see Appendix A for details. There is clear structure in the $\phi_{\rm tag}$ distribution (c), where the two dips are due to the gap between the two half-cylinders of which each FD main calorimeter was composed.

Turning to the distributions for the hadronic final state, Figure 6.5, one sees that HERWIG, although not being perfect, is far closer to the data. PHOJET has the wrong shape, with only about half the events of the data at low multiplicity/mass and far too many at higher values. This is particularly the case in the $E_{\rm T,out}$ distribution (d). These deficiencies are reflected in the difference between the data and PHOJET in the $x_{\rm vis}$ distribution, Figure 6.6. Note that the virtuality of the tagged electron in this sample is at larger values than those for which the author recommends PHOJET be used, but recall also that PHOJET will in the end only be used for estimating the systematic uncertainty on the final result. The HERWIG description of the $x_{\rm vis}$ distribution is far better, but is systematically lower than the data for $0.1 < x_{\rm vis} < 0.7$.

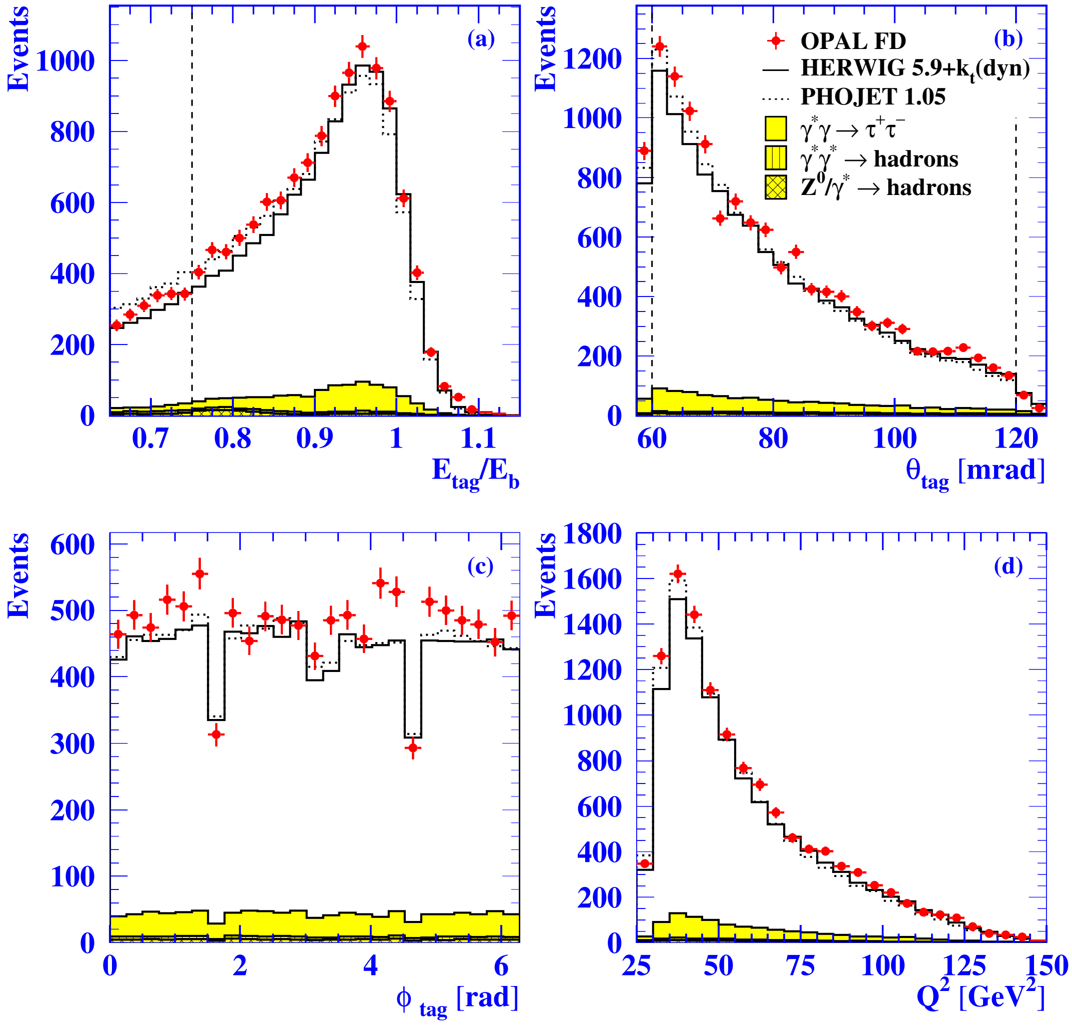

Figure 6.4: Data and Monte Carlo distributions of variables related to the tagged election for the FD sample. The distributions shown are: (a) $E_{\rm tag}/E_{\rm b}$, the energy of the tagged electron as a fraction of the beam energy; (b) $\theta_{\rm tag}$, the polar angle of the tagged electron; (c) $\phi_{\rm tag}$, the azimuthal angle of the tagged electron; (d) the measured Q^2. See Figure 6.1 caption for further details.

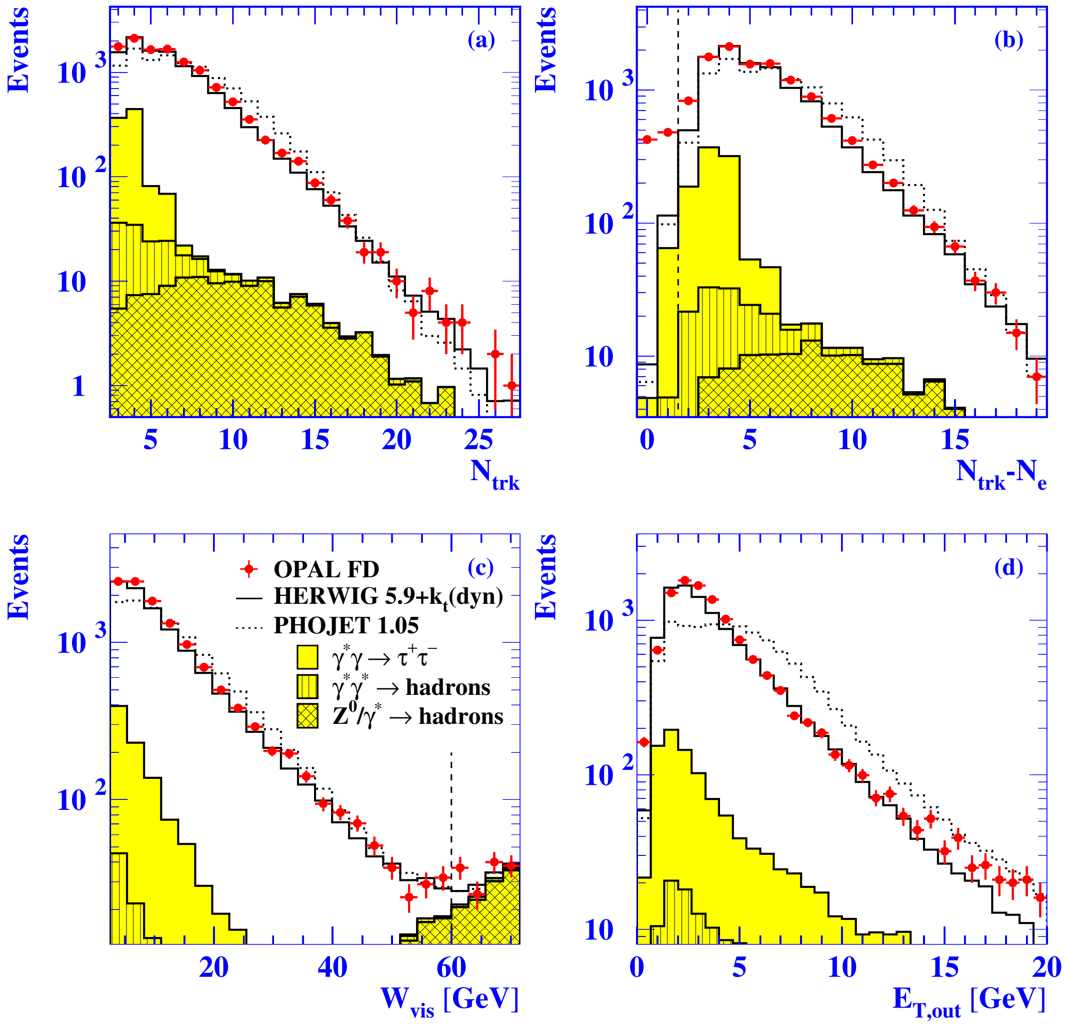

Figure 6.5: Data and Monte Carlo distributions of variables related to the hadronic final state for the FD sample. The distributions shown are: (a) N_{trk}, the track multiplicity; (b) $N_{\text{trk}} - N_{\text{e}}$, the number of tracks not identified as electrons; (c) W_{vis}, the measured invariant mass of the hadronic final state; (d) $E_{\text{T,out}}$, the transverse component of energy out of the tag plane. See Figure 6.1 caption for further details.

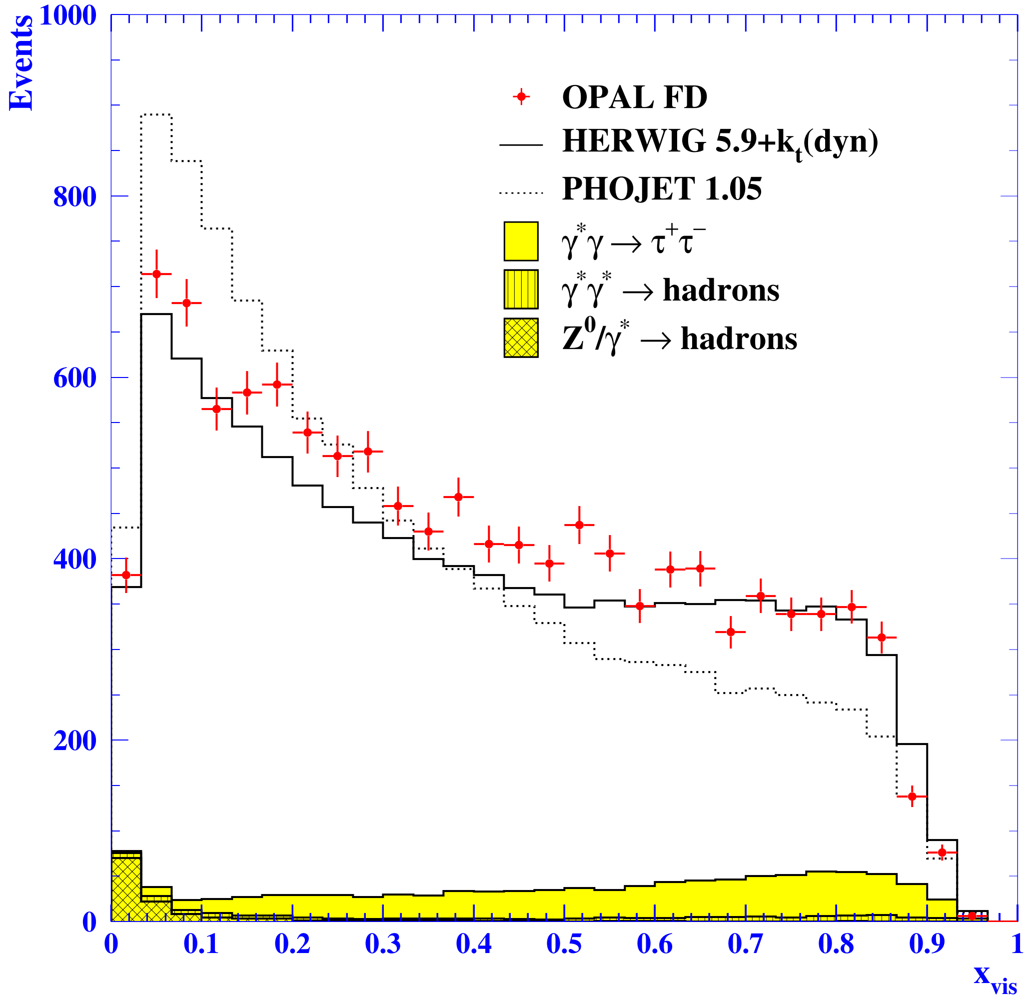

Figure 6.6: The measured x_{vis} distribution for the FD sample. See Figure 6.1 caption for further details.

6.3 EE Sample

For the EE sample we are in a very different regime, with low data statistics and different - and much larger - background contributions. The variables related to the tagged electron, Figure 6.7, are, within statistics, well described by both the HERWIG and Vermaseren models. As in the case of the FD sample, the tag energy has been corrected through a study of Bhabha events (see Appendix A).

For the hadronic final state variables, Figure 6.8, there are apparent differences in shape, with both Monte Carlos having a significant excess over the data at low N_{trk}(a), W_{vis}(c) and $E_{\mathrm{T,out}}$(d). At higher values, HERWIG follows the data well, but Vermaseren tends to be deficient. In the region of high W_{vis}, above the cut where the background completely dominates, the Monte Carlo follows the data well, lending confidence to the modelling of the annihilation background in this sample. For this sample, the $N_{\mathrm{trk}} - N_{\mathrm{e}}$ cut has only a small effect because of the tighter multiplicity cut. Therefore, this distribution has been replaced in Figure 6.8(b) by a plot of the energy in a cone of 500 mrad about the tagged electron. It can be seen that the data removed by the cut (the electron isolation cut) is almost entirely background (see Section 5.6.2), and that the region around and above the cut is well modelled by the Monte Carlo.

The x_{vis} distribution is shown in Figure 6.9. The difference in shape of the W_{vis} distribution is reflected in the observed difference between the data and both Monte Carlo models for this distribution. The Vermaseren program under-populates the lower x region, which is as expected for this purely point-like model.

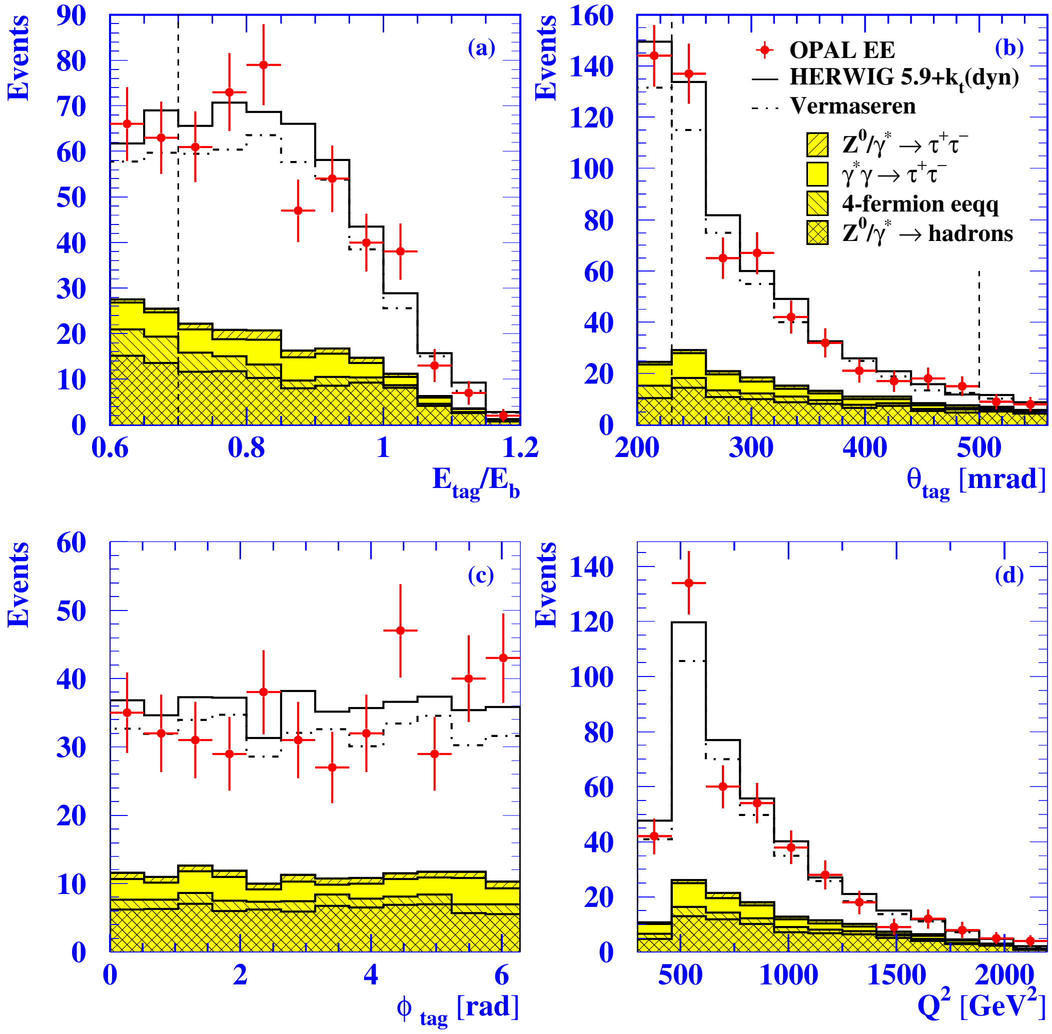

Figure 6.7: Data and Monte Carlo distributions of variables related to the tagged election for the EE sample. The open histograms are the sum of the signal prediction and the contributions of the major background sources (shaded histograms), shown both for the HERWIG and Vermaseren models. The Monte Carlo predictions are normalised to the data luminosity and all selection cuts have been applied, except for any cut on the variable in the plot (indicated as dashed lines if within the region shown). The distributions shown are: (a) $E_{\rm tag}/E_{\rm b}$, the energy of the tagged electron as a fraction of the beam energy; (b) $\theta_{\rm tag}$, the polar angle of the tagged electron; (c) $\phi_{\rm tag}$, the azimuthal angle of the tagged electron; (d) the measured Q^2. The errors are statistical only.

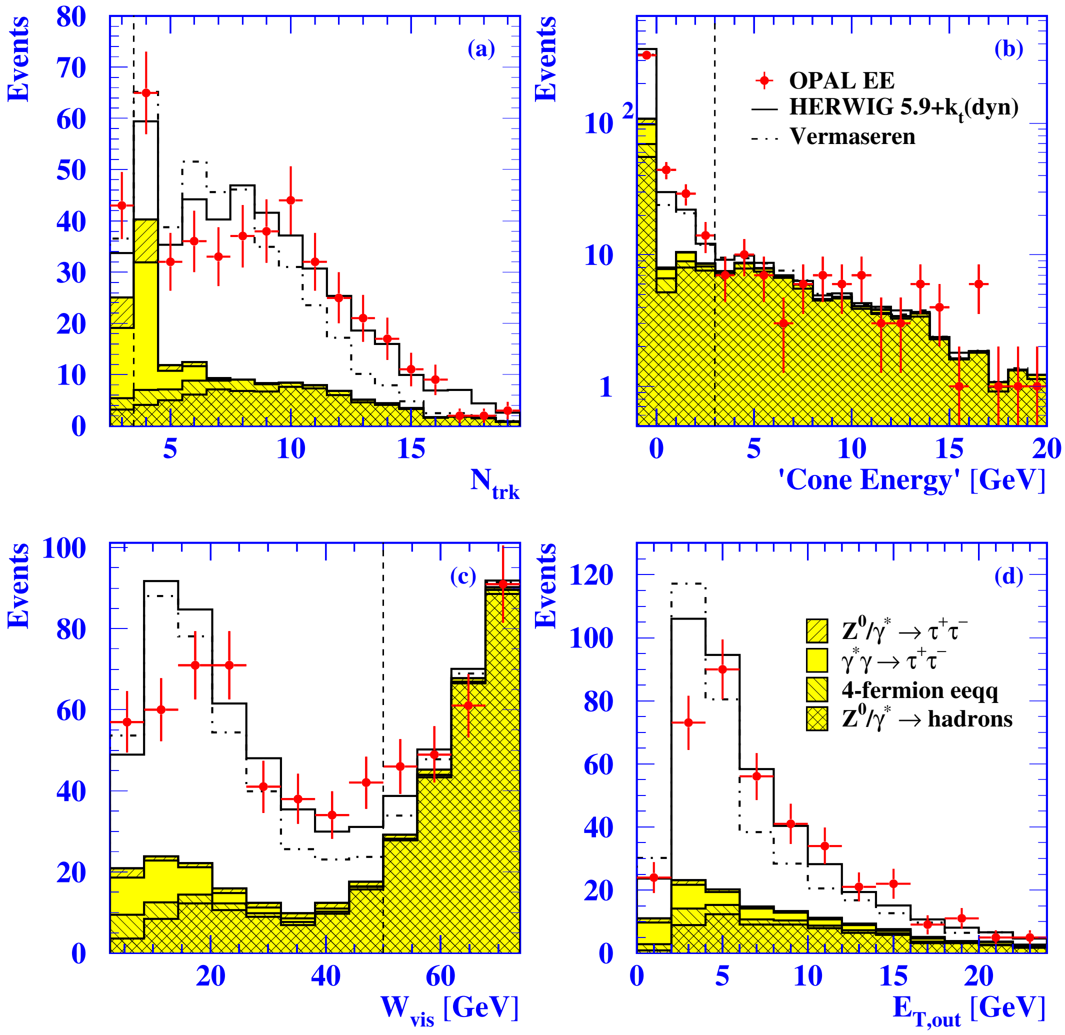

Figure 6.8: Data and Monte Carlo distributions of variables related to the hadronic final state for the EE sample. The distributions shown are: (a) $N_{\rm trk}$, the track multiplicity; (b) the energy deposited in a cone of radius 500 mrad about the tag (note that the left-hand bin corresponds to zero energy); (c) $W_{\rm vis}$, the measured invariant mass of the hadronic final state; (d) $E_{\rm T,out}$, the transverse component of energy out of the tag plane. See Figure 6.7 caption for further details.

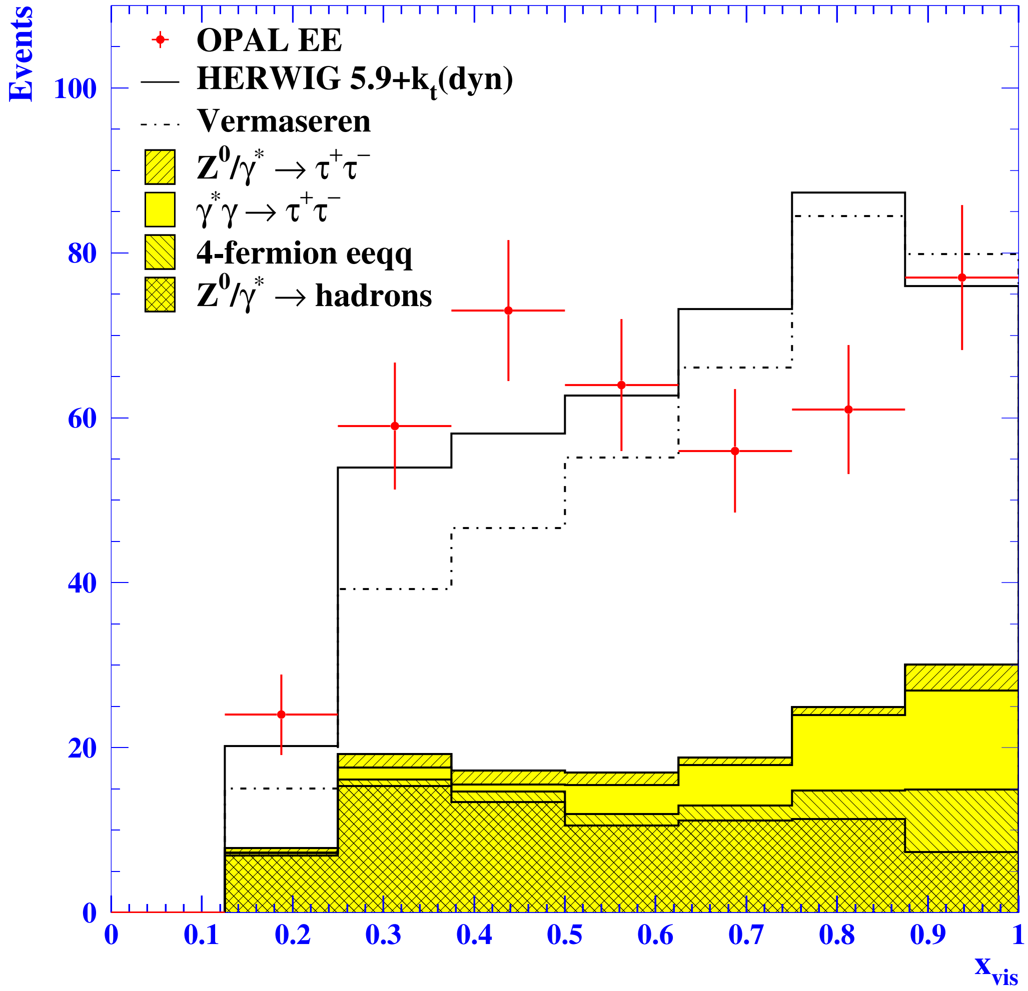

Figure 6.9: The measured $x_{\rm vis}$ distribution for the EE sample. See Figure 6.7 caption for further details.

Chapter 7

The Measurements of F_2^γ

In this chapter, the complete results obtained in this analysis are presented, accompanied by a full description of the corrections applied to the result, and of the determination of the systematic error. The results are given in two parts: first, the measurement of F_2^γ as a function of x at high Q^2 using the EE sample, and second, the measurement of the Q^2 evolution of F_2^γ using all three samples. Before that, however, is a discussion of unfolding: the major tool used to obtain the results given the selected dataset.

7.1 Unfolding

With an ideal detector one could measure F_2^γ simply by binning events in x and Q^2 and counting them. In reality, however, the measured distribution differs from the underlying true distribution that one is trying to measure because of a number of effects: the detector has limited acceptance, so some events may not be observed at all; the resolution is not perfect, so the value of x is smeared; and some background events remain in the final sample.

The most serious of these problems is the limited resolution, and in particular the migration of events from one region of x to another. To calculate x, the measured values of Q^2 and W are needed (Equation 2.7). Q^2 can be measured to an accuracy of a few percent, with a basically Gaussian error, but $W_{\rm vis}$ is in general strongly distorted with respect to the true value because particles are lost down the beam pipe or poorly measured in the forward calorimeters. This means that $W_{\rm vis}$ is usually less - sometimes much less - than the true invariant mass. This leads to a migration of events from low to higher x.

A common method used to correct for such effects is a bin-by-bin procedure, where a correction factor for each bin is deduced by comparing the ratio of the number of events in the bin at the generator and detector levels. It has become generally accepted that this is not a suitable method for analyses of this type because of the large migrations from low to high W. Nevertheless, at an early stage of the present analysis an investigation was conducted into whether the efficiencies, purities and correction factors (according to Monte Carlo) for the EE sample would permit the use of a bin-by-bin correction method. Purities and efficiencies were found to be of order 60%, with correction factors of up to 40%. It was decided that, given these values, bin-by-bin corrections would not adequately account for migration effects.

The method therefore used to correct for efficiency, resolution and migration is unfolding. The background in the sample is assumed to be known through Monte Carlo simulation and is subtracted from the measured distribution. Unfolding is by now a well-established and thoroughly tested technique in measurements of F_2^γ. It is discussed below, first generally, and then in terms of its specific application to this analysis.

7.1.1 The unfolding problem

Mathematically, the relation between the true distribution, $f(x)$, and the measured one (with background subtracted), $g(x_{\rm vis})$, can be expressed as the convolution integral

$$g(x_{\rm vis}) = \int A(x_{\rm vis}, x)\, f(x)\, {\rm d}x + e(x_{\rm vis})\,, \tag{7.1}$$

where $e(x_{\rm vis})$ represents statistical errors on the measured distribution and $A(x_{\rm vis}, x)$ is the response function which characterises the behaviour of the detector. It takes into account both resolution/migration, through which the true value of x is transformed into a measured value $x_{\rm vis}$, and acceptance/efficiency, such that some events are lost altogether, for example if they fail the experimental cuts.

Of course, we don't measure a continuous distribution, but rather a histogram of events, so Equation 7.1 needs to be discretised, leading to the matrix equation:

$$g = Af + e\,, \tag{7.2}$$

where g, f and e represent histograms and A is the response, or transformation, matrix. It's elements A_{ij} can be interpreted as the probability of an event in bin j of the true distribution being found in bin i of the measured one. If A is known, the simplest way to compare a theoretical prediction for f with the data is to fold the theoretically predicted true distribution with the response matrix, and compare the then folded theoretical spectrum with the measured one. This method is simple and stable, but makes it very hard to later compare a published measurement with alternative theoretical predictions (since the response matrix is needed), and impossible to make a comparison between different experiments.

It is therefore much more desirable to find a way to solve Equation 7.2 and find the underlying true distribution of the measurement. If the inverse of A exists, the naive assumption would be that one could solve the equation and find the true distribution thus (ignoring the statistical errors on the measurement):

$$f = A^{-1}g. \tag{7.3}$$

Unfortunately, this does not in general lead to a stable solution, but rather one that is wildly oscillating. The problem is that the errors e cannot be neglected, even if they are small compared to g. An intuitive understanding of why this happens can be reached by considering the nature of the matrix A. Usually, it is a smoothing matrix, which removes high frequency components in f. If this is the case, A^{-1} should put them back; but after smearing these components are a small effect, and are overwhelmed by the statistical errors. Thus the inverse response matrix puts back a completely different set of high frequency components to those in the original distribution, making the result useless.

The presence of the statistical errors, coupled with the fact that A is usually not known analytically, but rather obtained from a Monte Carlo simulation of the detector response, makes unfolding a statistical rather than an analytical problem. The way of reducing high frequency oscillations is to introduce a bias towards a smooth solution, and this leads to the method of regularised unfolding. The specific implementation which is used in this analysis is described in the next section.

7.1.2 The RUN program

The RUN program [93] implements an algorithm for regularised unfolding based on the well-known maximum likelihood method, described, for example, in Reference [94]. It uses this to perform a fit of the expression $g = Af$ to the data distribution. The response function A is implicitly given by the set of input Monte Carlo events with full detector simulation. (See [93] for details of how this is done numerically using the discrete distributions.) The solution, $f_u(x)$, would exhibit the same oscillating behaviour as in the case of matrix inversion if no smoothing were applied. The regularisation is introduced by the addition of a term to the negative log likelihood function, $S(f_u)$, which becomes:

$$S'(f_u) = S(f_u) + \tau \int [f_u''(x)]^2 \, \mathrm{d}x \tag{7.4}$$

The integral represents the total curvature, which would be large in the case of a strongly fluctuating solution. The factor τ is the regularisation parameter, which controls the amount of smoothing; the larger its value the stronger is the bias towards a smooth solution. Its magnitude can be defined such that the bias is small compared to the statistical errors; in effect, the regularisation provides a smooth cut-off of higher order terms in the solution.

$f_u(x)$ is a continuous function which is parameterised by B-splines. The final unfolding result is obtained by multiplying the input true distribution in the Monte Carlo by $f_u(x)$. An alternative way of looking at $f_u(x)$ is therefore as a weight function, which can be used to calculate an individual weight factor for each Monte Carlo event, depending on its true x value. The reweighted Monte Carlo events agree with the x_{vis} distribution of the data, within statistics. Results in bins of x can be obtained by integration over ranges of the final function.

RUN implements the full error propagation, taking into account the data statistics, the properties of the response function and the bias introduced by the regularisation. The statistical error on the response matrix is neglected, however, so it is important to have much more Monte Carlo than data (in this analysis there is always at least 10 times more Monte Carlo integrated luminosity than in the data). The propagation leads to correlated errors, and it should be noted that the variances will be much larger than would naively be expected given the statistics of the measurement. The limited resolution places a restriction on the number of data points that can be reconstructed from the data. If the bins are too narrow, then the results will have large correlations. RUN includes an algorithm which determines the optimal number of bins and their widths, given the aim of small correlations between the bins.

The form of the input distribution in the Monte Carlo should not affect the result. This does not, however, mean that the result is independent of the input Monte Carlo model used, since different models, with differences in such areas as the distribution of hadrons in the final state, can lead to differences in the calculated response matrix. It is this that has led to large systematic errors in past measurements of F_2^γ, and is why it is important to have models that give the best possible description of the data distributions.

7.1.3 Obtaining F_2^γ and $\mathrm{d}\sigma/\mathrm{d}x$

The unfolding procedure recovers the 'true' x distribution of the data, but what we are trying to make a measurement of is F_2^γ. Fortunately, the underlying F_2^γ that was used to generate the Monte Carlo events is known, and so to obtain the final result the unfolded function f_u is multiplied by the input F_2^γ (rather than the input true x distribution of the Monte Carlo events). The data cover a range of Q^2, and so the input $F_2^\gamma(x, Q^2)$ is calculated at the average value of Q^2, $\langle Q^2 \rangle$, of the data. Thus the data are unfolded to that specific value of Q^2. A slightly special treatment is required in the case of PHOJET. As stated in Section 4.2, PHOJET does not generate its events according the input structure function, and is therefore reweighted to match the HERWIG x distribution in order that the F_2^γ used as input to HERWIG can be used to find the result for F_2^γ. Technically, this is achieved for each unfolding by fitting a polynomial to the ratio of the PHOJET and HERWIG true x distributions.

In this analysis, results are given not only for F_2^γ but also in terms of the differential cross-section, $\mathrm{d}\sigma/\mathrm{d}x$. These are not given at a specific value of Q^2, but rather for the phase space defined by a Q^2 range. This means that explicit Q^2 cuts need to be applied, rather than the implicit ones given by the E_{tag} and θ_{tag} cuts, in order to have a well-defined phase space and avoid extrapolating the quoted result into areas where the efficiency is very low. Figure 7.1 shows the selection efficiency, according to HERWIG, for each sample as a function of Q^2. The efficiencies are obtained by dividing the histograms of the events passing the cuts by those for all generated events. The Q^2 cuts were chosen to be approximately at the points where the efficiency falls below

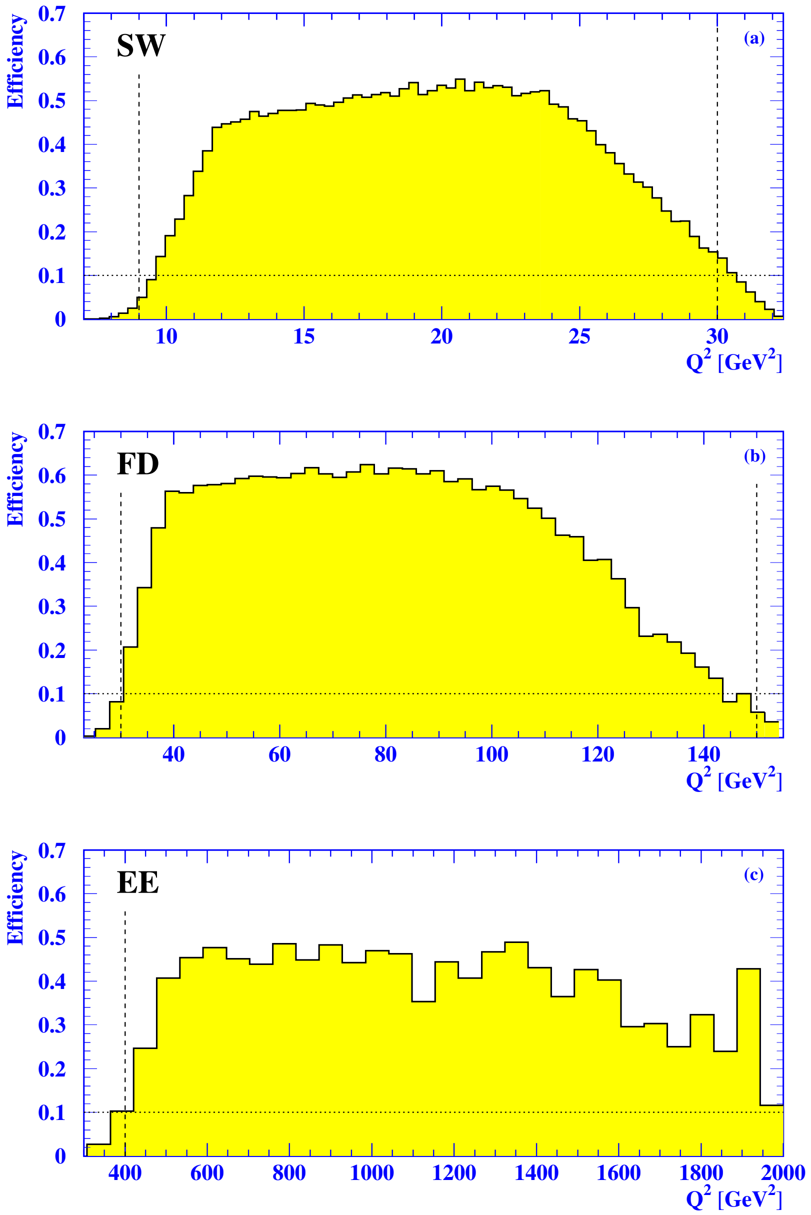

Figure 7.1: The selection efficiency as a function of Q^2 for (a) the SW, (b) the FD and (c) the EE samples, according to HERWIG 5.9+k_{t}(dyn). The efficiency is obtained by dividing the histogram of the events passing the cuts by that containing all generated events. The horizontal dotted line on each plot indicates 10% efficiency. Cuts on Q^2 were applied to the data at the values indicated by the dashed lines.

10%. These additional cuts on Q^2 are applied to all samples, both data and Monte Carlo, before the unfolding was performed, for both the F_2^γ and $\mathrm{d}\sigma/\mathrm{d}x$ measurements. The result for $\mathrm{d}\sigma/\mathrm{d}x$ is obtained by fitting a polynomial to the true x distribution of the events in the entire Monte Carlo sample, after the cuts on Q^2 and also one on y (again to avoid an extrapolation into a region where no measurement is made) have been applied. The unfolded function f_u is then multiplied by this polynomial rather than the input structure function. The quoted result applies to the phase space defined by the Q^2 range and the y cut ($y < 0.3$), and also by the P^2 cut applied to the generated samples. The W cut in the generated samples is in all cases outside the range of x for which a result is quoted.

The OPAL analysis immediately prior to this one [13, 92] used unfolding in two dimensions (i.e. another variable in addition to x) in order to reduce the dependence of the result on the input Monte Carlo model. The present analysis, however, reverts to unfolding in only one dimension, for a number of reasons. First is a practical reason: in order to compare with previous measurements of the evolution of F_2^γ with Q^2, it is desirable to present the results in specific x bins, of sometimes unequal width. The analysis of References [13, 92] used the unfolding package GURU [95], which unlike RUN can be adapted to perform unfolding in two dimensions. GURU, however, requires equispaced bins in order to perform the regularisation, whereas because the output of RUN is a smooth function, any binning can be chosen for the final result. In addition, GURU requires that the full range of the unfolding variable be included when unfolding [96], whereas in this analysis we do not want to include the low-x region in the final results. It has been demonstrated [13, 92] that RUN and GURU give consistent results.

The physics justification for the return to one dimensional unfolding is as follows: the problem of the dependence on the input Monte Carlo is most severe at low values of x, i.e. high W. The previous OPAL analysis [13, 92] was dedicated to measuring the low-x behaviour of F_2^γ. In the present analysis, no attempt is made to access values of x lower than 0.1. For the

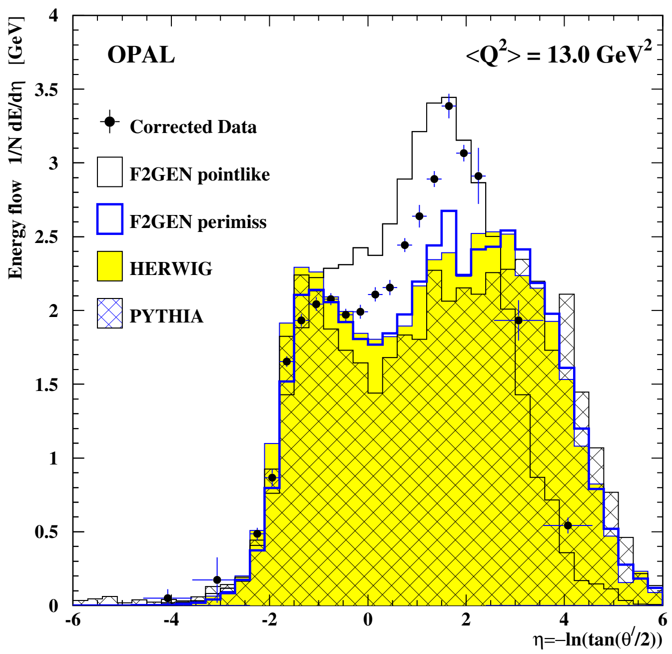

(a)

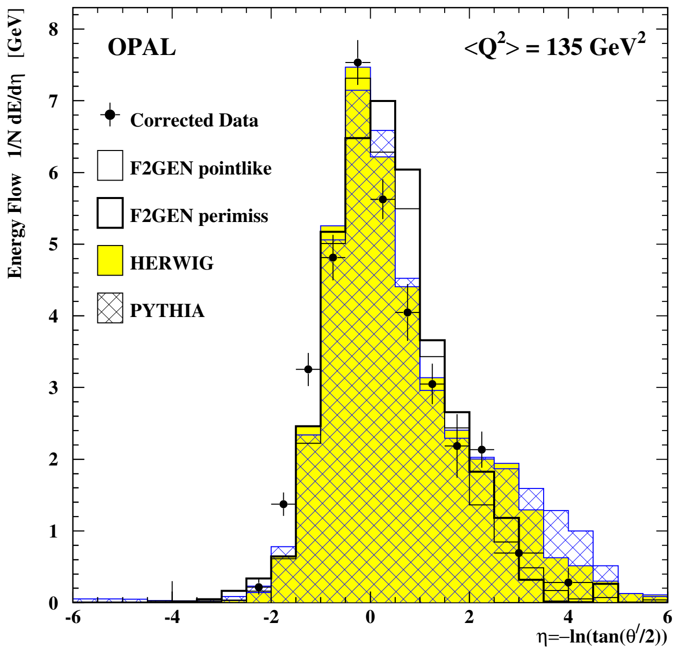

(b)

Figure 7.2: The hadronic energy flow per event as a function of pseudorapidity at (a) low and (b) high $\langle Q^2 \rangle$, for LEP1 data. Taken from Reference [10].

SW sample, this corresponds to a true value of W of less than about 16 GeV. At low to medium W the correlation between the measured invariant mass and the true value is much better than it is at the higher values required to access low x, so the results can be expected to have a smaller dependence on the Monte Carlo modelling of the hadronic final state. This is even more true for the high Q^2 EE sample, where the hadronic final state has much more transverse momentum (to balance the tag), and as a consequence is much better contained in the detector. This is demonstrated in Figure 7.2, which shows the hadronic energy flow as a function of pseudorapidity at low $\langle Q^2 \rangle$ (a) and at much higher $\langle Q^2 \rangle$ (b). These plots are take from an OPAL LEP1 publication [10], but there is no reason why the trend should be any different at LEP2 - the high-Q^2 sample is much better contained in the central part of the detector. This is reflected in the correlation between $W_{\rm vis}$ and the true value, Figure 7.3, which is very good even up to high values of W. For these reasons, one dimensional unfolding is appropriate for this analysis.

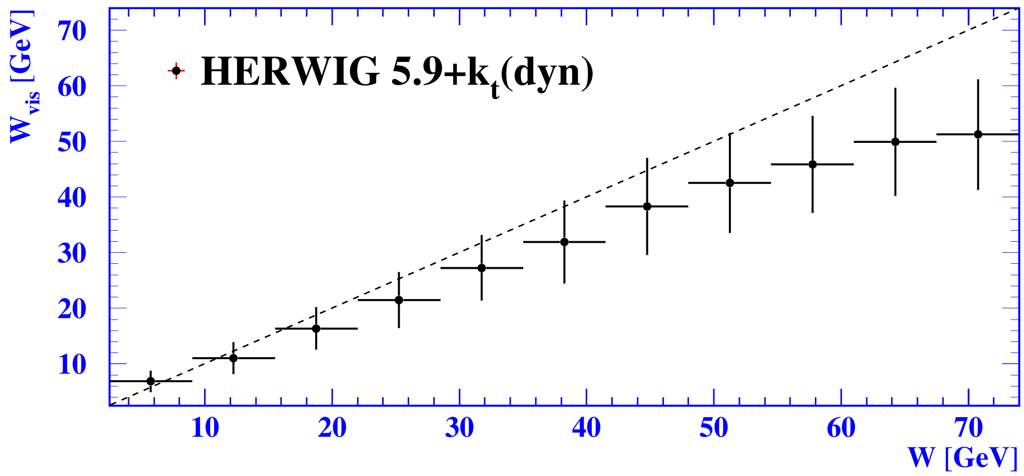

Figure 7.3: The correlation between the generated and measured hadronic invariant mass for the EE sample, as given by HERWIG 5.9+$k_{\rm t}$(dyn). The vertical error bars represent the rms spread within each bin. The dashed line corresponds to perfect correlation.

The previous analysis [13, 92] used new techniques to improve the reconstruction of W. This included scaling the energy in the forward region, to improve the measurement of hadronic energy in these electromagnetic calorimeters. The hadronic energy flow for the SW sample was studied in that analysis. On average, about 5% of the energy is deposited in SW, and about 20-25% in FD and SW combined. The numbers for the FD and EE samples are even lower, as inspection of Figure 7.2 would indicate. It was verified that scaling the energy in the forward region has a small impact on the measured F_2^γ for $x > 0.1$. Consequently, in the present analysis this energy is not scaled.

7.1.4 Unfolded distributions

The weight factors for each individual event, obtained from the unfolding, can be used to construct reweighted Monte Carlo distributions of different variables. The reweighted x_{vis} distribution should agree with the data by definition, but the reweighting will also change the shape of other measured variables. It is a valuable check of the unfolding procedure to compare these distributions, which are all differently correlated with x_{vis}, and see if the agreement with the data is improved by the unfolding. As an example, several reweighted HERWIG distributions for the EE sample are shown in Figure 7.4. It can be seen that the description of the data by the Monte Carlo is improved in all cases: for the unfolding variable x_{vis} (a), the variables directly correlated with x_{vis}, W_{vis} (b) and Q^2 (c) (although the Q^2 distribution was already well described), and even for a variable only indirectly correlated with x_{vis}, $E_{\mathrm{T,out}}$ (d).

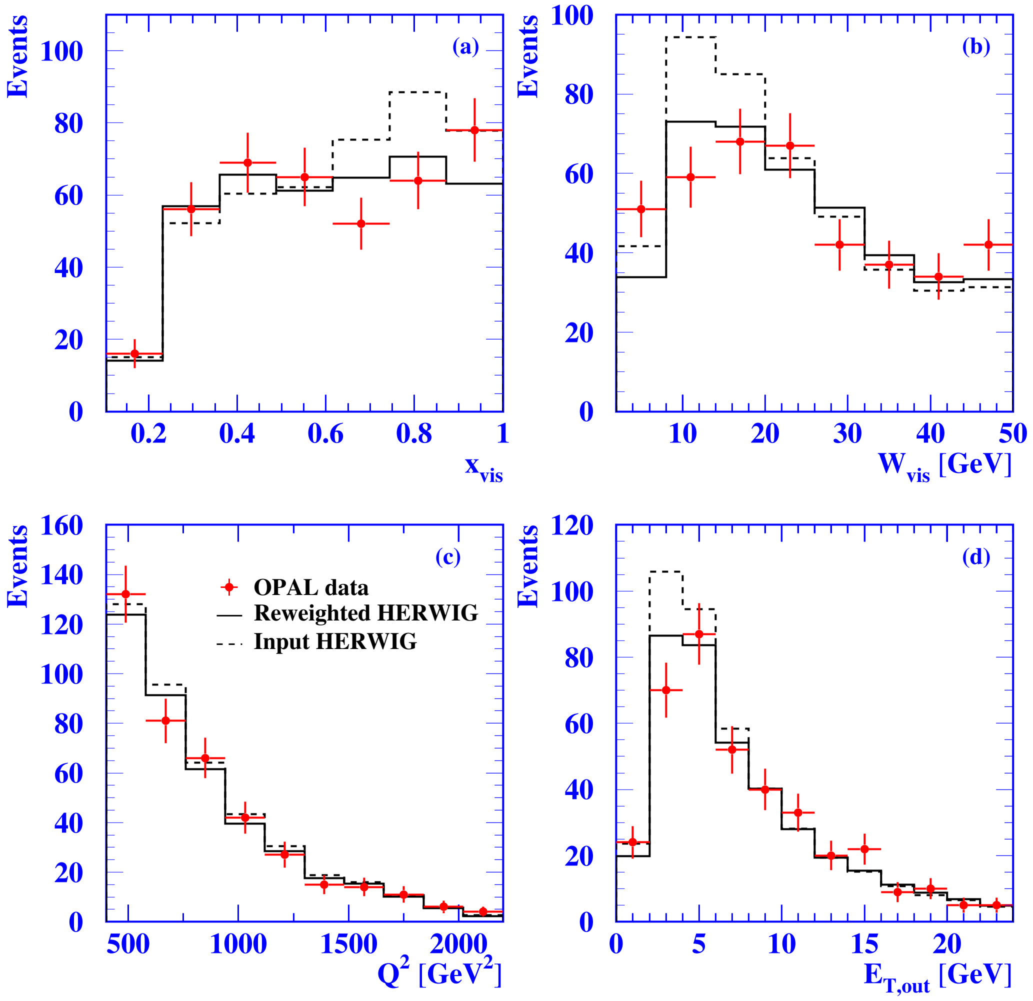

Figure 7.4: Reweighted HERWIG+k_t(dyn) Monte Carlo distributions for the EE sample, as output by the unfolding program. These are compared to the data and the original Monte Carlo distributions, which are equivalent to those shown in Figures 6.7, 6.8 and 6.9, although note that the binning is different in some cases. The distributions shown are (a) x_vis, (b) W_vis, (c) Q^2 and (d) $E_\mathrm{T,out}$. The background contributions have been added to the Monte Carlo histograms.

7.2 QED Radiative Corrections

None of the signal Monte Carlo programs used include QED radiative corrections to the deep inelastic scattering process, so when using them in an unfolding it is necessary to apply a correction to the result. The radiative corrections are dominated by initial state radiation from the tagged electron. Final state radiation is assumed to be unresolved experimentally due to the finite granularity of the calorimeters. The Compton process, in which the probe photon is of very low virtuality but the electron is tagged due to the emission of a final state photon at a large angle, contributes very little. It has been shown that corrections due to radiation from the untagged electron are very small (on the percent level) [97].

The RADEG program [98] has been used in this analysis to evaluate the corrections. The calculation uses the leading logarithmic approximation, which has been shown to be correct to within a few percent in the case of ep DIS. Mixed variables are used, which means that Q^2 is calculated from the scattered electron and W from the hadronic final state, so x is found in the same way as for the experimental case. The program allows calculation of differential cross-sections in bins of x and Q^2, with or without radiative corrections, while applying the experimental cuts on E_{tag}, θ_{tag}, W and the anti-tag angle. The predicted ratio of the differential cross-section for each bin of the analysis is used to correct the data, i.e. the measured F_2^γ is multiplied by the ratio of the non-radiative and radiative cross-sections. The SaS1D parameterisation of F_2^γ is used, but the predicted correction does not depend on the input structure function at the level of accuracy required for this analysis. SaS1D is chosen simply because the calculation is faster using it rather than, say, GRV.

The radiative corrections are predicted to reduce the cross-section in the phase space of this analysis, by between 4 and 9%. For a given value of Q^2 they are largest at low values of x. The correction applied to each data point is given in the tables of final results below, so should a more accurate calculation become available in the future the correction used here can easily be removed and a different one applied.

7.3 Target Virtuality Effects

The theoretical predictions for the effect of non-zero P^2 on $F_2^\gamma(x, Q^2, P^2)$ were discussed in Section 2.6. It was seen that there are significant differences between the various predictions, and that data able to constrain the predictions are not available. Therefore, to avoid biasing the result towards a particular prediction, and because the P^2 distribution in the data is not known, no correction is applied to the results in this analysis.

7.4 Measurement of F_2^γ at High Q^2

The measurements of the structure function F_2^γ and the differential cross-section at high Q^2 are obtained from the data by unfolding the x_{vis} distribution of the EE sample, after subtracting background and applying the additional restriction $400 < Q^2 < 2350$ GeV^2. Three bins in x, spanning the range 0.15–0.98, are used for the true variable. The central values are obtained using HERWIG as the input Monte Carlo model to the unfolding. Each data point is corrected for radiative effects as described in Section 7.2 above.

7.4.1 Bin-centre corrections

In order that the measured values of F_2^γ can easily be visually compared with the various parameterisations, and for convenience in making fits to the data, the measured values are corrected so that they represent F_2^γ at a particular value of x rather than the average F_2^γ within the bin. The plotted data points can then be directly compared to the theoretical curves at the x value at which they are plotted, which in this case is the centre of the bin. The correction is calculated by taking the average of the GRSc, SaS1D and WHIT1 predictions for the ratio of the value of F_2^γ at the nominal x position to the average F_2^γ over the bin. Note that only the results for the structure function F_2^γ are corrected in this way, not those for the differential cross-section.

7.4.2 Systematic errors

The systematic errors should take into account all uncertain aspects of the analysis, and the magnitude of the possible consequent bias on the results. They are estimated by varying one aspect of the analysis at a time, repeating the unfolding and finding the shift in the result. The systematic errors are then combined by adding all the individual contributions in quadrature. Positive and negative errors are summed separately since, in general, the systematic error may be asymmetric. The different systematic checks made are discussed in the following sections.

Some of the systematic variations can lead to changes in the composition of the selected events, either in the data, the Monte Carlo or both. This can have two effects on the result, aside from any systematic shift. First, the $\langle Q^2 \rangle$ of the sample can change, leading to a shift in the result because of the dependence of F_2^γ on Q^2. However, since the dependence is only logarithmic and the variations are small enough not to change $\langle Q^2 \rangle$ by a large amount, this effect can safely be neglected. The second effect is that changing the event composition of a given bin can lead to a statistical fluctuation in the result. Thus each systematic error in principle contains a statistical component, which will amplify the total estimated error. The last OPAL analysis [13, 92] included a procedure to subtract this statistical component. This procedure is not used here. In any case, the error on the high-Q^2 measurement is dominated by the statistical error on the data.

Model dependence

As has already been discussed, the result can depend on the Monte Carlo model used in the unfolding. The uncertainty due to this is estimated by repeating the unfolding using the Vermaseren sample as input and taking the full magnitude of the difference as the systematic error, for both the positive and negative error. One could envisage that changing the input structure function used when generating the Monte Carlo events could have an effect on the result. The result should not, however, depend on the shape of the input true x distribution, and it was verified in the last OPAL analysis [13, 92] that this is indeed the case.

Variations of cuts

The composition of the selected events is varied by changing the cuts one at a time. Changing the cuts is a means of testing various systematic effects. These include the effect and modelling of background contamination near the cut boundaries, poor reconstruction of variables and uncertainties in the acceptance. The variations made are listed in Table 7.1. The size of the variations reflect the resolution of the measured variables and the description of the data by the Monte Carlo around the cut values.

Cut	EE
$E_{\rm tag}/E_{\rm b}$ min	$\pm 0.05\,(0.70)$
$\theta_{\rm tag}$ min [mrad]	$\pm 5\,(230)$
$\theta_{\rm tag}$ max [mrad]	$\pm 5\,(500)$
$E_{\rm a}/E_{\rm b}$ max	$\pm 0.05\,(0.25)$
$N_{\rm trk}$ min	$+1\,(4)$
$W_{\rm vis}$ min [GeV]	$+1\,(2.5)$
$W_{\rm vis}$ max [GeV]	$\pm 5\,(50)$
Electron isolation [GeV]	$\pm 0.5\,(3.0)$

Table 7.1: The systematic variations applied to the cuts for the EE sample, with the standard cuts given in brackets.

Unfolding parameters

There is no reason why the number of bins used for the measured variable needs to be the same as the number used for the true variable. The standard result has 5 bins in the measured variable. This is in turn reduced to 4 and increased to 6 to estimate the systematic effects of the unfolding.

Calibration of the tagging detector

To allow for the uncertainty in the calibration of the EE, the energy of the tagged electron in the Monte Carlo is scaled by $\pm 1\%$. This is conservative, because the calibration is known much more accurately than this through the analysis of Bhabha events [99].

Measurement of the hadronic energy

The main uncertainty is in the calibration of the response of the electromagnetic calorimeter to hadronic energy for low energy particles in the hadronic final state. To estimate this uncertainty, the absolute energy scale is varied by $\pm 3\%$ [100] in the Monte Carlo samples. It was found in the previous OPAL analysis [13, 92] that the systematic effect of varying the tracking parameters or resolution is negligible.

Background modelling

The dominant background in this sample, stemming from the reaction $\mathrm{Z}^0/\gamma^\star \rightarrow$ hadrons, is also the one on which there is the greatest uncertainty. Since a fake tag can be provided either an energetic particle within a hadronic jet or by an ISR photon, the modelling of the final state fragmentation and the treatment of ISR is important. To quantify the uncertainty, the KK2f program along with cluster fragmentation is used instead of PYTHIA with string fragmentation.

Cone size for the W_{vis} calculation

The uncertainty arising from the choice of 200 mrad half-angle as the size of the exclusion cone for the W_{vis} calculation is estimated by varying the size of the cone by ± 30 mrad.

When all the individual systematic errors are combined the total estimated systematic error is of the same order as the statistical error. The full breakdown of the individual contributions is given in Table 7.7, where the errors are given as percentages of the measured F_2^γ. It can be seen that no single error source is dominant.

7.4.3 Results

The result for F_2^γ/α is listed in Table 7.2 together with the correlation matrix. In each bin of x the result for $\mathrm{d}\sigma/\mathrm{d}x$ is also listed. The $\mathrm{d}\sigma/\mathrm{d}x$ values are corrected to the phase space given by the Q^2 range, $P^2 < 4.5$ GeV^2 and $y < 0.3$. The measured F_2^γ/α, shown in Figure 7.5 together with several theoretical calculations, exhibits a flat behaviour. It can be seen that in this high-Q^2 regime the differences between the different predictions are rather small, particularly in the central x-region. All these predictions are compatible with the data to within about 20%, with the WHIT1 parameterisation, which predicts the flattest behaviour, being closest to the data. The QPM curve, which models only the point-like component of F_2^γ, shows a much steeper behaviour in x and is disfavoured by the data.

x range	x bin-centre	F_2^γ/α	$\mathrm{d}\sigma/\mathrm{d}x$ [pb]	radiative correction [%]	bin-centre correction [%]
$0.15 - 0.40$	0.275	$0.93 \pm 0.10 ^{+0.14}_{-0.11}$	$0.94 \pm 0.11 ^{+0.15}_{-0.11}$	-8.8	-0.4
$0.40 - 0.70$	0.550	$0.87 \pm 0.10 ^{+0.05}_{-0.15}$	$0.79 \pm 0.09 ^{+0.05}_{-0.14}$	-6.9	0.1
$0.70 - 0.98$	0.840	$0.97 \pm 0.17 ^{+0.16}_{-0.23}$	$0.62 \pm 0.11 ^{+0.10}_{-0.15}$	-5.4	-5.1

x range	$0.15 - 0.40$	$0.40 - 0.70$	$0.70 - 0.98$
$0.15 - 0.40$	1.00		
$0.40 - 0.70$	0.16	1.00	
$0.70 - 0.98$	-0.04	-0.15	1.00

Table 7.2: Results for F_2^γ/α as a function of x at $\langle Q^2 \rangle$ of 780 GeV^2, and for $\mathrm{d}\sigma/\mathrm{d}x$ in the Q^2 range 400-2350 GeV^2 and $y < 0.3$. The first errors are statistical and the second systematic. The data are unfolded in bins defined by the x ranges and corrected for radiative effects. For a given bin the radiative correction is the difference of the radiative and non-radiative cross-sections as a percentage of the non-radiative cross-section. The structure function is corrected to the x values listed using the bin-centre corrections which are given as a percentage of the non-corrected F_2^γ. The statistical correlations between the bins for the central result are also given.

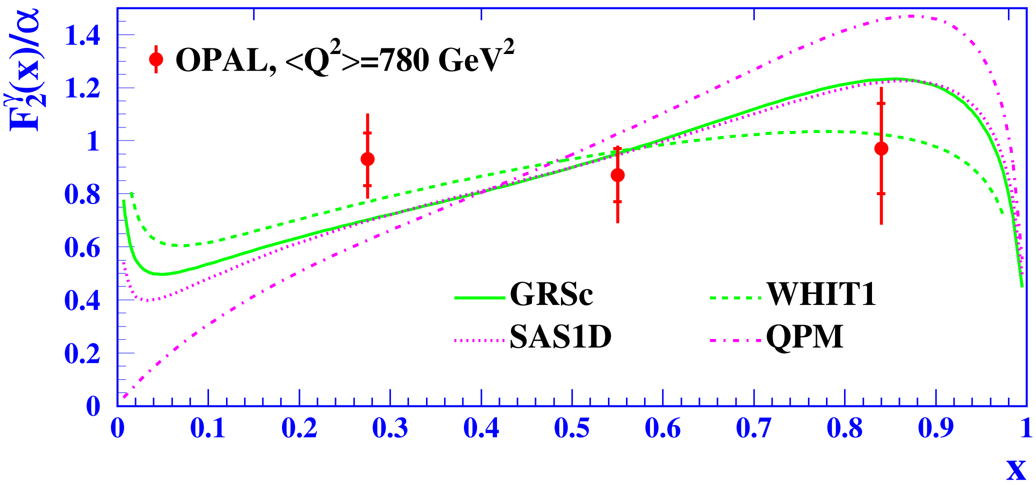

Figure 7.5: The measured F_2^γ/α as a function of x for the EE sample. The data are unfolded for $\langle Q^2 \rangle = 780$ GeV^2 and compared to the leading order predictions from the GRSc (full line), SaS1D (dotted line), WHIT1 (dashed line) and QPM (dot-dashed line) parameterisations of F_2^γ/α. The inner error bars represent the statistical errors and the full error bars represent the statistical and systematic errors added in quadrature. The tick marks at the top of the figure represent the bin boundaries.

7.5 Measurement of the Q^2 Evolution of F_2^γ

The second measurement performed in this analysis is that of the evolution of F_2^γ with Q^2, using all three samples. Due to the large statistics, the SW and FD samples are further split into two bins of Q^2 (9–15 and 15–30 GeV^2 for SW and 30–50 and 50–150 GeV^2 for FD). The data are unfolded as a function of x separately in each bin of Q^2, using HERWIG as the input Monte Carlo, and are corrected for radiative effects. To allow a direct comparison with the previous OPAL study of the scaling violations of F_2^γ, several ranges of x are used; first, the central region 0.1–0.6, and then the adjacent ranges 0.1–0.25, 0.25–0.6 and 0.6–0.85.

7.5.1 Systematic errors

The estimation of the systematic errors for the EE sample is described above. The estimation for the SW and FD samples mirrors the procedure for the EE sample, with some differences.

The PHOJET program (with the reweighting described in Section 7.1.3) is used as a second Monte Carlo to determine the model dependence. The variations made to the cuts are given in Table 7.3. Note that the θ_{tag} cuts are varied in only one direction, away from the edges of the detectors, since the full region of good acceptance is already used for the default cuts. For the unfolding parameters the standard number of bins in the measured variable, which was 8 for the central values, is varied by ± 2. No systematics due to the electron isolation are needed for the SW and FD samples.

With only two models available that satisfactorily describe the data [13, 92], the estimated systematic error is small for those x, Q^2 regions where the two models happen to predict similar correlations between x and x_{vis}. To reduce fluctuations within the SW and FD samples, the systematic error from this

Cut	SW	FD
$E_{\rm tag}/E_{\rm b}$ min	$\pm 0.05\,(0.75)$	
$\theta_{\rm tag}$ min [mrad]	$+2\,(33.25)$	$+3\,(60)$
$\theta_{\rm tag}$ max [mrad]	$-2\,(55)$	$-3\,(120)$
$E_{\rm a}/E_{\rm b}$ max	$\pm 0.05\,(0.25)$	
$N_{\rm trk}$ min	$+1\,(3)$	
$W_{\rm vis}$ min [GeV]	$+1\,(2.5)$	
$W_{\rm vis}$ max [GeV]	$\pm 5\,(60)$	

Table 7.3: The systematic variations applied to the cuts for the SW and FD samples, with the standard cuts given in brackets.

source has been averaged for each region of x for the two Q^2 points within a given sample. For the FD and SW samples, the total systematic error is on average about double the size of the statistical error, with the largest contribution to the systematic error generally stemming from the estimated model dependence. Once again, the full breakdown is given in Table 7.7.

7.5.2 Results

The results for F_2^γ in the central region of x, 0.1–0.6, are shown in Figure 7.6, along with the previous OPAL measurements [11] and a number of parameterisations. Table 7.4 lists the results for F_2^γ and $\mathrm{d}\sigma/\mathrm{d}x$. Note that no bin-centre corrections are applied - these results correspond to the average F_2^γ/α in the bin, rather than at a specific value of x. From Figure 7.6 the significant improvement in accuracy at medium Q^2, compared to the OPAL measurements performed at lower $\mathrm{e}^+\mathrm{e}^-$ centre-of-mass energies, is immediately apparent, as is the increased lever arm in Q^2. The status of the world data on the evolution of F_2^γ with Q^2 in the central x region, prior to the present analysis, is shown in Figure 7.7. The measurement presented here is comfortably the most accurate to date, and also extends to the highest value of Q^2.

An increase of F_2^γ/α with Q^2 is observed in the data, in agreement with QCD (and QPM) predictions. To quantify the slope, the data are fitted using a linear function of the form $a + b \ln Q^2$, where Q^2 is in GeV^2. Within the range of x fitted the parameters a and b are assumed to be independent of x. To obtain the central values of the two parameters, with their statistical errors and correlation, a fit is performed by the MINUIT [101] program using the measured values of F_2^γ/α and their statistical errors. The fit is repeated for each of the systematic variations. The systematic errors of a and b are estimated as the quadratic sum of the deviations of the two parameters from the central values. The result of the fit is

$$F_2^\gamma(Q^2)/\alpha = (0.08 \pm 0.02\,^{+0.05}_{-0.03}) + (0.13 \pm 0.01\,^{+0.01}_{-0.01}) \ln Q^2\,,$$

with, for the central result, a correlation between the two parameters of -0.98 and a χ^2 of 10 for 3 degrees of freedom. No significant change in the result is observed if the fit is performed using the full error on each point. The fit result is also shown in Figure 7.6, where it indicates that the data exhibit a steeper slope than any of the parameterisations. This new result compares to the previous OPAL value [11] of

$$F_2^\gamma(Q^2)/\alpha = (0.16 \pm 0.05\,^{+0.17}_{-0.16}) + (0.10 \pm 0.02\,^{+0.05}_{-0.02}) \ln Q^2.$$

These two determinations, based on independent data sets, are in agreement, and the errors on a and b have been strongly reduced.

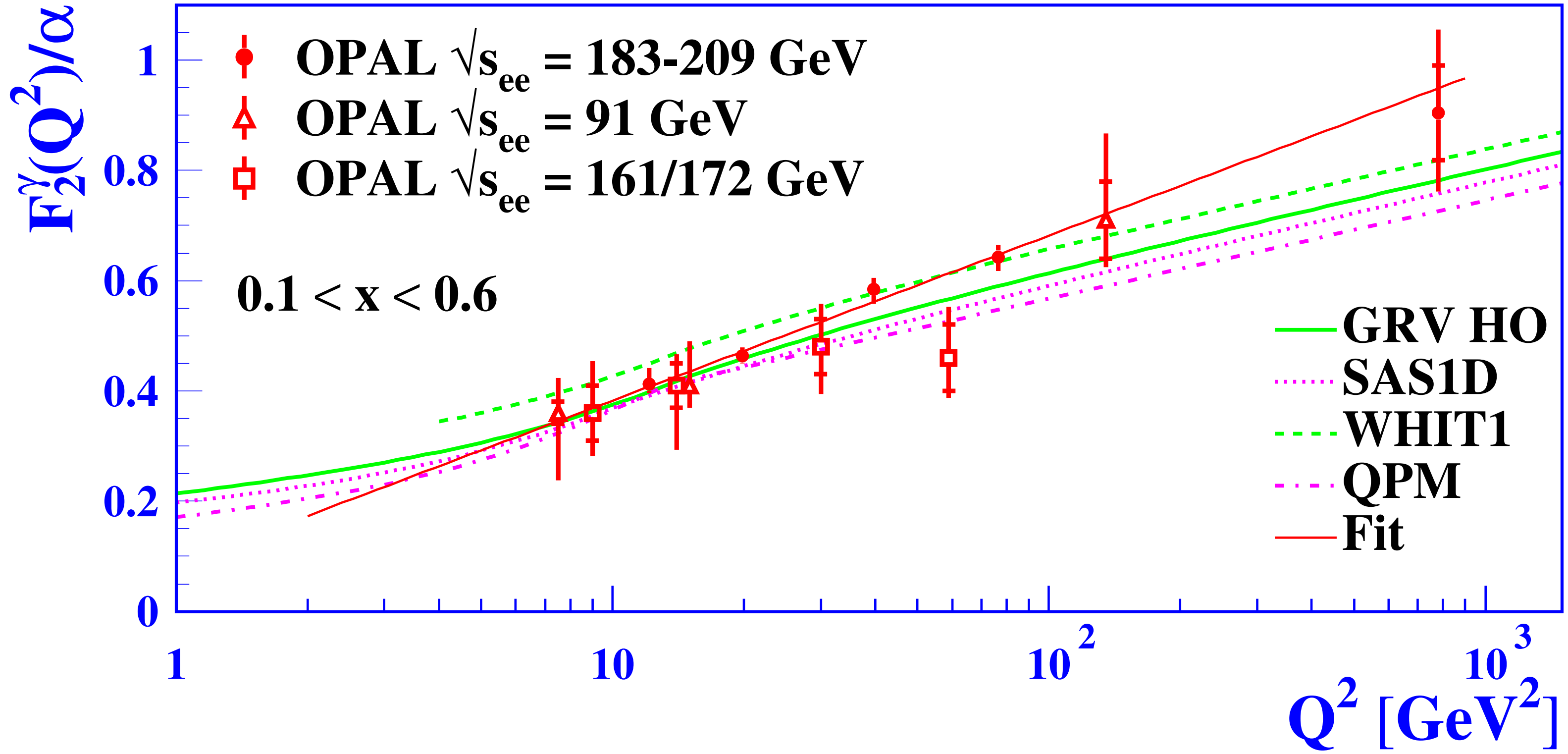

Figure 7.6: The measured evolution of F_2^γ with Q^2 for the central x region, 0.10–0.60. The inner error bars represent the statistical errors and the full error bars represent the statistical and systematic errors added in quadrature. The data are compared to the predictions from the GRV higher order (full line), SaS1D (dotted line), WHIT1 (dashed line), and QPM (dot-dashed line) parameterisations of F_2^γ/α.

x range	Q^2range [GeV^2]	$\langle Q^2 \rangle$ [GeV^2]	F_2^γ/α	$\mathrm{d}\sigma/\mathrm{d}x$ [pb]	radiative correction [%]
0.10 − 0.60	9 − 15	12.1	$0.41 \pm 0.01\,^{+0.03}_{-0.02}$	$57 \pm 1\,^{+4}_{-2}$	−4.7
	15 − 30	19.9	$0.46 \pm 0.01\,^{+0.01}_{-0.01}$	$42 \pm 1\,^{+1}_{-1}$	−4.9
	30 − 50	39.7	$0.58 \pm 0.01\,^{+0.02}_{-0.02}$	$17.7 \pm 0.3\,^{+0.6}_{-0.7}$	−5.3
	50 − 150	76.4	$0.64 \pm 0.01\,^{+0.02}_{-0.02}$	$15.3 \pm 0.3\,^{+0.4}_{-0.5}$	−5.6
	400 − 2350	780	$0.90 \pm 0.09\,^{+0.13}_{-0.11}$	$0.86 \pm 0.08\,^{+0.12}_{-0.11}$	−8.2

Table 7.4: Results for the average F_2^γ/α in the central x region at several values of $\langle Q^2 \rangle$ and for $\mathrm{d}\sigma/\mathrm{d}x$ in several ranges of Q^2. The first errors are statistical and the second systematic. The data are unfolded in bins defined by the x and Q^2 ranges listed. The radiative corrections which have been applied are also listed. For a given bin the radiative correction is the difference of the radiative and non-radiative cross-sections as a percentage of the non-radiative cross-section.

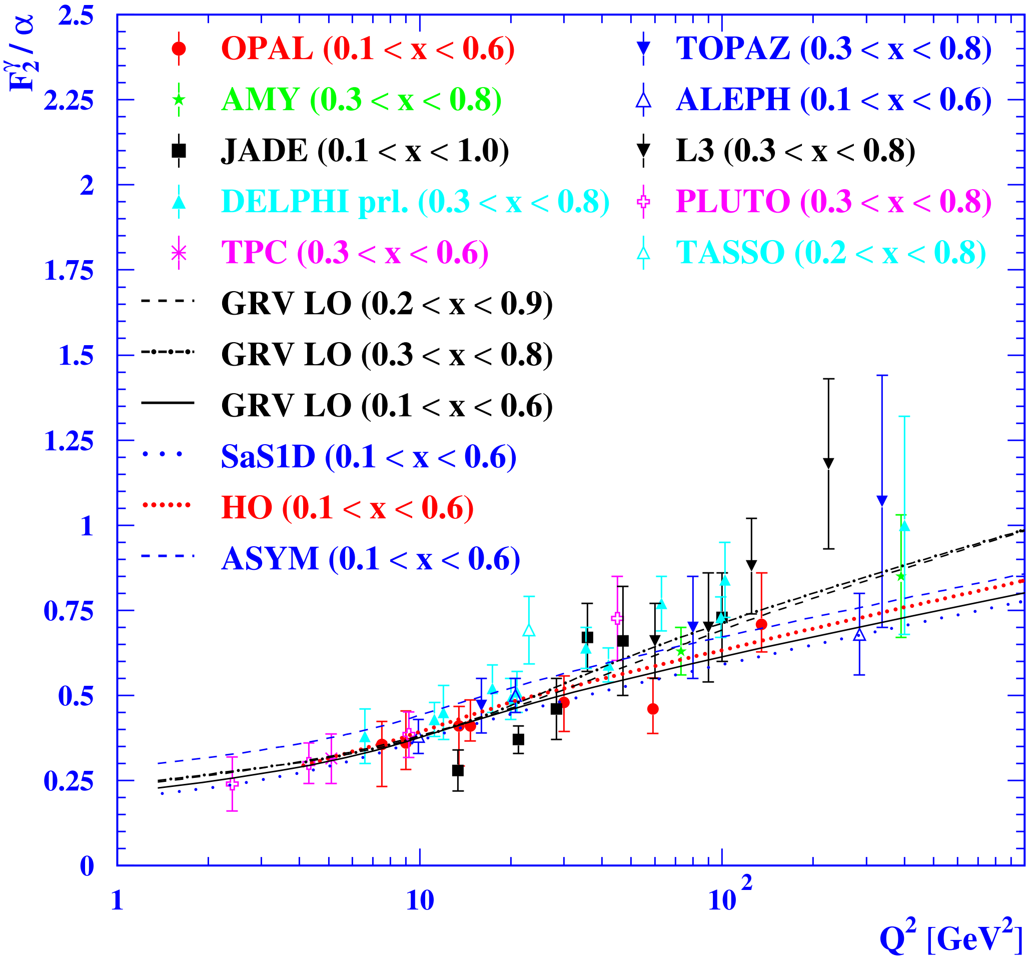

Figure 7.7: The world data (prior to the present measurement) on the evolution of F_2^γ with Q^2 in the central x region. Taken from Reference [1].

In order to test the predictions for the scaling violation behaviour of F_2^γ at different values of x, results are also presented for several ranges of x. These are shown in Figure 7.8 and listed in Table 7.5, where the results for $\mathrm{d}\sigma/\mathrm{d}x$ are also given. Table 7.6 gives the statistical correlations between the points at each value of $\langle Q^2 \rangle$. The data show positive scaling violations in F_2^γ for the x ranges 0.10–0.25 and 0.25–0.60. The QCD inspired parameterisations of F_2^γ qualitatively follow the data, but do not perfectly account for them. For the SW sample the GRSc and SaS1D predictions, which are almost indistinguishable, closely resemble the data, whereas at higher Q^2, for the FD sample, WHIT1 comes closest. For the range 0.60–0.85, the data are compatible with the predicted scaling violations of the QCD inspired parameterisations. The QPM model generally gives a bad description of the data, especially at low x.

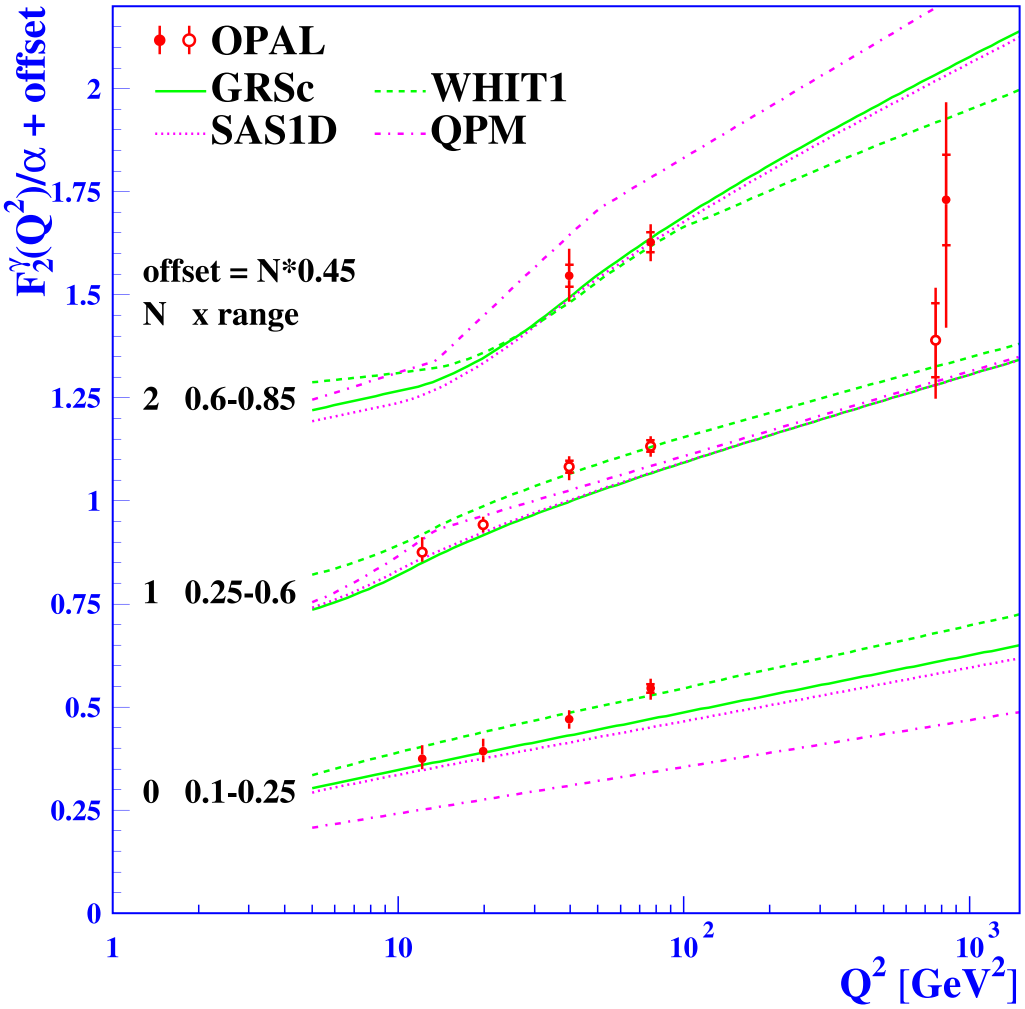

Figure 7.8: The measured evolution of F_2^γ with Q^2 for several bins of x. The inner error bars represent the statistical errors and the full error bars represent the statistical and systematic errors added in quadrature. The data are compared to the predictions from the GRSc (full line), SaS1D (dotted line), WHIT1 (dashed line), and QPM (dot-dashed line) parameterisations of F_2^γ/α.

x range	Q^2range [GeV^2]	$\langle Q^2 \rangle$ [GeV^2]	F_2^γ/α	dσ/dx [pb]	radiative correction [%]
$0.10 - 0.25$	$9 - 15$	12.1	$0.38 \pm 0.01\,^{+0.03}_{-0.03}$	$83 \pm 1\,^{+7}_{-6}$	-5.3
$0.25 - 0.60$			$0.43 \pm 0.01\,^{+0.03}_{-0.02}$	$47 \pm 1\,^{+4}_{-2}$	-4.4
$0.10 - 0.25$	$15 - 30$	19.9	$0.39 \pm 0.01\,^{+0.03}_{-0.03}$	$56 \pm 1\,^{+4}_{-4}$	-5.5
$0.25 - 0.60$			$0.49 \pm 0.01\,^{+0.02}_{-0.02}$	$36 \pm 1\,^{+1}_{-1}$	-4.5
$0.10 - 0.25$	$30 - 50$	39.7	$0.47 \pm 0.01\,^{+0.02}_{-0.02}$	$21.7 \pm 0.4\,^{+0.9}_{-0.9}$	-5.9
$0.25 - 0.60$			$0.63 \pm 0.01\,^{+0.02}_{-0.03}$	$15.9 \pm 0.4\,^{+0.5}_{-0.7}$	-4.8
$0.60 - 0.85$			$0.65 \pm 0.03\,^{+0.06}_{-0.06}$	$9.6 \pm 0.4\,^{+0.9}_{-0.8}$	-3.8
$0.10 - 0.25$	$50 - 150$	76.4	$0.55 \pm 0.01\,^{+0.02}_{-0.03}$	$18.8 \pm 0.4\,^{+0.7}_{-0.9}$	-6.5
$0.25 - 0.60$			$0.68 \pm 0.01\,^{+0.02}_{-0.02}$	$13.8 \pm 0.3\,^{+0.4}_{-0.4}$	-5.2
$0.60 - 0.85$			$0.73 \pm 0.02\,^{+0.04}_{-0.04}$	$9.1 \pm 0.3\,^{+0.4}_{-0.5}$	-4.1
$0.25 - 0.60$	$400 - 2350$	780	$0.94 \pm 0.09\,^{+0.09}_{-0.11}$	$0.91 \pm 0.09\,^{+0.08}_{-0.10}$	-7.6
$0.60 - 0.85$			$0.83 \pm 0.11\,^{+0.21}_{-0.29}$	$0.71 \pm 0.09\,^{+0.18}_{-0.25}$	-6.0

Table 7.5: Results for the average F_2^γ/α in several bins of x at several values of $\langle Q^2 \rangle$ and for dσ/dx in several ranges of Q^2. The first errors are statistical and the second systematic. The data are unfolded in bins defined by the x and Q^2 ranges listed. The radiative corrections which have been applied are also listed. For a given bin the radiative correction is the difference of the radiative and non-radiative cross-sections as a percentage of the non-radiative cross-section.

x range	$0.10-0.25$	$0.25-0.60$	$0.60-0.85$
$0.10-0.25$	1		
$0.25-0.60$	$0.00/0.28/0.45/0.40/-$	1	
$0.60-0.85$	$-/-/-0.23/-0.19/-$	$-/-/0.32/0.27/0.17$	1

Table 7.6: The statistical correlations between the x bins for the central results given in Table 7.5, for the $\langle Q^2\rangle$ values 12.1/19.9/39.7/76.4/780 GeV^2.

$\langle Q^2 \rangle$ [GeV^2]	x range	F_2/α	Statistical error	Total systematic +	Total systematic -	Model dependence	$E_{\rm tag}$ min +	$E_{\rm tag}$ min -	$\theta_{\rm tag}$ min +	$\theta_{\rm tag}$ min -	$\theta_{\rm tag}$ max +	$\theta_{\rm tag}$ max -	$E_{\rm a}$ max +	$E_{\rm a}$ max -	$N_{\rm trk}$ min +	$W_{\rm vis}$ min +	$W_{\rm vis}$ max +	$W_{\rm vis}$ max -	Electron isolation +	Electron isolation -	Unfolding bins +	Unfolding bins -	Tag calibration +	Tag calibration -	ECAL scale +	ECAL scale -	Background	Cone size +	Cone size -
12.1	0.10–0.60	0.41	1.6	6.9	3.8	2.5	-1.9	2.1	5.5	-	-	0.0	-0.1	0.0	1.7	-0.6	0.0	0.0	-	-	-0.2	0.1	-1.6	1.6	1.2	-1.3	0.0	-	-
	0.10–0.25	0.38	1.5	8.6	6.9	6.6	-1.3	2.8	3.2	-	-	0.0	-0.1	-0.1	3.3	0.6	-0.1	0.0	-	-	-0.5	-1.0	-0.4	0.3	-0.1	-0.3	0.0	-	-
	0.25–0.60	0.43	2.2	8.0	5.0	3.3	-2.2	2.0	6.3	-	-	0.0	-0.1	0.0	1.0	-1.1	0.1	0.0	-	-	0.0	0.6	-2.2	2.1	1.8	-1.8	0.0	-	-
19.9	0.10–0.60	0.46	1.3	3.1	2.6	2.2	-1.1	0.7	0.0	-	-	-0.4	0.1	-0.1	1.1	0.3	0.1	0.0	-	-	0.1	1.3	-0.7	0.9	0.8	-0.1	0.0	-	-
	0.10–0.25	0.39	1.4	7.6	6.6	6.3	-1.5	0.6	0.0	-	-	-0.5	0.1	-0.2	2.7	1.5	0.0	0.0	-	-	0.4	2.4	-0.2	0.2	-0.4	1.4	0.0	-	-
	0.25–0.60	0.49	1.6	3.6	3.3	2.9	-0.9	0.7	0.0	-	-	-0.3	0.1	0.0	0.5	-0.2	0.1	0.0	-	-	0.0	0.8	-1.0	-0.7	1.3	-0.7	0.1	-	-
39.7	0.10–0.60	0.58	1.9	3.2	4.0	2.4	-2.0	1.0	1.2	-	-	0.0	0.0	-0.3	0.1	-1.3	0.0	-0.1	-	-	-0.5	-1.6	-1.1	1.2	0.6	-0.5	0.0	-	-
	0.10–0.25	0.47	2.1	4.3	4.4	4.1	-0.4	0.3	-0.6	-	-	0.0	0.0	-0.1	-0.4	0.3	-0.1	0.0	-	-	-0.4	-0.3	-0.9	0.5	-0.6	0.5	0.0	-	-
	0.25–0.60	0.63	2.2	3.4	4.6	1.7	-2.6	1.4	1.9	-	-	0.0	0.0	-0.4	0.2	-2.0	0.0	-0.1	-	-	-0.5	-2.2	-1.2	1.3	1.0	-0.9	0.0	-	-
	0.60–0.85	0.65	4.2	9.2	8.8	2.7	-3.2	0.2	6.9	-	-	0.0	0.0	-0.3	-2.8	-6.4	-0.2	0.0	-	-	2.1	4.5	-2.6	2.0	1.6	-2.0	0.0	-	-
76.4	0.10–0.60	0.64	1.8	2.9	3.5	2.2	-0.8	0.4	0.0	-	-	0.2	0.8	-0.7	-2.3	0.1	0.0	0.1	-	-	-0.3	1.1	-1.0	1.2	0.3	-0.1	-0.1	-	-
	0.10–0.25	0.55	1.9	3.9	4.7	3.5	-0.5	-1.0	0.0	-	-	0.0	0.7	-0.2	-2.3	0.0	0.0	-0.2	-	-	-0.7	0.4	-1.0	1.1	-1.1	1.0	-0.2	-	-
	0.25–0.60	0.68	2.1	2.9	3.2	1.6	-0.9	0.9	0.0	-	-	0.2	0.9	-0.9	-2.2	0.2	-0.1	0.3	-	-	-0.1	1.4	-1.0	1.2	0.8	-0.5	0.0	-	-
	0.60–0.85	0.73	3.4	4.9	5.5	2.4	-3.0	2.3	0.0	-	-	0.1	1.6	-1.2	-1.5	1.3	0.0	0.1	-	-	-0.5	-1.3	-1.9	1.9	2.3	-2.5	0.0	-	-
780	0.10–0.60	0.90	9.4	13.8	12.7	10.8	4.4	1.5	1.0	-4.2	-0.5	-0.6	1.3	3.3	1.2	0.5	3.5	-4.0	0.1	0.4	-0.9	3.6	-1.6	2.3	2.3	-0.8	-2.5	1.1	0.5
	0.25–0.60	0.94	9.5	8.6	10.4	8.2	-3.8	-1.2	0.8	-2.5	-1.3	-0.6	-0.1	-0.5	1.1	-0.1	-1.7	0.2	-1.4	0.0	-1.6	-0.5	0.2	-0.5	-0.9	0.3	-2.8	0.2	1.5
	0.60–0.85	0.83	13.1	25.2	33.8	25.0	2.1	-9.2	-4.1	1.9	-3.5	-0.3	-0.4	0.2	-7.2	-1.9	-1.8	-6.7	0.6	0.1	-8.0	-15.2	0.1	-1.1	-1.2	-3.3	-5.7	-1.0	-2.7
	0.15–0.40	0.93	11.2	15.4	12.1	8.0	4.9	2.2	-5.4	1.0	-0.6	0.8	2.7	4.4	-0.4	1.0	5.1	-6.4	-0.5	0.4	2.0	7.9	1.5	-0.8	-1.9	2.1	-2.7	0.8	1.8
	0.40–0.70	0.87	11.6	6.2	17.4	5.2	-4.0	-3.6	-0.2	0.2	-1.6	-0.5	-3.0	-0.6	3.1	-0.9	-4.2	1.3	-0.8	-0.5	-7.4	-11.4	-0.6	-0.3	0.0	-1.0	-3.3	-0.3	-1.2
	0.70–0.98	0.97	18.1	16.6	24.1	5.7	5.2	-3.4	1.9	-0.5	4.4	1.1	3.7	1.8	-18.1	-5.8	1.1	-7.2	0.1	0.3	8.3	8.2	-2.3	-0.1	5.9	-1.0	-9.3	-2.4	-1.9

Table 7.7: A full breakdown of the contributions to the systematic error on F_2^γ/α for all the results presented in this thesis. The statistical errors and the contributions to the systematic error from each of the sources are listed as percentages of F_2^γ/α (or $\mathrm{d}\sigma/\mathrm{d}x$, since the percentage errors are identical). The systematic errors are summed in quadrature separately for positive and negative contributions, except for 'Model dependence' which is symmetric.

Chapter 8

Conclusions

The photon structure function F_2^γ and the differential cross-section $\mathrm{d}\sigma/\mathrm{d}x$ have been measured using deep inelastic electron-photon scattering events recorded by the OPAL detector during the years 1997–2000 with an integrated luminosity of 632 pb^{-1} and an average $\mathrm{e^+e^-}$ centre-of-mass energy of 197.1 GeV.

The structure function F_2^γ has been measured as a function of x in the range $0.15 < x < 0.98$ and at an average photon virtuality of $\langle Q^2\rangle = 780$ GeV^2. The Q^2 evolution of F_2^γ has been studied for $12.1 < \langle Q^2\rangle < 780$ GeV^2 using several ranges of x. The data exhibit positive scaling violations in F_2^γ for the x ranges 0.10–0.25 and 0.25–0.60. For the range 0.60–0.85, the data are compatible with the predicted scaling violations. The measured evolution of F_2^γ/α as a function of Q^2 in the central region of x, 0.10–0.60, has been fitted with a linear function in $\ln Q^2$, resulting in

$$F_2^\gamma(Q^2)/\alpha = (0.08\ \pm 0.02\,{}^{+0.05}_{-0.03}) + (0.13\ \pm 0.01\,{}^{+0.01}_{-0.01})\ \ln Q^2\,,$$

where Q^2 is in GeV^2.

Both for the measurement of F_2^γ at $\langle Q^2\rangle = 780$ GeV^2 and for the investigation of the Q^2 evolution of F_2^γ, the quark-parton model prediction is not in agreement with the data. It shows a much steeper rise than the data as a function of x for $\langle Q^2 \rangle = 780$ GeV^2 and also a different behaviour in the Q^2 evolution. In contrast, the leading order GRSc, SaS1D and WHIT1 parameterisations and the higher order GRV parameterisation of F_2^γ are much closer to the data. This means that the corresponding parton distribution functions of the photon are adequate to within about 20% at large values of x and at $\langle Q^2 \rangle$ scales of about 780 GeV^2.

As well as reaching the highest value of $\langle Q^2 \rangle$ thus far, these results also represent the most accurate measurement, to date, of F_2^γ at medium x and Q^2. There is scope for further improvement, however. Because of the limited statistics, the measurement of F_2^γ at high Q^2 could benefit from a combination with the data of other LEP experiments. It is this possibility that is the main motivation for the presentation of the results in terms of the differential cross-section as well as F_2^γ. Such a combination would, however, make it desirable to reduce the systematic error on the measurement. This could be achieved by revisiting the analysis and employing the method used in the previous OPAL measurement [13, 92] to subtract the statistical components which are certainly currently present in the systematic error. As well as in a combination, the $\mathrm{d}\sigma/\mathrm{d}x$ results could also be employed to integrate this measurement into the framework of the HZTOOL package [102], which facilitates the global comparison of photoproduction data with Monte Carlo models, e.g. for tuning purposes.

The measurements presented here have already been used in a new fit to determine the value of the strong coupling constant [103]. It has been demonstrated that the most recent LEP data have reduced the experimental error to such a degree that a competitive determination of α_s from F_2^γ is now possible.

The results of this analysis have been published in *Physics Letters* [104].

Appendix A

Studies of Bhabha Events

A.1 Electrons in EE

In order to elucidate the extent and nature of the showering of high energy electrons in the dead material in front of the EE, a study of Bhabha events with the electrons detected in the EE was carried out. Bhabha events were selected in the 1998 data using essentially the criteria of the 'large acceptance' sample of the standard OPAL wide-angle Bhabha analysis [99], with the modification that the highest energy cluster was found in the polar angle region of the EE used in the present analysis. Mainly because these criteria include the requirement of high energy, back-to-back clusters, this selection results in a very high purity sample, so one can be confident that it is really electrons that are being studied. Figure A.1(a) shows a histogram of the distances of CT and ECAL objects (tracks or clusters) from the highest energy cluster (equivalent to the tag, and referred to as such). Each such object in an event enters the histogram separately. Also shown, normalised to the data luminosity, is the prediction of the BHWIDE [105] Monte Carlo program after GOPAL simulation, which significantly undershoots the data. This may appear to be simply a normalisation problem, but in fact the cross-

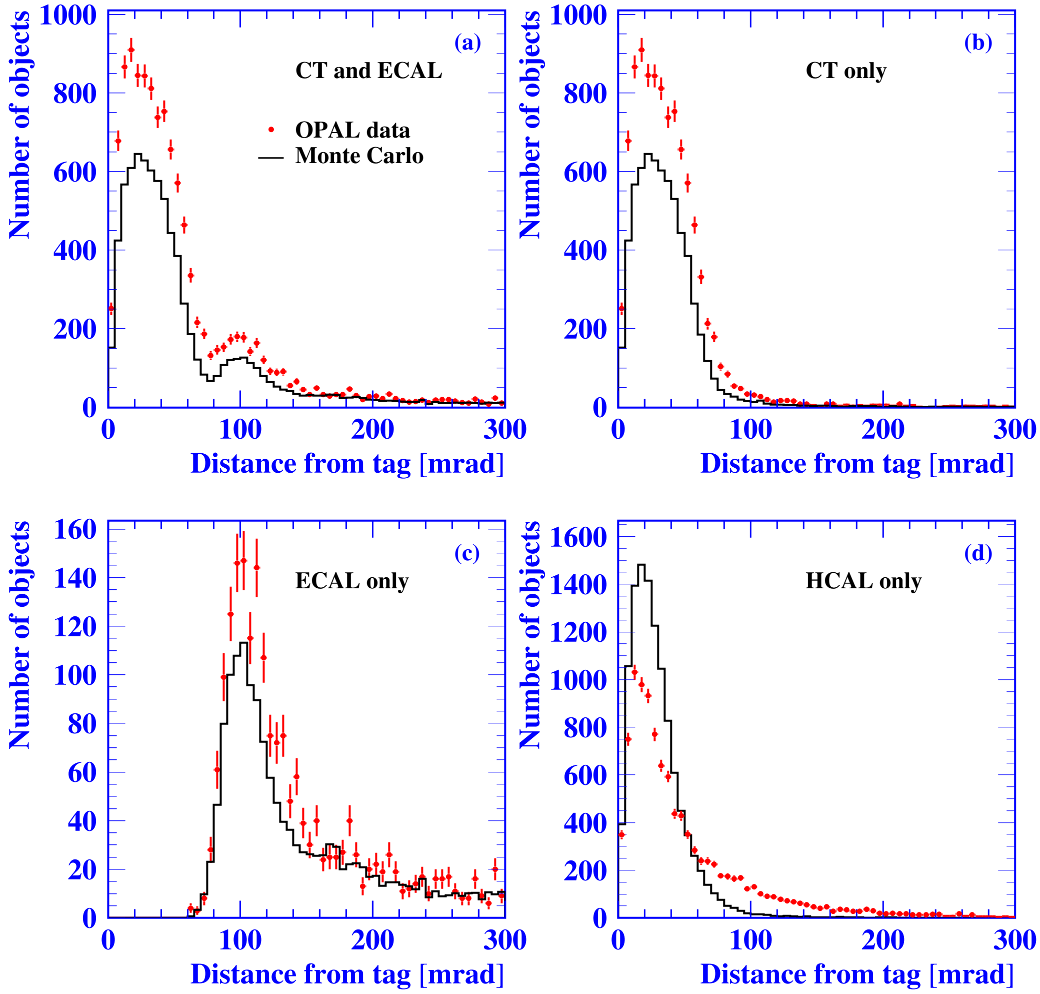

Figure A.1: Histograms showing the numbers of objects close to the 'tag' in EE Bhabha events for (a) tracks and ECAL clusters, (b) just tracks, (c) ECAL clusters and (d) HCAL clusters. Each object in an event enters separately. The data are compared to the BHWIDE Monte Carlo prediction after GOPAL simulation, which is normalised to the data luminosity.

section predicted by BHWIDE is close to the measured value [99]. One must therefore conclude that the dead material is not fully modelled in GOPAL, because a high energy electron is much more likely to shower before reaching the EE in the data than in the simulation. The structure in the plot arises from the contributions of the two subdetectors - as demonstrated in Figures A.1(b & c), where the same histograms are shown for CT and ECAL objects separately.

Around 20% of Bhabha data events show evidence of showering leading to 'extra' objects such as these, and one would expect a similar behaviour for the tags in two-photon events. Although most of these objects are low energy (Figure A.2), it would clearly be wrong to include them in the calculation of the hadronic invariant mass, irrespective of whether or not they are well reproduced by the detector simulation. From inspection of Figure A.1, a value of 200 mrad was arrived at as a suitable cone-size to exclude. This procedure also excludes HCAL clusters arising from leakage of the 'tag' shower (Figure A.1(d)), which is also poorly reproduced by the Monte Carlo. The distributions given by the other years' data used in this thesis were examined and found to be qualitatively consistent with the 1998 data.

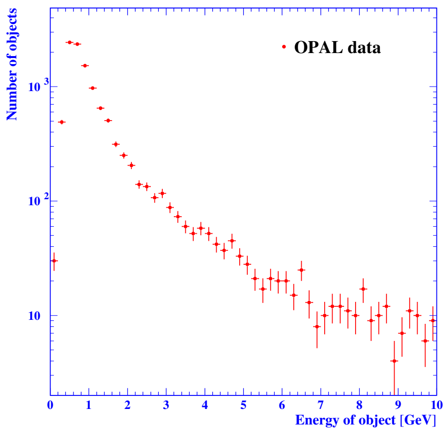

Figure A.2: Histogram showing the energies of all CT and ECAL objects within 200 mrad of the 'tag' in Bhabha data.

A.2 EE Energy Scale and Resolution

In a study of wide-angle Bhabhas [106], the GOPAL simulation was also found to be deficient in respect of the energy scale and resolution of the ECAL, in some regions. This is most likely because local concentrations of dense material had not been properly described, or even included, in the GOPAL code. It was particularly the case for clusters in the EE, so it is important to the present analysis that this be corrected for. In order to improve the agreement between data and Monte Carlo, the ECAL clusters in the Monte Carlo have been scaled and smeared. This was achieved by multiplying the energy of each cluster by a factor $\alpha(1 + \sigma r)$, where r is a random number selected from a Gaussian distribution with unit width, and α and σ are θ dependent factors. The values of α are the ratio of the mean value of E/E_{beam} in Bhabha data and Monte Carlo events, and those of σ are such that the quadratic sum of σ and the resolution in the Monte Carlo gives the data resolution. Full details of the procedure can be found in [106], which also contains the values of α and σ used to correct the Monte Carlo samples pertaining to the 1997 and 1998 data. The values for later years are given in Table A.1 [107]. In the present analysis these factors were used to correct the energy of tag clusters in the EE in all Monte Carlo samples.

$\lvert\cos\theta\rvert$	θ [mrad]	1999		2000	
		α	σ	α	σ
0.84–0.945	333–574	1.001	0.010	1.002	0.011
0.945–0.955	301–333	1.004	0.058	1.005	0.060
0.955–0.96	284–301	0.997	0.082	0.995	0.083
0.96–0.97	246–284	0.983	0.060	0.983	0.061
0.97–0.98	200–246	1.021	0.117	1.018	0.114

Table A.1: Factors used to scale and smear ECAL cluster energies in 1999 and 2000 Monte Carlo.

A.3 FD Energy Scale and Resolution

The first inspection of the tag energy distributions for the FD sample revealed a large discrepancy between data and Monte Carlo (Figure A.3). The distributions suggest that the energy scale and resolution of the FD calorimeter for high energy electrons is also not correctly represented in GOPAL. To assess this a study was made of Bhabha events where both the electrons are detected in the FD.

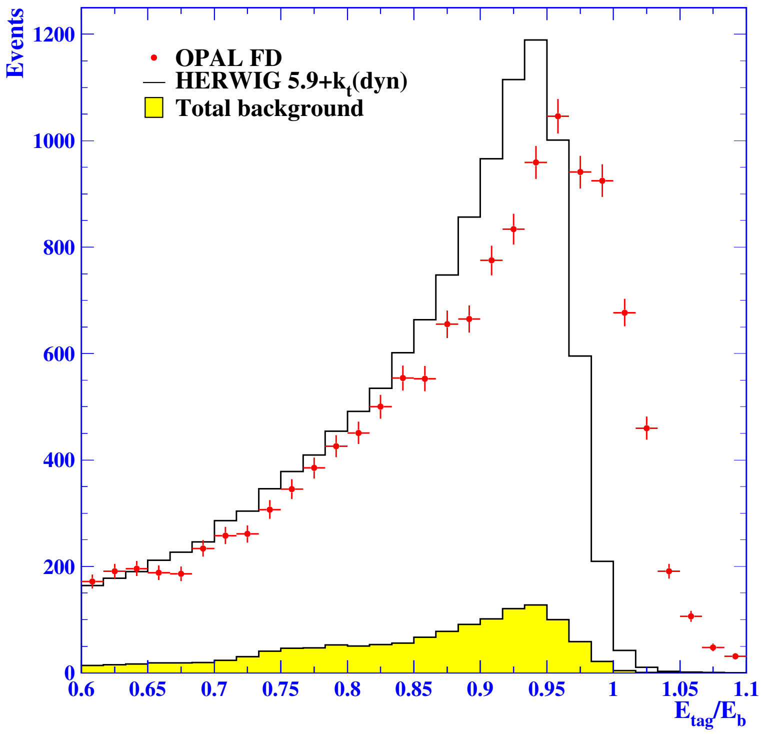

Figure A.3: The energy of the tagged electron normalised to the beam energy for the FD sample, before the corrections described in this section have been applied. All cuts (see Section 5.5) have been applied except for that on the tag energy.

Data from each of the years 1997–2000 were studied as separate samples. In addition, a sample of 500k Bhabha events at $\sqrt{s}$ of 189 GeV was generated covering the FD acceptance region using the BHLUMI [108] program. Events were selected by applying the following cuts:

- the two highest energy clusters in the event must be found in opposite ends of the detector, and must both have an energy greater that 75% of the beam energy and polar angle with respect to the beam axis of between 60 and 120 mrad;
- the acollinearity of the two clusters must be less than 142 mrad;
- there must be no tracks in the event;
- the total energy measured in the ECAL must be less than 5 GeV.

These tight cuts were designed to ensure very high purity, large statistics samples. The selection efficiency is not important for this investigation. The number of selected events in each sample is given in Table A.2.

Sample	Selected events
1997	70 130
1998	170 488
1999	344 090
2000	314 074
Monte Carlo	51 132

Table A.2: Numbers of selected FD Bhabha events.

The distribution of cluster energy normalised to the beam energy, for each of the two highest energy clusters (i.e. two entries per event), is shown in Figure A.4 for the 1998 (189 GeV) data. The dashed histogram shows the BHLUMI Monte Carlo distribution as given by the detector simulation (normalised to the number of data events). It clearly differs significantly in both mean and width from the data distribution, although the general shapes (Gaussian with a low energy tail) are consistent.

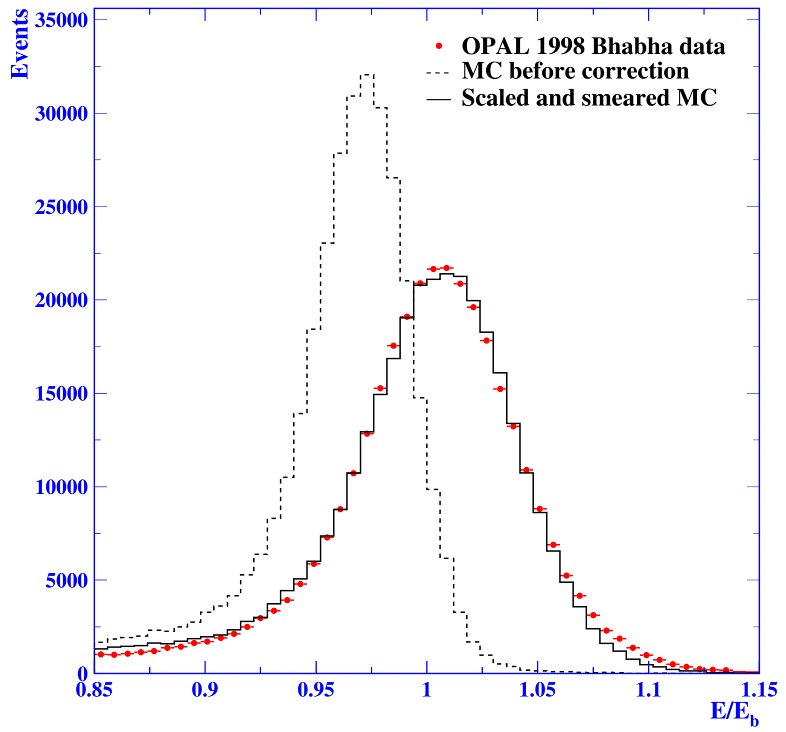

Figure A.4: Distributions of cluster energy normalised to the beam energy for the two highest energy clusters in FD Bhabha events. The Monte Carlo is normalised to the number of events in the data.

In order to correct the Monte Carlo, a procedure similar to that used for the ECAL (previous section and [106]) was employed. The normalised cluster energy, for each of the two highest energy clusters, was histogrammed in bins of θ. The statistical means and standard deviations of the distributions were obtained from the histograms truncated to the range $0.85 < E/E_{\mathrm{beam}} < 1.15$. Values of α and σ, as defined in the previous section, were then obtained by comparing the Monte Carlo sample to each year's data in turn. The factors obtained are given in Table A.3. Rather constant values are obtained across the years and also the different regions of the detector, with the exception of the bin corresponding to the outer edge of the FD detector where larger correction factors are required. The numbers indicate that the energy scale of the FD for high energy electrons was wrong by about 4% in the simulation. This is not a complete surprise - since the FD was supplanted as the main luminosity calorimeter by the SW, the calibration of the FD simulation has been neglected. In many respects this is the equivalent calibration. The corrected Monte Carlo is shown as the solid histogram in Figure A.4. The agreement between data and Monte Carlo, while still not perfect, has been considerably improved and this is reflected in the final tag energy distribution for the FD sample in the present analysis (Figure 6.4(a)).

θ [mrad]	1997		1998		1999		2000	
	α	σ	α	σ	α	σ	α	σ
110–120	1.047	0.026	1.047	0.028	1.048	0.032	1.047	0.028
100–110	1.038	0.023	1.038	0.024	1.038	0.028	1.038	0.024
90–100	1.037	0.023	1.038	0.025	1.038	0.027	1.037	0.024
80–90	1.038	0.020	1.038	0.023	1.037	0.025	1.037	0.023
70–80	1.039	0.018	1.040	0.020	1.039	0.023	1.039	0.021
60–70	1.037	0.020	1.037	0.021	1.037	0.023	1.036	0.021

Table A.3: Factors used to scale and smear FD cluster energies in Monte Carlo.

Bibliography

[1] R. Nisius, Phys. Rep. **332** (2000) 165.

[2] PLUTO Collaboration, C. Berger *et al.*, Phys. Lett. **B107** (1981) 168; Phys. Lett. **B142** (1984) 111; Nucl. Phys. **B281** (1987) 365.

[3] JADE Collaboration, W. Bartel *et al.*, Phys. Lett. **B121** (1983) 203; Z. Phys. **C24** (1984) 231.

[4] CELLO Collaboration, H.J. Behrend *et al.*, Phys. Lett. **B126** (1983) 391.

[5] TASSO Collaboration, M. Althoff *et al.*, Z. Phys. **C31** (1986) 527.

[6] TPC/2γ Collaboration, H. Aihara *et al.*, Z. Phys. **C34** (1987) 1; Phys. Rev. Lett. **58** (1987) 97.

[7] AMY Collaboration, T. Sasaki *et al.*, Phys. Lett. **B252** (1990) 491; AMY Collaboration, S.K. Sahu *et al.*, Phys. Lett. **B346** (1995) 208; AMY Collaboration, T.Kojima *et al.*, Phys. Lett. **B400** (1997) 395.

[8] TOPAZ Collaboration, K. Muramatsu *et al.*, Phys. Lett. **B332** (1994) 477.

[9] OPAL Collaboration, R. Akers *et al.*, Z. Phys. **C61** (1994) 199.

[10] OPAL Collaboration, K. Ackerstaff *et al.*, Z. Phys. **C74** (1997) 33.

[11] OPAL Collaboration, K. Ackerstaff *et al.*, Phys. Lett. **B411** (1997) 387.

[12] OPAL Collaboration, K. Ackerstaff *et al.*, Phys. Lett. **B412** (1997) 225.

[13] OPAL Collaboration, G. Abbiendi *et al.*, Eur. Phys. J. **C18** (2000) 15.

[14] DELPHI Collaboration, P. Abreu *et al.*, Z. Phys. **C69** (1996) 223.

[15] L3 Collaboration, M. Acciarri *et al.*, Phys. Lett. **B436** (1998) 403.

[16] L3 Collaboration, M. Acciarri *et al.*, Phys. Lett. **B447** (1999) 147.

[17] L3 Collaboration, M. Acciarri *et al.*, Phys. Lett. **483** (2000) 373.

[18] ALEPH Collaboration, D. Barate *et al.*, Phys. Lett. **B458** (1999) 152.

[19] A. Böhrer, *Measurement of the photon structure function at ALEPH*, Proceedings of the International Conference on the Structure and Interactions of the Photon (Photon 99), Freiburg, Germany. Nucl. Phys. Proc. Suppl., Vol. 82, ed. S. Söldner-Rembold, March 2000, 25.

[20] I. Tyapkin, *Study of the hadronic photon structure function with the DELPHI detector at LEP*, to appear in the proceedings of Photon 2001, Ascona, Switzerland, 2–7 September 2001.

[21] R.J. Taylor, *Measurement of the Hadronic Photon Structure Function F_2^γ at LEP2*, to appear in the proceedings of Photon 2001, Ascona, Switzerland, 2–7 September 2001. hep-ex/0110024.

[22] CELLO Collaboration, H.J. Behrend *et al.*, Phys. Lett. **B126** (1983) 384.

[23] TPC/2γ Collaboration, M.P. Cain *et al.*, Phys. Lett. **B147** (1984) 232.

[24] PLUTO Collaboration, C. Berger *et al.*, Z. Phys. **C27** (1985) 249.

[25] OPAL Collaboration, R. Akers *et al.*, Z. Phys. **C60** (1993) 593;
OPAL Collaboration, G. Abbiendi *et al.*, Eur. Phys. J. **C11** (1999) 409.

[26] L3 Collaboration, M. Acciarri *et al.*, Phys. Lett. **B438** (1998) 363.

[27] V.M. Budnev, I.F. Ginzburg, G.V. Meledin and V.G. Serbo, Phys. Rep. **15** (1975) 181.

[28] C.F. von Weizsäcker, Z. Phys. **88** (1934) 612;
E.J. Williams, Phys. Rev. **45** (1934) 729.

[29] P. Kessler, Il Nuovo Cimento **17** (1960) 809.

[30] H. Kolanoski, *Two-Photon Physics at* e^+e^- *Storage Rings*, Springer Verlag (1984).

[31] C. Berger and W. Wagner, Phys. Rep. **146** (1987) 1.

[32] T.F. Walsh and P.M. Zerwas, Phys. Lett. **B44** (1973) 195;
R.L. Kingsley, Nucl. Phys. **B120** (1977) 189.

[33] J. Badier *et al.*, Z. Phys. **C18** (1983) 281.

[34] C. Peterson, T.F. Walsh and P.M. Zerwas, Nucl. Phys. B174 (1980) 242; Nucl. Phys. **B229** (1983) 301.

[35] E. Witten, Nucl. Phys. **B120** (1977) 189.

[36] C.H. Llewellyn-Smith, Phys. Lett. **B79** (1978) 83.

[37] W.R. Frazer and J.F. Gunion, Phys. Rev. **D19** (1979) 2447; Phys. Rev. **D20** (1979) 147.

[38] R.J. DeWitt *et al.*, Phys. Rev. **D19** (1979) 2046.

[39] W.A. Bardeen and A.J. Buras, Phys. Rev. **D20** (1979) 166.

[40] A. Nicolaidis, Nucl. Phys. **B163** (1980) 156.

[41] D.W. Duke and J.F. Owens, Phys. Rev. **D26** (1982) 1600.

[42] L.E. Gordon and J.K. Storrow, Z. Phys. **C56** (1992) 307.

[43] `http://www-zeus.desy.de/physics/sfew/PUBLIC/public.html`

[44] V. Gribov and L. Lipatov, Sov. J. Nucl. Phys. **15** (1972) 438;
L. Lipatov, Sov. J. Nucl. Phy. **20** (1975) 95;
G. Altarelli and G. Parisi, Nucl. Phys. **B126** (1977) 298;
Y. Dokshitzer, Sov. Phys. JETP **46** (1977) 641;
G. Altarelli, Phys. Rep. **81** (1982) 1.

[45] A. Vogt, *The parton structure of real photons*, Proceedings of Photon '97, Egmond aan Zee, The Netherlands. Eds. A. Buijs and F.C. Erné, World Scientific, Singapore (1998) 3.

[46] P. Aurenche, G.A. Schuler *et al.*, Proceedings of Physics at LEP2, Eds. G. Altarelli, T. Sjöstrand and F. Zwirner, CERN 96-01, Vol. 1, 291.

[47] M. Glück, E. Hoffmann and E. Reya, Z. Phys. **C13** (1982) 119.

[48] K. Hagiwara *et al.*, Phys. Rev. **D51** (1995) 3197.

[49] E. Laenen, S. Riemersma, J. Smith and W.L. van Neerven, Phys. Rev. **D49** (1994) 5753.

[50] OPAL Collaboration, G. Abbiendi *et al.*, Eur. Phys. J. **C16** (2000) 579; CERN-EP-2002-031, submitted to Physics Letters **B**.

[51] T. Uematsu and T.F. Walsh, Phys. Lett. **B101** (1981) 263; Nucl. Phys. **B199** (1982) 93.

[52] PLUTO Collaboration, C. Berger *et al.*, Phys. Lett. **B142** (1984) 119.

[53] ZEUS Collaboration, J. Breitweg *et al.*, Phys. Lett. **B479** (2000) 37.

[54] G.A. Schuler and T. Sjöstrand, Z. Phys. **C68** (1995) 607; Phys. Lett. **B376** (1996) 193.

[55] M. Glück, E. Reya and M. Stratmann, Phys. Rev. **D51** (1995) 3220.

[56] M. Glück, E. Reya and A. Vogt, Phys. Rev. **D45** (1992) 3986; Phys. Rev. **D46** (1992) 1973.

[57] M. Glück, E. Reya and I. Schienbein, Phys. Rev. **D60** (1999) 054019.

[58] M. Drees and K. Grassie, Z. Phys. **C28** (1985) 451.

[59] H. Abramowicz, K. Charchula and A. Levy, Phys. Lett. **B269** (1991) 458.

[60] L.E. Gordon and J.K. Storrow, Nucl. Phys. **B489** (1997) 405.

[61] P. Aurenche, J.-P. Guillet and M. Fontannaz, Z. Phys. **C64** (1994) 621.

[62] OPAL Collaboration, K. Ahmet *et al.*, Nucl. Instr. and Meth. **A305** (1991) 275.

[63] P.P. Allport *et al.*, Nucl. Instr. and Meth. **A324** (1993) 34; Nucl. Instr. and Meth. **A346** (1994) 476.

[64] G. Aguillion *et al.*, Nucl. Instr. and Meth. **417** (1998) 266.

[65] M. Akrawy *et al.*, Nucl. Instr. and Meth. **A290** (1990) 76.

[66] B.E. Anderson *et al.*, IEEE Transactions on Nuclear Science **41** (1994) 845.

[67] M. Arignon *et al.*, Nucl. Instr. and Meth. **A313** (1992) 103.

[68] G. Marchesini *et al.*, Comp. Phys. Comm. **67** (1992) 465.

[69] R. Engel, Z. Phys. **C66** (1995) 203;
R. Engel and J. Ranft, Phys. Rev. **D54** (1996) 4244.

[70] J.A.M. Vermaseren, J. Smith and G. Grammer Jr., Phys. Rev. **D19** (1979) 137;
J.A.M. Vermaseren, Nucl. Phys. **B229** (1983) 347.

[71] B.R. Webber, Nucl. Phys. **B238** (1984) 492.

[72] S. Cartwright, M.H. Seymour *et al.*, J. Phys. **G24** (1998) 457.

[73] M. Derrick *et al.*, Phys. Lett. **B354** (1995) 163.

[74] The LEP Working Group for Two-Photon Physics, ALEPH, L3, and OPAL, Eur. Phys. J. **C23** (2002) 201.

[75] A. Capella *et al.*, Phys. Rep. **236** (1994) 227.

[76] I.F. Ginzburg and V.G. Serbo, Phys. Lett. **B109** (1982) 231.

[77] T. Sjöstrand, Comp. Phys. Comm. **39** (1986) 347;
M. Bengtsson and T. Sjöstrand, Comp. Phys. Comm. **43** (1987) 367;
T. Sjöstrand, Comp. Phys. Comm. **82** (1994) 74;
T. Sjöstrand *et al.*, Comp. Phys. Comm. **135** (2001) 238.

[78] B. Andersson *et al.*, Phys. Rep. **97** (1993) 31.

[79] R.K. Ellis, W.J. Stirling and B.R. Webber, *QCD and Collider Physics*, Cambridge University Press (1996).

[80] R. Brun *et al.*, *GEANT User Guide*, CERN DD/78/2.

[81] J. Allison *et al.*, Nucl. Instr. and Meth. **A317** (1992) 47.

[82] H. Plothow-Besch, Comp. Phys. Comm. **75** (1993) 396.

[83] C. Hawkes *et al.*, *ROPE Users' Guide*, unpublished.

[84] `http://opal.web.cern.ch/opal/group/twophoton/gg_welcome.html`

[85] *The MT Manual*, unpublished.

[86] J. Lauber, *Using FD to Measure Hadronic Energy in the Forward Region*, OPAL Technical Note 348, unpublished.

[87] F.A. Berends, P.H. Daverveldt and R. Kleiss, Nucl. Phys. **B253** (1985) 421; Comp. Phys. Comm. **40** (1986) 271; Comp. Phys. Comm. **40** (1986) 285; Nucl. Phys. **B264** (1986) 243.

[88] T. Sjöstrand, CERN-TH/93-7112 (1993);
T. Sjöstrand, Comp. Phys. Comm. **82** (1994) 74.

[89] S. Jadach, B.F.L. Ward and Z. Wąs, Comp. Phys. Comm. **130** (2000) 260.

[90] J. Fujimoto *et al.*, Comp. Phys. Comm. **100** (1997) 128.

[91] D. Karlen, Nucl. Phys. **B289** (1987) 23.

[92] E.W. Clay, *Measurement of the Low-x Behaviour of the Photon Structure Function* F_2^γ, PhD Thesis, University College London (2000).

[93] V. Blobel, *Unfolding Methods in High-Energy Physics Experiments*, DESY-84-118 (1984);
V. Blobel, *The RUN manual, Regularized Unfolding for High-Energy Physics Experiments*, OPAL Technical Note 361, unpublished.

[94] R.J. Barlow, *Statistics: a guide to the use of statistical methods in the physical sciences*, Wiley (1989).

[95] A. Höcker and V. Kartvelishvili, Nucl. Instr. and Meth. **A372** (1996) 469.

[96] E.W. Clay, *Unfolding Techniques for Extracting the Photon Structure Function* F_2^γ, OPAL Technical Note 550, unpublished.

[97] M. Landrø, K.J. Mork and H.A. Olsen, Phys. Rev. **D36** (1987) 44;
F.A. Berends, P.H. Daverveldt, and R. Kleiss, Nucl. Phys. **B253** (1985) 441; Comp. Phys. Comm. **40** (1986) 285.

[98] E. Laenen and G.A. Schuler, Phys. Lett. **B374** (1996) 217;
E. Laenen and G.A. Schuler, *Model-independent QED corrections to photon structure-function measurements*, Proceedings of Photon '97, Egmond aan Zee, The Netherlands. Eds. A. Buijs and F.C. Erné, World Scientific, Singapore (1998) 57.

[99] OPAL Collaboration, G. Abbiendi *et al.*, Eur. Phys. J. **C13** (2000) 553.

[100] OPAL Collaboration, G. Abbiendi *et al.*, Eur. Phys. J. **C14** (2000) 199.

[101] F. James and M. Ross, *MINUIT-function minimization and error analysis*, CERN Program Library D506 (1995).

[102] J.M. Butterworth and R.J. Taylor, Nucl. Phys. Proc. Suppl., Vol. 82, ed. S. Söldner-Rembold (2000) 112.

[103] S. Albino, M. Klasen and S. Söldner-Rembold, *Strong Coupling Constant from the Photon Structure Function*, DESY 02-052 (2002).

[104] OPAL Collaboration, G. Abbiendi *et al.*, Phys. Lett. **B533** (2002) 207.

[105] S. Jadach, W. Placzek, B.F.L. Ward, Phys. Lett. **B390** (1997) 298.

[106] C.P. Ward, *Analysis of Bhabha Events at 189 GeV*, OPAL Technical Note 612, unpublished.

[107] C.P. Ward, private communication.

[108] S. Jadach *et al.*, Comp. Phys. Comm. **70** (1992) 305; Comp. Phys. Comm. **102** (1997) 229.